A VLBI STUDY OF OH MASERS IN A PROTO-PLANETARY NEBULA OH 0.9+1.3.

A thesis submitted in fulfillment of
the requirements for the degree of

MASTER OF SCIENCE

of

RHODES UNIVERSITY

by
KIM MCALPINE

Abstract

This thesis reports the calibration, imaging and analysis of one epoch of VLBA observations of the 1612 MHz OH maser emission from the proto-planetary nebula OH 0.9+1.3. These are the first polarisation VLBI observations of this source and the spatial morphology of the OH emission is resolved on this scale. Proto-planetary nebulae represent the transition phase in the evolution of stars between the asymptotic giant branch (AGB) phase and their emergence as planetary nebulae. A long-standing astronomical question is how the predominantly spherical circumstellar envelopes of AGB stars evolve into the bipolar and axisymmetric structures that are commonly observed in planetary nebula. Proto-planetary nebulae offer a unique opportunity to study this transformation process. The high-resolution VLBI maps produced in this thesis were used to investigate the morphology and kinematics of OH 0.9+1.3 with a view to gaining insight into the development of asymmetries in the circumstellar material.

The OH maser emission of OH 0.9+1.3 has a double-peaked profile with one peak blue-shifted and the other red-shifted with respect to the stellar velocity. The total intensity maser maps demonstrate a considerable degree of asymmetry with the blue- and red-shifted emission located in spatially distinct regions of the envelope. The blue-shifted emission is distributed preferentially along an axis at a projected position angle of $\sim 135^{\circ}$ (North through East). The morphology of this source is not consistent with the standard symmetric thin-shell model and an attempt to fit the traditional OH/IR kinematic model of a simple expanding shell to the maser components was found to be unsatisfactory. No definitive evidence of a bipolar outflow was observed either. The high degree of asymmetry observed in the source is consistent with its status as a proto-planetary nebula.

The source was imaged in all four Stokes parameters and the fractional linear and circular polarisations of the maser components were derived from the Stokes parameter maps. In all except one of the components the total

fractional polarisation was found to be low ($< 15\%$). The mean fractional linear and circular polarisation were calculated to be 5.54% and 7.11% respectively. The absence of an identifiable Zeeman pair in the Stokes V map prohibited the estimation of the magnetic field in the circumstellar envelope of this source.

Acknowledgments

I would like to thank my two Supervisors Prof. Justin Jonas and Dr. Athol Kemball for their support, encouragement and considerable patience with my many questions.

Thanks must also go to all the students who have occupied Room 48 in the Physics Department with me at one time or another. They provided an invaluable support network in times of crisis. Thanks in particular to Laura for all the advice she has given me during the course of this work. Thanks to Anthony for seeing me through many a computer emergency. Thanks to all the staff in the Physics department who have always made it an absolute pleasure to be a member of the extended family of Physics at Rhodes. Finally thanks to my family and fiance, without their continuous encouragement I would not have prevailed.

I gratefully acknowledge the financial assistance of Rhodes University and SKA South Africa

Contents

List of Figures

List of Tables

Chapter 1

Introduction

The period immediately following the asymptotic giant branch is one of the least understood phases of stellar evolution and there remain many open questions regarding the transformation of AGB stars into planetary nebulae. These objects are heavily obscured by dust at optical wavelengths and thus high resolution observations of masers in their circumstellar envelopes provide a useful probe of the dynamics of these poorly understood environments.

This thesis presents full polarisation VLBA observations of OH maser emission from OH 0.9+1.3 which is a proto-planetary nebula. The rest of this chapter provides an introduction to the topic of proto-planetary nebulae including their evolutionary status, the open questions regarding their evolution and current models and theories which attempt to address these questions.

Chapter 2 gives an overview of the powerful observing technique of Very Long Baseline Interferometry and chapter 3 details the data reduction steps which were undertaken in order to produce the final maps. Chapter 5 presents an analysis of the maser maps along with the final maps themselves. Chapter 4 presents a review of the source properties known to date.

1.1 Evolutionary status

Asymptotic giant branch (AGB) stars are the evolved descendants of main sequence stars with low to intermediate masses (between $1M_{\odot}$ and $8M_{\odot}$). These stars consist of a hot inner core and large convective mantle. Typically the stellar core has a diameter of approximately $\sim 10^8$ cm while the mantle extends over a region of $\sim 10^{13}$ cm. The outer regions of the mantle are only weakly gravitationally bound. The core consists of an electron-degenerate carbon and oxygen mixture and no nuclear burning takes place within the core. Above the core lies a helium shell and above that a hydrogen mantle (Olofsson, 1999). The mantle is fully convective and the outer regions are cool enough that formation of molecules will take place. Helium burning of the shell provides the energy during the early AGB evolution but eventually the hydrogen at the base of the hydrogen-mantle ignites and this marks the beginning of the thermally pulsing AGB phase (TP-AGB). In this stage the process of hydrogen burning into helium leads to a mass increase of the helium layer. Regularly, but only for a short time, the helium burns into carbon and oxygen creating a temporary large increase in the luminosity of the star (Habing, 1996). These events are the 'thermal pulses' from which the name TP-AGB is derived.

During the TP-AGB phase the star experiences a period of intense mass loss and the ejected matter creates an expanding dusty molecular circumstellar envelope (CSE). Mass loss continues until the mantle is almost completely depleted and it leads to the eventual termination of this phase of stellar evolution (Habing, 1996). The rate of mass loss increases with time and the maximum achievable mass loss rate increases with increasing main sequence mass of the central star (Olofsson, 1999). Observed mass loss rates range between $10^{-8}M_{\odot}.\mathrm{yr}^{-1}$ and $10^{-4}M_{\odot}.\mathrm{yr}^{-1}$ (Bujarrabal, 1999). The pulsation of an AGB star strongly affects the structure of the surrounding stellar atmosphere. In particular, it levitates material outwards to create an atmosphere that is far more extended than one which is created in hydrostatic equilibrium. Pulsation may produce mass loss in itself, but more importantly it creates an atmosphere which encompasses regions with suitable conditions

for the formation of dust grains (Olofsson, 2001). Radiation pressure from the central star acts directly on dust grains formed in the extended atmosphere of the star and collisions between the dust grains and gas molecules transfers this momentum to the gas in the CSE (Habing, 1996). It is likely that this process is the main agent responsible for the intense mass loss observed in AGB stars and subsequently it drives the outward expansion of the circumstellar envelope.

The CSE consists of dust and molecular gas. The molecules are located in envelopes of different sizes, or shells of different radii and widths, depending on UV photon flux and their chemical formation routes. The molecules with the largest envelopes are CO and H_2; the dust grains exist throughout the molecular envelopes and extend way beyond them (Olofsson, 2001). The dust in the circumstellar envelope absorbs the optical radiation from the central star and re-emits in the infra-red. The high degree of optical extinction afforded by the dust makes direct observations of the central star difficult (Kwok, 1993). However, these cool envelopes support maser emission from several species including SiO, H_2O and OH which afford an excellent mechanism for studying the circumstellar environment. The SiO masers form in the stellar atmosphere; the H_2O masers at distances of up to 10^{15} cm from the central star and the OH masers between 10^{15} and 10^{16} cm. The H_2O is photo-dissociated into OH by UV photons from the interstellar radiation field. As UV radiation also dissociates OH into O and H the OH masers exist only in a very thin shell (Goldreich and Scoville, 1976). A schematic representing maser emission in the circumstellar envelope of a typical AGB star is presented in figure 1.1. Information about the envelope can also be gleaned from thermal emission from many molecular species in the envelope. In particular the CO line emission is very useful as it is used to determine reliable mass loss rates (Olofsson, 1999). Presently over 60 different molecular species have been detected in circumstellar envelopes.

AGB stars are the precursors of planetary nebulae (PNe). Ultimately mass loss will decrease, the envelope will become detached and the central star's temperature will increase to sufficiently high temperatures to produce an ionising wind which will ionise the inner region of the circumstellar shell.

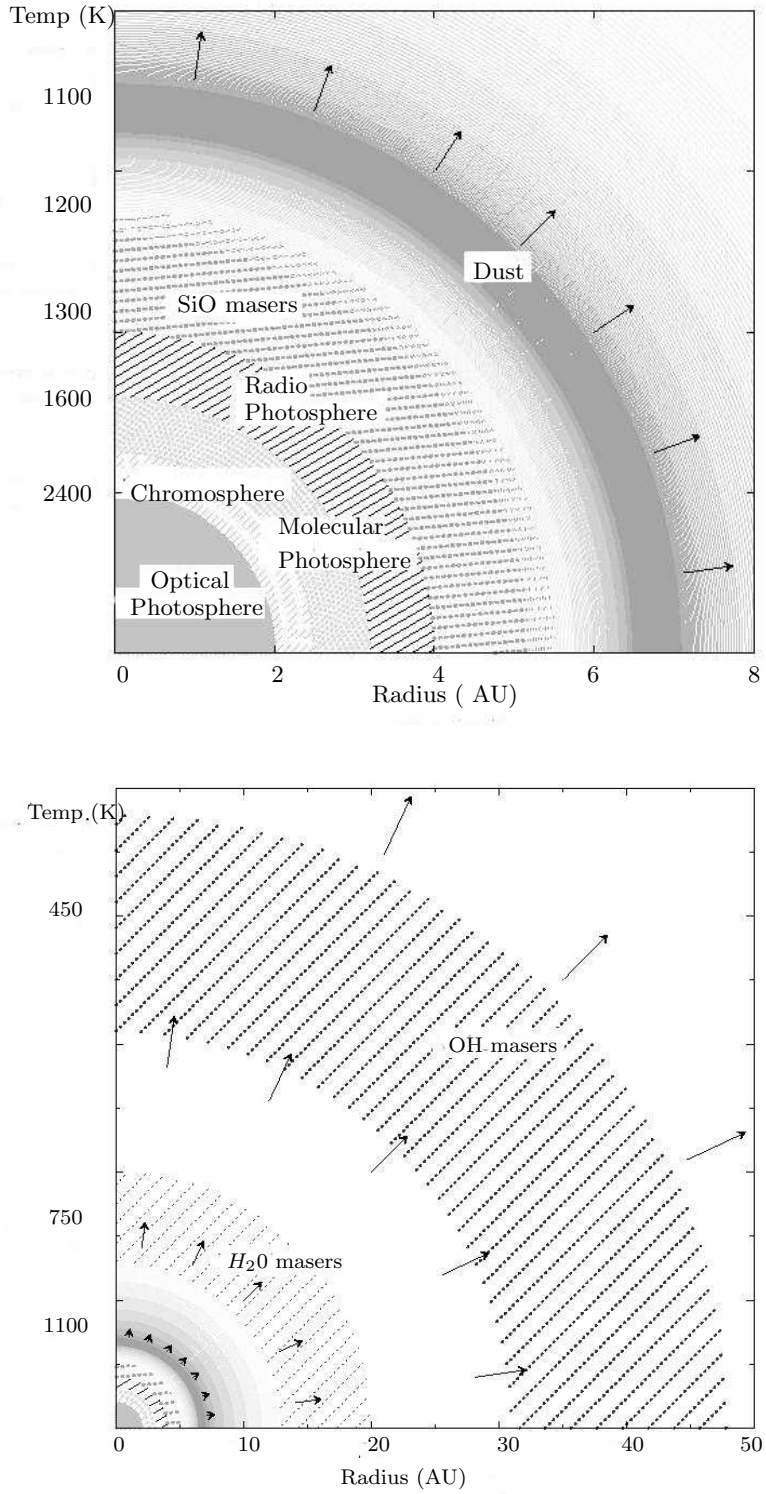

Figure 1.1: Schematic of the circumstellar envelope of a typical AGB star, taken from Reid (2002).

The emergence of strong recombination lines of hydrogen and helium and collisionally excited lines of metals in the gas envelope signifies the beginning of the planetary nebula phase (Kwok, 1999).

Proto-planetary nebulae (PPNe) represent the transition phase in the evolution of stars between the AGB phase and their emergence as PNe. Specifically PPNe are defined as stars that have ceased large-scale mass loss on the AGB but have not evolved to be hot enough to ionise the surrounding remnants of the AGB envelope (Kwok, 1993). A useful mechanism for identifying objects in this transition phase is the IRAS two-colour diagram. AGB stars with oxygen rich circumstellar shells form a sequence in the diagram which is interpreted as an evolutionary track for these objects (van der Veen and Habing, 1988). This evolutionary track is indicated by the dashed line in figure 1.2, and stars in the early AGB phase are to be found in region I of this diagram. On the AGB, where the mass loss rate is increasing, stars evolve towards lower colour temperatures as a result of increasing optical depth in the dusty circumstellar envelope. Therefore the most evolved AGB stars with the largest circumstellar envelopes are to be found in region IV of the diagram. Planetary nebulae are found predominantly in region V (van der Veen and Habing, 1988). Thus the colours of AGB stars and PNe are clearly separated in the diagram and a general trend of decreasing colour temperature with increasing age can be discerned. After mass loss is terminated the decrease in colour temperature is caused by geometric dilution of the dust as the remnant envelope expands away from the star. Using this empirical colour sequence it is possible to predict the IRAS colours of transition objects (Kwok, 1993). In general they are expected to have colour temperatures of between 150 - 300 K.

The infra-red continuum properties alone cannot define a PPN, as young stars are expected to have similar colour temperatures. Thus it is useful to supplement the colour temperature data with further observations of a source in order to unambiguously identify its evolutionary status. Useful distinguishing properties of a PPN candidate includes molecular emission of the remnant AGB shell.

Although the evolutionary sequence of this transformation is well estab-

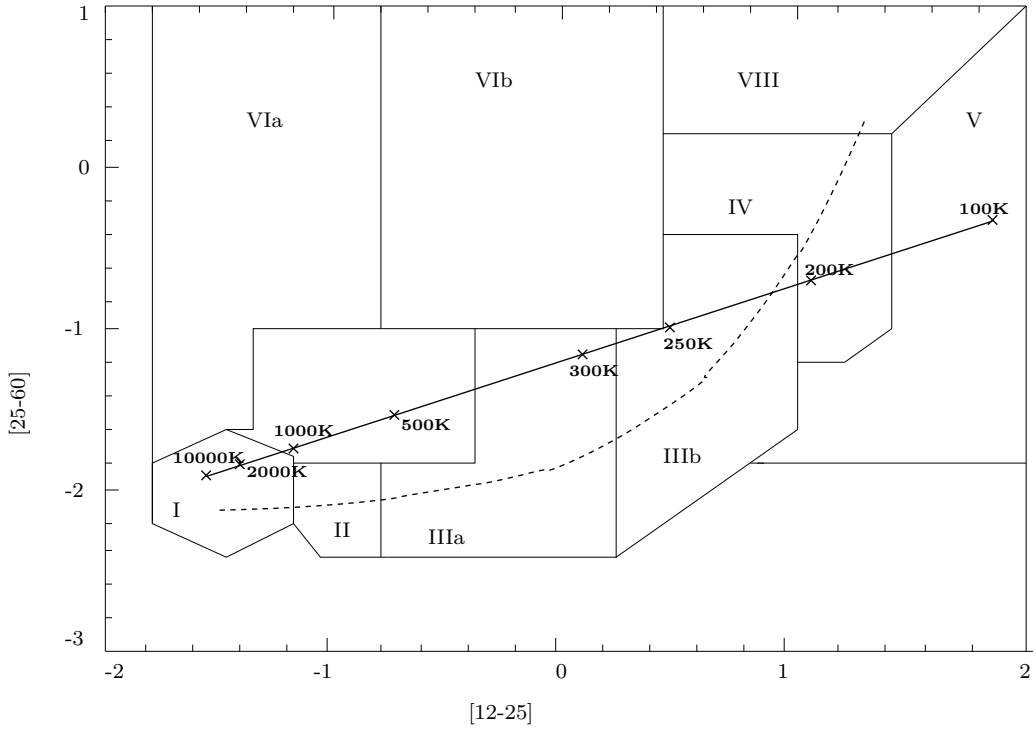

Figure 1.2: Regions of the IRAS two colour diagram which separate different types of AGB stars, taken from van der Veen and Habing (1988). The dashed line indicates the evolutionary track of oxygen rich stars through the diagram and the full line indicates the black body curve. Here [12]-[25]=2.5log$\left(\frac{F_{25\mu m}}{F_{12\mu m}}\right)$ and [25]-[60]=2.5log$\left(\frac{F_{60\mu m}}{F_{25\mu m}}\right)$.

lished there are large differences in the morphology of CSE's of AGB stars and the ionised nebula of a PN. Planetary nebulae show bright rims and well defined shell-like structures and a large fraction ($\sim$ 70%) show non-spherical morphology, particularly bipolar, axisymmetry or point-symmetry (Manchado et al., 2000). In contrast, the circumstellar environment of progenitor AGB stars are largely spherically symmetric and 'filled', i.e., not shell-like (Sahai, 1999). The planetary nebulae also have higher densities and expansion velocities than the CSE's of AGB stars.

Originally, the accepted explanation for the observed structures in PNe was by way of the interacting stellar wind (ISW) theory, first proposed by Kwok et al. (1978). In this theory a fast, low density stellar wind turns on to-

wards the end of the AGB phase as the central star increases in temperature. This wind will compress the material ejected by the earlier slower winds into a thin dense rim at the leading edge of the wind (Balick and Frank, 2002). Assuming that both winds expand isotropically, the theory predicts that the nebula should consist of a hot nearly invisible cavity separated from a smooth mantle of slow winds by a hot dense rim of swept-up gas. This morphology is illustrated in figure 1.3. The ISW theory succeeds as a plausible explanation for most spherical or mildly elliptical planetary nebulae. Unfortunately as mentioned previously, PNe come in a large variety of shapes and a large proportion (13%) of PNe have bipolar structures (Manchado et al., 2000).

The ISW theory can be conveniently extended to explain the commonly observed bipolar planetary nebulae by invoking an equatorial density enhancement in the circumstellar envelope which preferentially directs the fast stellar wind along the polar axis. This suggestion is known as the generalised interacting stellar wind (GISW) theory. Numerical simulations including those by Livio and Soker (1988), Icke et al. (1992) and Mellema and Frank (1997) have demonstrated that this paradigm can produce a wide variety of nebular morphologies including highly collimated jets.

This model has had considerable success but falls short on two fronts. Firstly, the origin of the collimating density enhancement remains a matter of conjecture, although Soker and Livio (1989) have speculated that it may be the result of binary mergers. Secondly, high resolution observations by the Hubble Space Telescope (HST) reveal PNe morphologies with higher order structure that appear difficult to explain with the classic GISW paradigm.

The observed features which currently evade a widely accepted explanation include:

1. Point-symmetry: Point symmetric pairs of knots and jets have been observed in a number of PNe by Lopez et al. (1995) and Sahai and Trauger (1998). There are also bipolar and elliptical PNe which show point symmetry in their brightness distributions. Suggested explanations for these phenomena include precessing jets (Frank, 1999).

2. Jets and FLIERS/Ansae: FLIERS(Fast low ionisation emission regions)

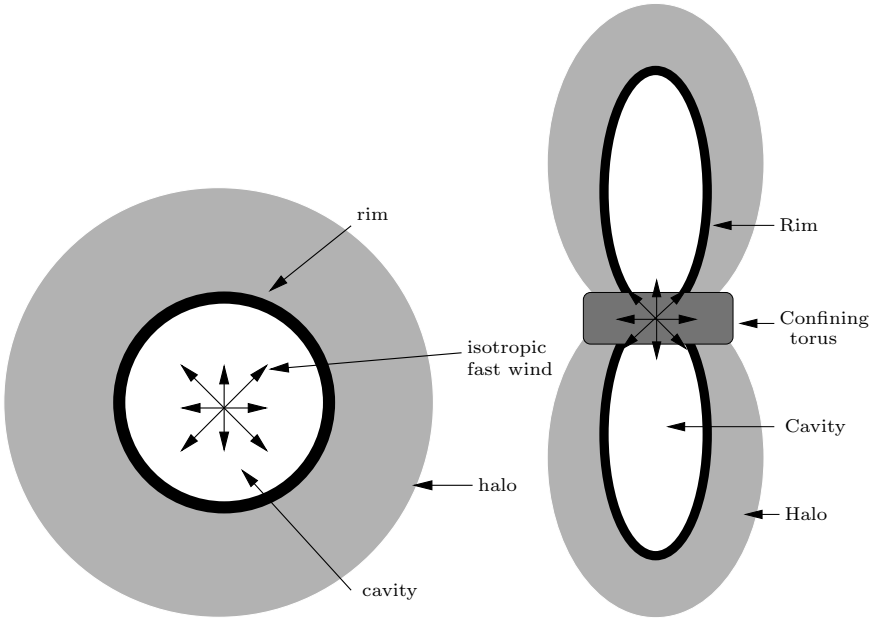

(a) ISW (b) GISW

Figure 1.3: Schematic representation of a planetary nebula shaped by the interacting stellar wind theories.

are small, bright knots of low excitation gas. They tend to come in pairs equidistant from and on opposite sides of the nucleus along the polar axis of PNe. They are most common in elliptical PNe and their Doppler shifts indicate that they have much higher velocities than the slowly expanding gas of the planetary nebulae that surrounds them (Balick et al., 1998). Thus far they have eluded most attempts at theoretical explanation. Fast jets have also been observed in PNe. Such jets can be produced by the GISW provided that the collimating structure is a very fat torus and it is not clear whether such structures are common in PNe.

3. Multipolar episodic outflows: Some PNe show multiple nested axisymmetric outflows. Sometimes these multiple shells have common axes of symmetry while in others the axes are misaligned, i.e., they are multipolar (Frank, 1999).

4. Rings and arcs: The observation of concentric circular rings and arcs

in both PN and PPNe's was an unexpected development. Detections of arcs include those by Hrivnak et al. (2001) (IRAS 16594-4656, IRAS 20028+3910), Balick et al. (2001) (NGC 6543) and Kwok et al. (1998) (IRAS 17150-3224). These arcs are believed to result from modulation of the mass loss rates during the AGB phase, although the exact mechanism is not well understood (Mauron and Huggins, 2000). However, the preservation of these perfectly circular features co-existing with bipolar lobes in the planetary nebulae pose a difficult phenomenon to explain (Kwok et al., 2000). An image of a bipolar PN with circular arcs is presented in figure 1.4.

Thus it seems that the transition from an AGB star to a planetary nebula is far from clearly understood. There remain many open questions concerning the origin of highly complex structures in PNe.

1.2 Evolutionary onset of asymmetry

Crucial to understanding the processes that shape the asymmetry of planetary nebulae is knowing when the asymmetry first manifests itself. However, detailed study of circumstellar envelopes is difficult because of the relatively cool material that the envelopes consist of and the high angular resolution needed to resolve the envelopes. One technique to image the gas is by way of mm interferometry and a survey of the CO emission from 46 AGB and post-AGB stars by Neri et al. (1998) indicated that some 70% of these objects are consistent with a spherical geometry. This survey was carried out using the IRAM interferometer and had a relatively low resolution of $\sim 3 \times 5$ arcseconds.

A second technique is to image the thermal infra-red dust emission using speckle interferometry. Studies using this technique have revealed asymmetries in the circumstellar dust of individual AGB stars very close to the central object. These include the paper by Gauger et al. (1999) on AFGL 2290 which demonstrates that the inner envelope of this object is elliptical. These observations have a resolution of 75 milliarcseconds. Near-infra-red

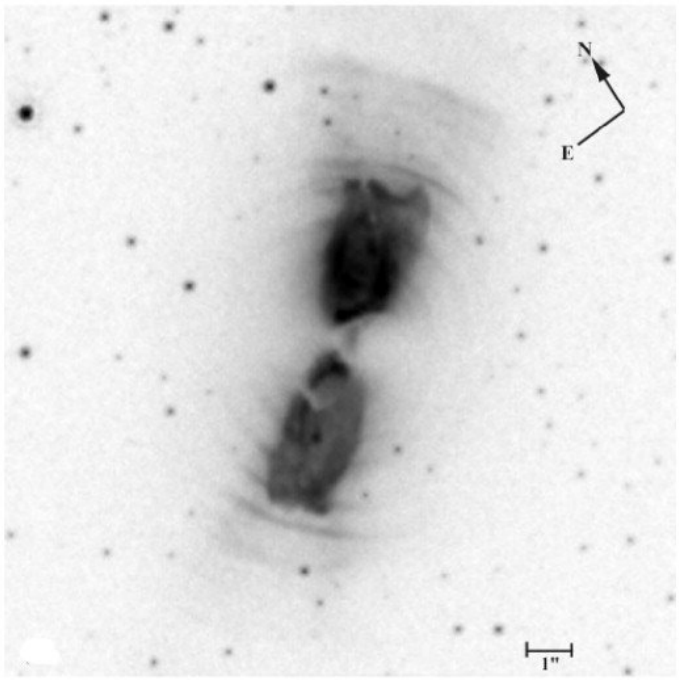

(a) Image of arcs in IRAS 17150-3224, taken from Kwok et al. (1998).

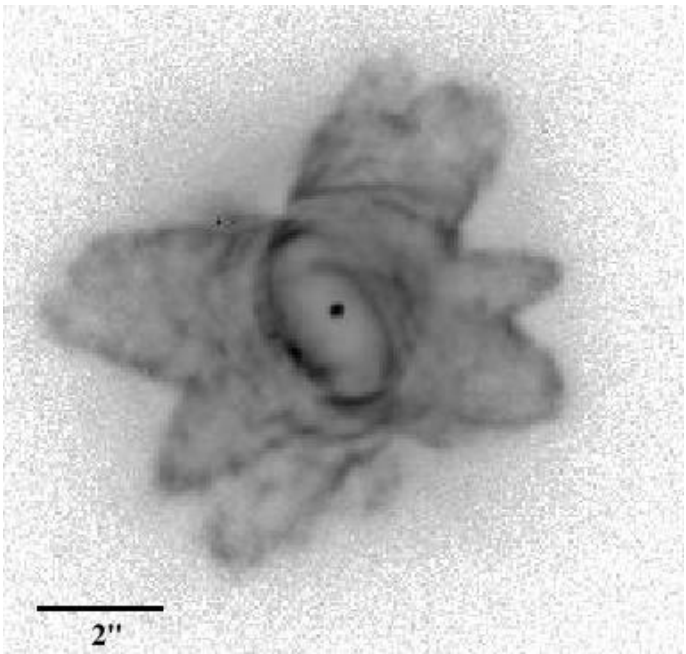

(b) Image of multipolar episodic outflows in He2-47, taken from Sahai (2002).

Figure 1.4: Images of proto-planetary nebulae which display complex structure.

bi-spectrum speckle-interferometric images of CIT 3 (Hofmann et al., 2001) and IRC+10216 (Weigelt et al., 2002) also reveal detailed structure of the dust. The observations are made in the J-, H- and K-band with resolutions of 50, 56 and 73 milliarcseconds respectively. Two structures are identified in the J-band of CIT 3: a compact elliptical core and a fainter fan-like structure. The paper by Weigelt et al. (2002) indicates that the dust shell in IRC+10216 is clumpy, bipolar and changing on a timescale of years.

It is also sometimes possible to image the circumstellar dust in scattered light at optical wavelengths. The inner envelope is illuminated by light from the central star and the outer envelope is illuminated by ambient galactic radiation. Mauron and Huggins (2000) present optical observations of this type of IRC+10216. This object is the nearest AGB carbon star which is still experiencing significant mass loss. This object is a carbon rich star and thus it must be borne in mind that it is not a good representative of post AGB evolution in oxygen rich stars. However, despite this, general arguments about asymmetry can be applied, with care, to its oxygen rich AGB star counterparts. It serves as an important archetype for the study of mass loss on the AGB and has been extensively studied at infra-red and millimeter wavelengths. This object is over-represented in observational studies because of its relative proximity. The Mauron and Huggins (2000) paper combines arcsecond resolution images from the Canada-France-Hawaii telescope with archival HST observations. This combination provides a resolution of $0.1 - 1$ arcseconds over a very large field. These images reveal the presence of multiple, complex shell structures within the circumstellar envelope. The outer shells are circularly symmetric and a bipolar structure is visible close to the central star. These observations are important if representative of mass loss in other AGB stars. They favour an isotropic, episodic mass loss process on highly-variable timescales.

More recent optical observations of AGB circumstellar envelopes by Mauron and Huggins (2006) demonstrate that in a sample of five successfully imaged envelopes, all except one, show deviations from spherical symmetry. This survey also combined ground-based observations with HST images. The resolution of the ground-based observations varied over a range of $1 - 2.2$ arc-

seconds. Two of the objects (IRC+10216 and IRC+10011) exhibit a circularly symmetric outer halo with a bipolar core, one (AFGL 2514) is elliptical and the other (AFGL 3068) has a clear spiral structure visible in its envelope. Although the sample size is small, the fact that so many of the objects deviate from spherical symmetry implies that envelope shaping commences on the AGB before the transition to the PPNe phase.

Proto-planetary nebulae are just beginning their expansions and are thus intrinsically small and heavily obscured by dust. Their lifetimes are relatively short and thus they are rarer than typical PNe. Despite these difficulties a growing number of these transition objects are being imaged (Sahai, 2004). Current HST images of PPNe and young PNe include those by Sahai and Trauger (1998), Sahai (2004), Ueta et al. (2000) and Kwok et al. (1998) and they indicate that most, if not all, of these objects are bipolar or multipolar. The objects in these surveys are selected to be small, to have low ionisation and to have a large infra-red excess. These criteria select for young objects where the ionisation of the envelope has only just begun.

From these observations it is clear that point symmetry and multipolarity are very common. Many of these objects have internal components such as rings or hourglasses embedded in a nebula whose overall morphology is completely different from these structures. It is important to note that although a denser torus is visible around the central star of some of these nebulae, objects without this feature also display bi- or multi-polar structure and occasionally the resolved torus isn't aligned with the overall axis of the nebula. Thus it seems unlikely that the torus is the primary agent shaping the nebula (Sahai and Trauger, 1998). These PPNe frequently exhibit higher order symmetries than the more mature PNe, including multiple point-symmetric structures, and multiple nested outflows with different axes of symmetry. The fact that fully fledged PNe only rarely show such high order symmetries suggest that fast winds, hot bubbles and ionisation fronts may smooth or eradicate many structural details, and possibly invite unrealistically simplistic approaches to explaining the transition (Balick and Frank, 2002). It is clear that the GISW model is inadequate for explaining the observed structures. Thus it has been proposed that the winds which form these structures may not be isotropic.

The prevalence of complex structures in these very young objects indicates that the shaping process has already taken place very soon after the object has left the AGB. Whether this shaping occurs when the object is still on the AGB or only in the immediate post-AGB phase is not entirely clear yet.

Some HST images show evidence of multiple low-latitude jet-like outflows and Sahai and Trauger (1998) propose that high speed jets in the early post-AGB phase carve the imprint of complex structures into the CSE. Subsequent expansion of an isotropic, fast stellar wind inside the imprinted envelope results in the observed PN. The overall shape of the nebula depends on how the initial jet-like outflows change with time. Although jets had been detected in PNe prior to this suggestion their role in shaping the overall nebulae was and still is largely unknown.

Interferometric maps of OH masers provide important insights into the development of asymmetries. In particular, OH maser Very Long Baseline Interferometry allows high-resolution imaging of the obscured CSE, thus providing a useful probe of the evolution of the envelope. Interferometric images of OH masers of ten OH/IR stars with unusual OH spectra revealed that several of them had maser distributions that were consistent with a bipolar outflow (Zijlstra et al., 2001). These sources were imaged using the VLA, MERLIN and ATCA arrays with resolutions ranging from $1-6$ arcseconds. Half the objects in this study have IRAS colours consistent with post-AGB evolution and one of them has colours consistent with high ongoing mass loss which may indicate that it is still in the AGB phase. Some of the outflows determined for these sources are consistent with jet-like, rather than wind-like, outflows (Zijlstra et al., 2001). A single dish survey by Deacon et al. (2004) of the OH emission of a large number of likely proto-planetary nebulae indicates that approximately 25% of these sources are likely to have asymmetric or bipolar outflows. This was concluded on the basis of the shape of their OH-maser spectra. Several objects with double-peaked spectra with gently sloping outer edges were shown to have bipolar outflows by Zijlstra et al. (2001). Thus objects with this 'velocity wing' spectral profile, along with objects whose irregular spectra had large velocity widths (> 50 km.s^{-1}), were deemed likely to have bipolar outflows. Objects with irregular profiles,

including those with multiple peaks and emission plateaus, were classified as having asymmetric outflows. The bipolar outflows identified by these two papers may be influential in the shaping process.

1.3 Causes of asymmetry

1.3.1 Interacting winds, ionisation and radiative processes

The cause of the observed complex structures in PNe is the subject of considerable debate and widespread attempts to understand the various effects at play have been made. Previously the primary elements of the GISW model were discussed. Refinements to this model, including the effects of radiative losses, the speed and acceleration of the fast stellar wind and the role of ionisation, can produce a wide variety of morphologies (Balick and Frank, 2002). It has been shown that the actions of an ionisation front (IF) may play a role in the development of microstructures observed in nebulae. It is likely that the equatorial density enhancement proposed in the GISW forms before the onset of significant stellar UV flux. The interaction between the IF and a dense torus, or with radiative shock fronts created by the interacting winds, can lead to instabilities of various types including Rayleigh-Taylor modes (Breitschwerdt and Kahn, 1990; García-Segura et al., 1999). This would lead to the development of radial Rayleigh-Taylor fingers in the nebulae. Also, ionisation in environments with large gradients of the polar to equatorial density distribution leads to latitudinal pressure gradients, which may result in a more elliptical shaped nebula (Mellema, 1997). Thus stellar UV photons influence the global structure of the nebulae and may explain how ripples and fingers grow in young PPNe.

1.3.2 Jets

As mentioned previously, the highly asymmetric structures in PPNe have sparked the idea that these objects are shaped by fast collimated outflows

and jets. In many cases jets are not directly detected but their interaction with the ambient circumstellar medium produces compressed structures of enhanced density (Sahai, 2004). In these cases one can only infer the properties of the jets by fitting the shapes and kinematics of the objects using magnetohydrodynamic (MHD) simulations. It is thus desirable to supplement the current images of PPNe with information about their kinematics in order to better constrain these models. Sahai and his colleagues have embarked on a programme of VLBA/VLA interferometric observations of OH/H_2O masers together with long slit STITS spectroscopy which he hopes will provide greater insight into collimated jets as primary agents for shaping PPNe (Sahai, 2004).

Current evidence for jets in PPNe include swept-up CSE material in HST images, jet-like outflows detected in OH maser emission from various post-AGB objects (Zijlstra et al., 2001) and the so-called 'water fountain' nebulae. Water fountain nebulae are young PPNe with high velocity outflows traced by H_2O maser line emission. Theoretical models suggest the masers form in shocked regions created when the high-speed jet collides with an ambient gas cloud. Objects which belong to this class are the AGB star W43A (Imai et al., 2002), and the two PPNe IRAS 16342-3814 (Likkel and Morris, 1988) and IRAS 19134+2131 (Imai et al., 2004). The H_2O masers indicate that the jet in W43A is precessing and a corkscrew type structure visible in the NIR radiation of the dust surrounding IRAS 16342-3814 may indicate that this object also has a precessing jet (Sahai et al., 2005).

Although there is some observational evidence that jets may be common in young planetary nebulae, the nature of the launching mechanism remains elusive (Frank, 1999). The most promising models fall into two categories: i) those which require a binary companion and ii) those which rely on stellar magnetic fields. Binarity and stellar magnetic fields have also been invoked in more traditional attempts to explain asymmetry, and the following discussion highlights the main scenarios by which these two mechanism may influence shaping.

1.3.3 Binarity

There are several classes of binary interaction with a stellar companion relevant to the shaping of planetary nebulae. Models which rely on the inertia of some pre-existing structure to direct the nebula along a preferential axis require initial conditions (i.e., torii, accretion disks) which could be supplied by interaction with a binary companion, either by way of mergers, accretion disks or tidal torquing (Balick and Frank, 2002). Models which demonstrate that fast rotation of the central star might result in axisymmetry also cite the presence of a companion star as a feasible mechanism for spin up; e.g., Dijkstra and Speck (2006). It is also proposed that substellar masses such as a brown dwarf or Jupiter sized planet may have sufficient dynamical influence to be important in shaping (Soker, 2004).

Common envelope evolution

A common envelope (CE) phase occurs in a binary system where the more massive star has filled its Roche lobe. In the case of a star evolving towards the AGB, if the larger mass losing star is unable to contract at the same rate as its Roche lobe then it will transfer envelope mass to its companion (Iben and Livio, 1993). If the time scale of mass donation is considerably shorter than the time it takes for the companion to adjust thermally, the accreted mass will heat up, expand and fill the companion's Roche lobe.

Thereafter, the donated mass flows into a common envelope that encompasses both stars. The frictional interaction of this envelope with the stellar cores produces drag forces that cause them to spiral towards each other and once the stars become too close to one another the configuration becomes unstable (Iben and Livio, 1993). Such a scenario could result in the rapid, violent ejection of the matter in the common envelope. There is considerable uncertainty about the effectiveness of envelope liberation of this type. Simulations by Sandquist et al. (1998) calculated fairly high efficiencies for this process, of the order of 40%. These models also showed that most of the mass was ejected towards the equatorial plane.

Finally, consider the possibility that the secondary does not spiral all

the way in to merge with the core, but instead enters an extremely close binary orbit. In the period after the CE ejection the two stars will orbit rapidly in an environment rich with circumbinary gas (Sandquist et al., 1998). Spiral shocks driven by the rotation of the companion heat the gas, and may be capable of driving a fast wind from the source. This scenario is highly speculative but may provide a mechanism for driving explosive energy releases or fast winds during the PPN phase (Frank, 1999).

Accretion disk winds

It has also been suggested that accretion disks play a role in shaping PNe. An accretion disk is unlikley to be able to survive the long main sequence lifetime of the central star of a planetary nebula (Frank, 2004; Balick and Frank, 2002). As such, binary interactions at late evolutionary stages seem the most likely source of accretion disks. Disks may form around a companion star via Roche lobe overflow or wind accretion as modelled by Morris (1987) and Mastrodemos and Morris (1998) and thereafter the orbiting companion star is capable of producing a disk-driven fast collimating outflow (Soker and Rappaport, 2000).

Alternatively, tidal shredding of the companion star could cause it to accumulate as a disk around the primary star which would then be the source of the disk-driven bipolar outflow (Nordhaus and Blackman, 2006). It is also possible that a disk may form around the primary star after a common envelope ejection has taken place (Soker and Livio, 1994; Reyes-Ruiz and López, 1999). This last scenario is very interesting as theoretical simulations by Reyes-Ruiz and López (1999) indicate that the accretion rate will decrease as a power law over time, thus implying a finite lifetime for the disk. This may provide an explanation for the transient nature of some of the outflows observed in PNe.

Although considerable work has been done on ascertaining whether or not it is likely that accretion disks will form in binary systems, there is still work to be done to understand how these disks will launch a collimated wind in PNe (Frank, 1999). The most promising models rely on the presence of

magnetic fields embedded in the rotation disk. This mechanism for launching jets is referred to as magneto-centrifugal launching and is explored in some detail by Frank and Blackman (2004) and Frank (2004).

1.3.4 Magnetic fields

The magnetised wind blown bubble (MWBB) model relies on the presence of a global magnetic field originating in the evolved star to produce bipolar outflows. It was first proposed by Chevalier and Luo (1994). In their model a dipole field at the surface of the post-AGB star is transported outwards by an expanding stellar wind, as in the solar case. The field thus has its end-points tied to a rotating stellar surface. Conservation of magnetic flux implies that the poloidal component of this field scales as $\frac{1}{r^2}$, and the toroidal component as $\frac{1}{r}$. Thus at large radii the field becomes predominantly toroidal (Balick and Frank, 2002). The field is assumed to be dynamically insignificant until the fast wind compresses the gas into a shocked region. Compression in this shocked region strengthens the magnetic field to such an extent that the magnetic energy density in this region is greater than the thermal energy density. Hoop stresses associated with the toroidal field will preferentially direct material along the dipole axis of the magnetic field. This effect will dominate over isotropic gas pressure in the region, resulting in a bipolar outflow (Chevalier and Luo, 1994). The principal parameter describing the effect of the wind-driven bubble is the ratio of magnetic to kinetic energy density at large radii from the star. This ratio σ is given by:

$$\sigma = \frac{B_*^2 r_*^2}{\dot{M} v_w} \left(\frac{v_{rot}}{v_w} \right)^2 \tag{1.1}$$

Here B_* is the stellar magnetic field, $\dot{M}$ is the mass loss rate, r_* is the stellar radius, v_{rot} is the rotational velocity of the central star and v_w is the speed of the stellar wind (Balick and Frank, 2002). The Chevalier and Luo (1994) paper explicitly assumes that $\sigma < 1$, which translates to an approximate upper limit of $\sim$ 300 G for the stellar magnetic field in these types of models. Their work indicates that the bipolar outflows will form for

$\sigma \geq 10^{-4}$. However, numerical simulations by Rozyczka and Franco (1996) indicate that significant elongation along the poles only occurs for much larger σ values of $\sigma \geq 0.05$.

Numerical work simulating this model indicates that it is capable of producing fast jets (García-Segura and López, 2000; Garcia-Segura, 1997). Fully three dimensional models of this type are also able to convincingly reproduce ansae in a variety of configurations. In simulations where the magnetic axis of the star precesses, the jets that form also precess with the magnetic field. This could provide a mechanism for producing a multipolar structure. However, this mechanism can only help to collimate the winds as the assumed fields are too weak to be responsible for the launching process. Furthermore, this model collimates the wind at large radii ($> 10^{17}$ cm) from the central star and there is observational evidence which suggests that the wind is collimated at much closer distances (Sahai, 2004).

A fast magnetised stellar rotator may also be able to launch fast jet-like outflows via magneto-centrifugal launching processes. Explicit models of this process have been made by Blackman et al. (2001a,b) who investigate both the case of a single star and a star surrounded by an accretion disk formed after a CE ejection event. These theories rely on dynamo action to sustain or amplify the required magnetic field (Blackman, 2004). Dynamo calculations by Pascoli (1997) and Blackman et al. (2001a) argue that a classic differential rotation and convection model based on the $\alpha\omega$ dynamo model has the potential to generate extended fields in evolved stars. In such a dynamo the twisting of the magnetic field provided by Coriolis effects on rising cells in a rotating convective medium is referred to as the α effect. Further twisting of the field via differential rotation is the ω effect (Russell, 1999).

The Blackman et al. (2001a) model assumes angular momentum conservation in mass shells in the stellar core and then uses core contraction and envelope expansion to generate strong differential rotation between the core and convective envelope. Rapid rotation ($\sim$ 100 km.s^{-1}) of the core is required to sustain the magnetic field once the envelope is blown away. However, in addition to establishing the feasibility of global magnetic fields,

dynamo generated or otherwise, this class of models must investigate whether the generated magnetic fields are capable of launching and collimating the required outflows.

Blackman et al. (2001a) attempt to address the issue of collimation. In this paper the wind is radiatively driven and the dynamical influence of the magnetic field is limited to its ability to collimate this pre-existing wind. The ability of a magnetic rotator to collimate a wind can be quantified useing a rotation parameter Q given by:

$$Q/Q_{\odot} \simeq 4(\phi_c/5 \times 10^{26}\ \mathrm{G.cm^2})(\Omega_c/2 \times 10^{5}\ \mathrm{s^{-1}}) \times (\dot{M}/6 \times 10^{21}\ \mathrm{g.s^{-1}})^{-\frac{1}{2}}(V/400\ \mathrm{km.s^{-1}})^{-\frac{3}{2}} \quad (1.2)$$

In this expression ϕ_c is the magnetic flux at large distances, V is the outflow speed, Ω_c the angular velocity of the stellar core and $\dot{M}$ the mass loss rate. If $Q > 1$ then the object is expected to launch a fast self-collimated outflow, the larger the Q the stronger the collimation (Blackman et al., 2001a). Using representative outflow parameters ($V = 1000$ km.s^{-1}; $\dot{M}= 5 \times 10^{-7} M_{\odot}$.yr^{-1}) and the calculated magnetic flux from his dynamo model, Blackman et al. (2001a) calculate Q=15 for a typical late stage planetary nebula. Thus they conclude that once the magnetised core of a PPNe is exposed via mass loss or binary effects, it will be able to collimate a jet regardless of the existence of accretion disks surrounding the primary star. In contrast the MWBB model utilises winds with $Q < 1$. Thus jets formed via magneto-centrifugal launching processes require larger outflows and stronger magnetic fields than those formed via MWBB models (Balick and Frank, 2002).

There have also been several attempts to model a magnetic launching mechanism. These generally fall into two categories: the magnetic 'spring', or magnetic 'fling' mechanism (Blackman et al., 2001b). The 'spring' mechanism is of the type proposed by Contopoulos (1995). Here the field is predominantly toroidal and the magnetic energy density is comparable to the kinetic energy density of the nebula. Toroidal field pressure drives the outflow in this model. In the 'fling' model (Blandford and Payne, 1982) the outflow is driven by centrifugal forces generated by rotating poloidal field lines. The

base of the poloidal field lines are tied to either a rotating accretion disk or central star, and at large distances from the star the inertia of the gas causes the field to become increasingly toroidal. Hoop stresses associated with this toroidal field will then collimate the centrifugal outflow.

Some fraction of the magnetic energy in these magneto-centrifugal launching models may be available to power X-ray emission from the central stars. X-ray emission has been detected from several planetary nebulae including NGC 7027 (Kastner and Vrtilek, 2001), BD+30° (Kastner et al., 2000) and NGC 6543 (Chu et al., 2001; Guerrero et al., 2001), but its presence is more frequently linked to the presence of companion stars or the action of shocked winds.

While Blandford and Payne (1982) have shown that magnetic launching mechanisms can produce steady flows of matter, in the sense that the outflow engine still operates while the flow is observable, it is possible that magnetic forces may result in an outflow of a more transient nature. Matt et al. (2004) propose a magnetic explosion mechanism which results in the complete ejection of the CSE. In this model a solid core, threaded with a dipole field rotates inside an initially motionless envelope. The envelope is threaded everywhere by the dipole field originating in the core. Differential rotation between the core and the envelope results in the twisting of magnetic field lines and the subsequent development of an azimuthal magnetic field. The authors argue that as the convective envelope expands and its density decreases the relative importance of the magnetic field increases. Eventually the magnetic energy in the envelope exceeds its gravitational potential, and at that point the magnetic pressure of the azimuthal field drives off the envelope in a single short-lived event. In order to simplify the computations, the model adopts an envelope of fixed density and a steadily increasing magnetic field. The azimuthal field generated by the rotating dipole is strongest at mid-latitudes, and thus it directs the flow preferentially towards the equator and the poles resulting in a quadrupolar outflow. The simulations indicate that the envelope is completely ejected for the system if the dimensionless parameter:

$$v_c v_A v_{esc}^{-2} > 0.1, \tag{1.3}$$

where v_c is the rotational velocity of the core, v_A is the Alfvén velocity and v_{esc} the escape speed at the core. This type of transient ejection would be consistent with those observed planetary nebulae whose flows follow a 'Hubble Law' expansion $v \propto R$ (Alcolea et al., 2001). This type of flow suggests that ejecta are accelerated only for a short period and thereafter follow ballistic trajectories. Thus, they seem to require a quasi-explosive mechanism to explain their kinematics.

It is widely accepted that PNe are powered by line-driven winds. A line-driven wind is produced when photons, from the central star, transfer momentum to metal ions via the absorption and scattering of spectral line radiation in strong line transitions. Coulombic interactions transfer the momentum of the metal ions to the surrounding plasma resulting in a net outflow of the entire plasma (Castor et al., 1975). The circumstellar envelopes of AGB stars are driven outwards by radiation pressure on dust, and thus by extension it has always been assumed that the energy source of PPNe is radiation pressure. However, recent observations of PPNe have revealed that the linear momenta and kinetic energies of these objects are far in excess of what could be provided by radiation pressure alone, sometimes by up to three orders of magnitude. These large amounts of energy cannot be accounted for by line-driven winds, radiation pressure on dust or continuum-driven winds (Bujarrabal et al., 2001; Alcolea et al., 2001).

In light of these new observations, magnetic pressure becomes an attractive option to explore as the main driver of post-AGB winds. It has been calculated by García-Segura et al. (2005, 2006) that a sudden increase in the global stellar magnetic field at the onset of the post-AGB stage can lead to prominent magnetically driven stellar winds. These winds have distinctly different kinematics to the magnetised line-driven winds produced in the MWBB models and these differences may prove to be a useful diagnostic of the launching mechanism in a specific outflow. The winds are able to reproduce many of the features observed in transition objects such as high mass loss rates, extreme collimation of the developing nebular shell and high-velocity outflows. An example of a highly collimated nebula produced by magnetically driven winds in these models is given in figure 1.5. These

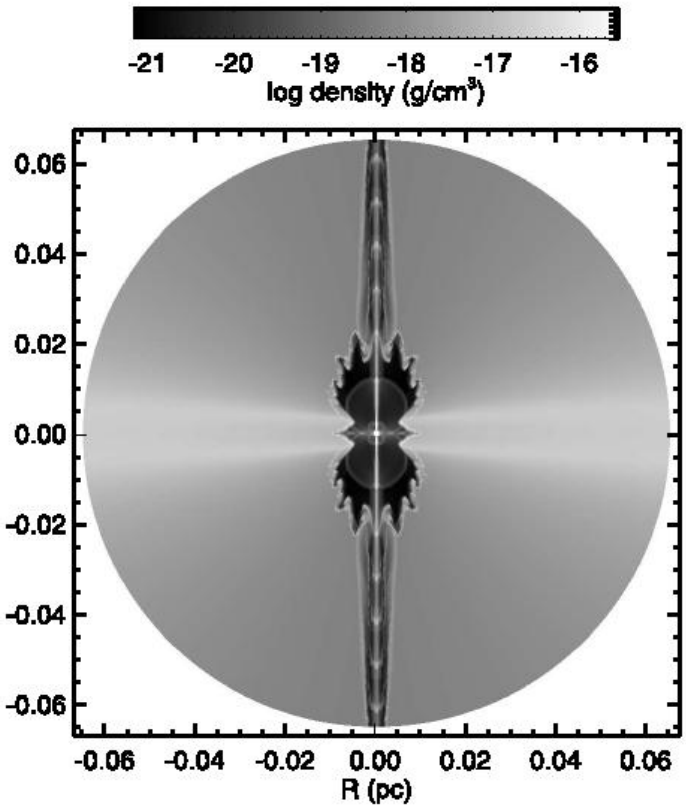

Figure 1.5: An example of a model of a planetary nebula in which the post-AGB wind is driven solely by magnetic pressure. This figure is adopted from García-Segura et al. (2005).

papers do not explore how or why this sudden increase in magnetic field would occur but suggested that a plausible scheme is that the rotation rate and field strength increase during the formation of the white dwarf. Thus the field strength increases as the core contracts and becomes exposed at the stellar surface.

The magnetic explosion mechanism proposed by Matt et al. (2004) may also be able to account for the observed high energy levels in PPNe. Blackman (2004) also suggested that dynamo-driven outflows launched by the magnetic fling mechanism proposed by Blandford and Payne (1982) may provide the required mechanical luminosity and momentum.

Although these models provide interesting mechanisms for shaping planetary nebulae, they are subject to many criticisms. Soker (1998) argues that the rotation rates required from the central star in order for models of the

MWBB type to be efficient, are unrealistically high as rotation cannot easily be preserved through AGB evolution. It is arguable that the star could reach such high rotation rates if it is spun up by the influence of a binary companion. He also takes some exception to the assumed topology of the field. These models require that the field lines circle the central star in the equatorial plane and as this is not the case for the Sun it seems that there is no real evidence to suppose that this would be the case for post-AGB stars. However, it should be noted that the Sun and post-AGB stars differ substantially in their geometry and composition. Furthermore if the magnetic field is generated by dynamo activity it will have opposite directions in the two hemispheres and this configuration will reduce the efficiency of the proposed collimation process.

Soker and Zoabi (2002) remain unconvinced by the $\alpha\omega$ dynamo model presented by Blackman et al. (2001a). This model is criticised for assuming an unrealistic angular momentum distribution and requiring very rapid rotation of the stellar core. It is deemed unlikely that each mass shell would conserve angular momentum over the course of stellar evolution, as strong coupling is expected between the convective envelope and the core. The assumption that there would be zero angular momentum transfer between the two layers is also criticised, as it is argued that any magnetic field extending into the convective layer will rapidly spin down the core (Soker and Zoabi, 2002). However, this conclusion is deemed unlikely to hold as strong field lines will collect into flux-tubes that do not provide significant drag in the envelope (Frank, 1999). It has been proposed that a binary companion could account for the spin up of the core and could perhaps maintain differential rotation rates between the two layers (Blackman, 2004).

Soker and Zoabi (2002) also claim that the equatorial polar density contrast achieved by these models is very low unless very strong magnetic fields, or very fast rotation is invoked and these effects are not very satisfactorily explained.

It is argued in several papers (Soker, 2000; Soker and Zoabi, 2002; Soker, 2006) that an $\alpha\omega$ dynamo can only be effective in the minority of stars that have been substantially spun up by the action of a companion. Therefore

magnetic fields in post-AGB stars are more likely to be the result of a turbulence generated $\alpha^2\omega$ dynamo, rooted mainly in the vigorous convective envelope of the star. In an $\alpha\omega$ dynamo, the α effect, due to convection, generates the poloidal field component, while differential rotation amplifies the toroidal component. In contrast, in the $\alpha^2\omega$ dynamo the toroidal component is amplified by convection, and the primary role of rotation is to establish the overall geometry of the magnetic field (Soker, 2000).

The magnetic field generated by an α^2 dynamo mechanism has a much lower filling factor than a global $\alpha\omega$ dynamo and consequently is unlikely to have any direct dynamical influence on the geometry of the CSE. However, the field produced by this dynamo is strong enough to cause the formation of magnetic cool spots on the stellar surface. The lower temperature of these cool spots results in a region of enhanced dust formation, thereby locally increasing the mass loss rate. These cool spots may also facilitate magnetic reconnection events (flares) which are also likely to lead to enhanced dust production (Soker and Kastner, 2003). Thus the magnetic field is only dynamically important in relatively small regions of the stellar surface. However, in Soker (1998) it is postulated that a weak global magnetic field may influence the overall geometry of a planetary nebula via the secondary dynamical influence of the magnetic cool spots. In this paper the enhanced magnetic activity towards the equator of the star results in a greater number of cool spots being formed there. Thus the star experiences higher mass loss rate at the equator resulting in the formation of an axisymmetric envelope. This mechanism may be responsible for the formation of some of the observed dense torii surrounding post-AGB stars.

1.4 Observations of Magnetic fields in AGB and post-AGB stars

There are an increasing number of detections of magnetic fields around post-AGB stars. The most convincing evidence of their existence comes from polarised maser emission. Any detected polarisation structure is interpreted

as due to Zeeman splitting by the stellar magnetic fields. These include observations of SiO masers by Kemball and Diamond (1997), of H_2O masers by Vlemmings et al. (2002, 2005) and Vlemmings et al. (2006) and of OH masers by Bains et al. (2004, 2003); Szymczak and Gérard (2004, 2005) and Miranda et al. (2001). Approximately these measurements place the magnetic field in SiO maser clumps at $\sim$1 G near the AGB stellar surface at $\sim$1 AU , decreasing to 100 mG in the H_2O maser region and $\sim$1 mG at the OH masers which are located at larger radii. There may be some uncertainty in the determined magnetic field. In particular, it has been suggested that a non-Zeeman interpretation of the polarisation of SiO masers may be possible. In the case of a non-Zeeman interpretation the magnetic fields strengths will be considerably less than those derived by applying a Zeeman interpretation (Wiebe and Watson, 1998).

Reid et al. (1979) suggests that one might extrapolate the average magnetic field at the surface of the star, B_*, from these maser results by assuming that the field strength varies as a power of the distance from the central star with some exponent α. Thus B_* is obtained by:

$$B_* = B_{maser} \left(\frac{R_*}{R_{maser}} \right)^{-\gamma} \tag{1.4}$$

Such an extrapolation would only be valid if the magnetic field is of a global nature and originates in the central star. It is interesting to note that current magnetic field estimates in the different species of maser emission obey this distance dependence. These maser measurements imply an γ value of between 2 and 3 (Reid, 1990; Vlemmings et al., 2005). Such extrapolations frequently imply stellar magnetic fields well in excess of 10^3 G. The diagram in figure 1.6 illustrates current magnetic field estimates from various species of masers and their distance dependence.

An obvious drawback of measuring magnetic fields in masers is that the masers exist in discrete gas clumps hence one can only sample magnetic field structures in a local sense (Bains et al., 2004). Soker and Kastner (2003) and Soker (2006) argue that these observed magnetic fields can be attributed to local ejection events or magnetic flaring which then gives rise to localised

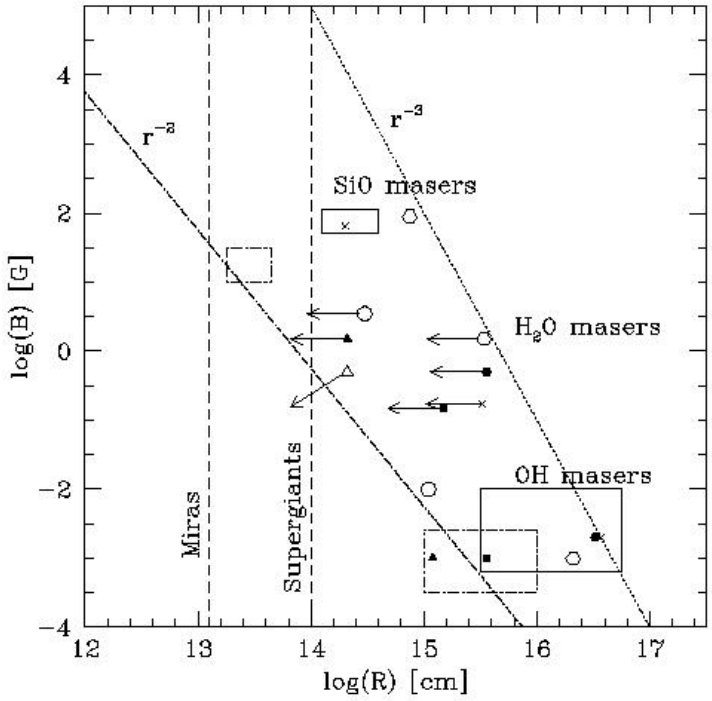

Figure 1.6: Magnetic field strength, B, as a function of distance, R, from the star. This figure is taken from Vlemmings et al. (2005). The dashed boxes indicate magnetic field strength estimates from OH and SiO masers in Mira stars, the solid boxes are those for the supergiants. The symbols represent magnetic field strength estimates in individual stars (solid and open triangles: U Her, solid squares: S Per, crosses :VY CMa, open circles: U Ori, open hexagonal: VX Sgr).

'magnetic clouds'. These are analogous to the magnetic clouds formed by the Sun as a result of impulsive mass loss events which are characterised by stronger than average magnetic field strengths. In particular the very fast variation of the polarisation of OH 17.7-0.2 seems to support a local origin for the magnetic field (Soker, 2006). Recent magneto-hydrodynamic simulations of the star Betelgeuse suggested that locally strong magnetic fields could be generated by a local dynamo based in the convective envelope of the giant star (Dorch, 2004). It is possible that a similar mechanism could generate magnetic fields in post-AGB stars. This type of localised magnetic action could not play a global role in shaping PNe. However Bains et al. (2004) counter this argument by suggesting that while 'magnetic clouds' may be present in AGB objects in post-AGB objects, the concentrated field clumps will be indistinguishable from the general outflow due to gas diffusion effects. Therefore the magnetic field detected in the maser emission is representative of the global distribution.

Soker (2006) also suggests that the detected magnetic fields may be the result of a magnetically active binary companion or of an accretion disk surrounding a companion. The accretion disk will enhance the magnetic field of the accreted gas thereby producing the required stronger fields.

Further evidence of magnetic fields in post-AGB stars is provided by recent observations of PNe with the VLT (Jordan et al., 2005). This survey consists of spectropolarimetric observations between 3500 and 5900 Å of the central stars of four PNe. It conclusively detected kilogauss magnetic fields in at least two of the objects (NGC 1360 and LSS 1362) with less certain detections in the other two objects (EGB 5 and Abell 36). This is the first direct detection of magnetic fields in the central stars of PNe, and as such provides an important independent confirmation of the existence of such fields.

1.5 OH masers

1.5.1 The structure and spectrum of hydroxyl

Hydroxyl is a diatomic molecule with an unfilled electron shell and various internal spins. As a result its energy levels are fairly complex. The overall angular momentum of OH excluding nuclear spin is given by $\mathbf{J}=\mathbf{K}+\mathbf{L}+\mathbf{S}$, where $\mathbf{K}$ corresponds to the rotational angular momentum of the nuclei, $\mathbf{L}$ is the orbital angular momentum of the electrons and $\mathbf{S}$ is the electronic spin (Cook, 1977). The hydroxyl molecule is an important exception to the general rule that the ground states of molecules are Σ states; the electronic ground state of OH is a Π state with $\mathbf{L}_z$=1. The symbols Σ, Π and Δ are used to denote $\mathbf{L}_z$= 0, 1, 2 respectively. Therefore the angular momentum of the electronic ground state is given by $\mathbf{J} = 1\pm\frac{1}{2}$, giving rise to two rotation ladders denoted by $^2\Pi_{\frac{1}{2}}$ and $^2\Pi_{\frac{3}{2}}$ (Cook, 1977). The subscripts indicate the values of J_z and the superscript 2 is used to denote the two possible spin orientations. Of these two sets of states the $^2\Pi_{\frac{3}{2}}$ sequence has the lower energies. Interaction with the next electronic state removes the degeneracy between states with $+J_z$ and $-J_z$, introducing a parity splitting known as Λ doubling. Thus the two levels of an Λ doublet have opposite parity; in the $^2\Pi_{\frac{3}{2}}$ ground states the upper level has + parity and the lower has − parity (Elitzur, 1992). There is a further contribution to the energy of the hydroxyl molecule caused by the hyperfine interaction with the nuclear spin $\mathbf{I}$ (I=$\frac{1}{2}$). Each rotation state is thus split into a quartet of levels according to parity and the value of the total angular momentum $\mathbf{F}=\mathbf{J}+\mathbf{I}$ (Elitzur, 1992). In the ground state $^2\Pi_{\frac{3}{2}}$ F can be either 2 or 1. The quartet of levels in this state is as given in table 1.1 (Cook, 1977). OH allowed transitions follow the simple dipole selection rules, which require a parity change and $\Delta\mathbf{F}$=0, $\pm$1 (but F=0 $\rightarrow$0 is forbidden). The wavelengths of the ground-state transitions are approximately 18 cm. The F-conserving lines, with frequencies of 1665 and 1667 MHz are called main-lines and the F-changing ones at 1612 and 1720 MHz are satellite-lines (Elitzur, 1992).

It is interesting to note that in most extended sources the main-lines

Level	Parity	**F**	Energy (MHz)
4	+	2	1720
3	+	1	1665
2	−	2	53
1	−	1	0

Table 1.1: Energy levels for the $^2\Pi_{\frac{3}{2}}$ ground state of OH

appear in either weak emission or absorption with nearly equal strengths, as would be expected from a source in thermal equilibrium, whereas the satellite-lines almost always exhibit an anomalous pattern. One of the satellite-lines may appear in absorption while the other is in emission or the strength of emission exceeds what would be expected from the main-line behavior. This behaviour is explained by Elitzur (1992) as outlined below. It begins by considering the energy level diagram in figure 1.7. The main-lines connect levels with the same overall angular momentum **F** in the different components of the Λ-doublet. These couple to levels that are simply the parity image of each other in the excited rotation states. The radiative transition strengths and selection rules for the two halves of the Λ-doublet are very similar and can be considered to be identical to a first approximation. Therefore the population of each half of the Λ-doublet is expected to be approximately the same in each rotation state, and the main-lines should be in equilibrium to a first approximation. However the situation is quite different for the satellite-lines. These lines connect levels with different F values which, in turn, couple to different levels in the excited rotation states. These levels are subject to entirely different radiative decay patterns owing to the dipole selection rules. Thus the satellite-line excitations involve a rather asymmetric pattern for cycling of molecules and these transitions are more easily inverted than their main-line counterparts.

1.5.2 OH masers in late-type stars

Late-type stars provide, as a group, the greatest variety and most consistent display of strong maser emission. This emission is detected in a variety of

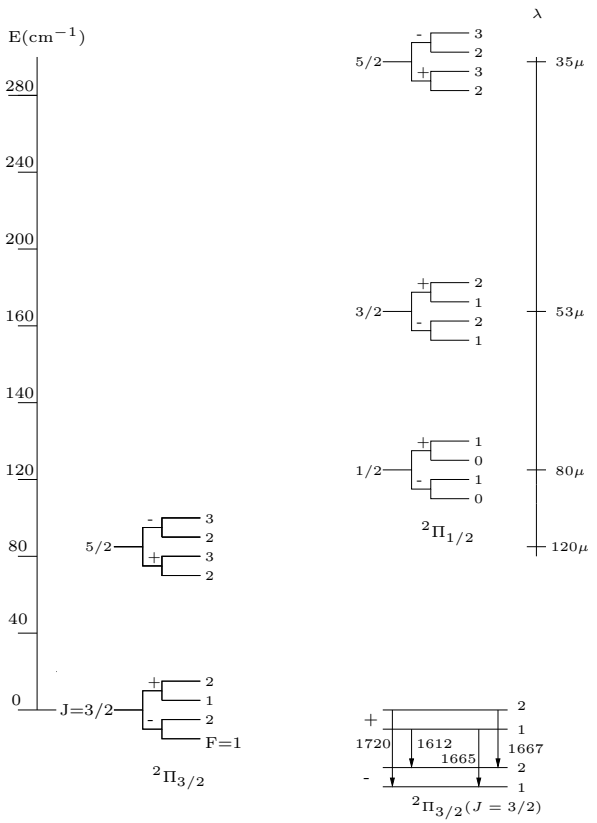

Figure 1.7: Rotation levels of OH. Above are all the rotationally excited levels that couple to the ground state via a radiative (dipole) transition (Elitzur, 1992).

transitions and molecules. OH emission has been detected in OH/IR stars in all of the ground-state lines except for the one at 1720 MHz. The properties of 1612 MHz and main-line masers are quite different in late-type stars, indicating that the transitions are inverted under different circumstances at somewhat different locations (Elitzur, 1992). For historical reasons stars emitting more strongly in the main-lines are referred to as Type I OH/IR stars and those with stronger 1612 MHz emission are Type II.

Type II OH/IR stars - Satellite-Lines

The 1612 MHz maser emission from late-type stars has a characteristic double-peak profile with two strong emission peaks separated in velocity by

20-50 km.s^{-1}. The two emission features tend to have abrupt outer edges and more gradually tapering inner edges. Although the intensity and shapes of the two peaks are generally different in any individual source there is no statistical difference in the shape and strength of the red- and blue-shifted peaks (Elitzur et al., 1976). This profile can most easily be explained as maser emission from a slowly expanding shell. The red- and blue-shifted components correspond to the front and back of the shell respectively. Their velocity separation is twice the shell expansion velocity and the mid-point corresponds to the stellar velocity (Elitzur, 1992).

The regular variability of late-type stars provides a rare opportunity for identifying the underlying pump mechanism of their maser emission. An extensive monitoring project by Harvey et al. (1974) demonstrates that 1612 MHz maser emission and IR radiation from OH/IR stars vary together with almost no phase delay. This result is hard to reconcile with a collisional pump and it essentially establishes IR radiation as the primary inversion pump mechanism (Elitzur, 1992). Detailed model calculations conclude that pumping by the circumstellar dust IR radiation provides an adequate explanation for the 1612 MHz emission observed in OH/IR stars. Pumping occurs through 35 μm and 53 μm excitations of the $^2\Pi_{\frac{1}{2}}(J=\frac{5}{2})$ and $^2\Pi_{\frac{1}{2}}(J=\frac{3}{2})$ states respectively. Because the spontaneous decay rates of transitions from the $^2\Pi_{\frac{1}{2}}$ to the $^2\Pi_{\frac{3}{2}}$ ladder are much slower than those which proceed directly down the $^2\Pi_{\frac{1}{2}}$ ladder, the molecule usually follows the route $^2\Pi_{\frac{1}{2}}(J=\frac{5}{2}) \longrightarrow {}^2\Pi_{\frac{1}{2}}(J=\frac{3}{2}) \longrightarrow {}^2\Pi_{\frac{1}{2}}(J=\frac{1}{2})$. From this final state the only possible decay is to the $^2\Pi_{\frac{3}{2}}(J=\frac{3}{2})$ ground state, which completes the cycle (Elitzur et al., 1976). Such a cascade is expected to strongly invert the 1612 MHz transition provided that the final transition is optically thick. In order to meet this conditions for optical thickness, high mass loss rates of $\sim 10^{-5} - 10^{-6}\, M_{\odot}.\mathrm{yr}^{-1}$ are required in stars which generate strong satellite-line emission (Elitzur, 1992). Such high mass loss rates are generated for relatively short periods of time at the very late evolutionary stages of AGB stars.

The theoretical model calculations predict that the 1612 MHz masers in OH/IR stars are saturated and the production of each maser photon re-

quires about four far-IR pump photons (Elitzur et al., 1976). Werner et al. (1980) performed simultaneous IR and radio observations of five 1612 emitters. Their result show that the ratio of IR photons to maser photons is indeed 4:1. Additionally their results show that the observed ratio of the two types of radiation remains constant throughout various phases of the stellar cycle, as would be expected for a saturated maser. Thus this experiment provides strong observational support for the theoretical calculations in Elitzur et al. (1976) .

Type I OH/IR stars - Main-line emission

Main-line inversion is fundamentally different from that of satellite-lines. Anomalous emission at main-line frequencies is a much more selective phenomenon and is much more difficult to explain. The reason is that the energy levels diagram is symmetric with regard to the two halves of the Λ-doublet and for every cycle that carries molecules from negative to positive parity there is an image cycle that carries molecules in the opposite direction with equal efficiency (Elitzur, 1992). Therefore main-line inversions require some parity selectivity in the pumping process. This is in contrast to the satellite-lines where anomalies are due to the structure of the energy level diagram and photon trapping effects, rather than to any unusual pumping conditions (Elitzur, 1978).

The main-line inversions also arise from rotational excitations by IR radiation. In order to produce a ground state inversion, the excitation of the rotational levels should prefer the upper Λ-doublet components. This is because the resulting cascade back to ground, proceeding mostly within each rotation ladder, preserves the sense of excitation selectivity to produce a main-line inversion (Elitzur, 1978). A selectivity in the excitation process is possible because the energy separation of the Λ-doublet increases with increasing rotation angular momentum. As a result, a transition from the ground state to the upper halves of any rotation state has a higher frequency than its image transition to the lower half. Therefore rotational excitations by a radiation field whose photon occupation number increases with fre-

quency will pump more photons into the upper Λ-doublet of each rotation level producing a main-line inversion (Elitzur, 1978).

Calculations show that the most important thing in establishing an inversion is the dust temperature, T_d, and main-line inversions are produced when $T_d > 100\ K$ (Elitzur, 1978). The main-lines are not saturated and their inversion is not a very stable effect. An increase in the OH density, for instance, could eliminate the inversion altogether. Model calculations show that the relative strengths of the 1665 MHz and 1667 MHz emissions is sensitive to properties of the circumstellar dust. They show that 1667 MHz emission is stronger for dust temperatures in the range 150-280 K with a dust spectral index of $1 < p < 1.5$. Higher dust spectral indices result in the 1665 MHz line being the more dominant emission. Thus main-line maser emission can provide information about the dust properties of the observed source (Elitzur, 1992). Field (1985) discusses the process of competitive gain between hyperfine transitions in OH and in particular examines the relative strengths of the different transitions under a variety of dust conditions.

1.6 OH maser interferometry

As discussed in section 1.5.2 the double-peaked profile of the OH maser emission typically observed from OH/IR stars is interpreted as arising in a spherically symmetric, uniformly expanding shell. This explanation was first suggested by Reid et al. (1977) and the first high resolution interferometric maps of an OH/IR source with such a spectrum, presented by Booth et al. (1981), provided considerable support for this interpretation. These maps of OH 127.8-0.0 display the predicted structure of barely resolved emission caps at the velocity extremes which open out into partial shells at more intermediate velocities. Thereafter numerous interferometric observations of OH/IR stars confirm that the spatial distribution of the OH maser emission from these sources is broadly consistent with this simple model (Norris et al., 1982; Bowers et al., 1983; Chapman et al., 1984; Diamond et al., 1985). In these maps full shells of emission are seldom resolved and the emission is often asymmetric and clumpy. However, it does appear to outline portions

of ring-like structures. In some cases the extreme blue- and red-shifted emission features are positionally offset from one another. This is in contrast to the predictions of the model which place the extreme blue- and red-shifted emission features directly in front of and behind the star respectively and thus these features should be positionally co-incident. Deguchi (1982) explains these departures from the model predictions as occurring as a result of random velocity fluctuations in the circumstellar envelope.

Interferometric observations of OH maser emission from post-AGB objects have revealed a variety of interesting structures including bipolar outflows (Zijlstra et al., 2001) and expanding disks (Gómez et al., 2006). The more typical expanding shell type emission has also been detected from these objects. The OH spectra of these objects frequently display departures from the standard double-peaked profile (Deacon et al., 2004) and thus is not surprising that the masers in these objects trace different kinematic structures.

Chapter 2

Very Long Baseline Interferometry

2.1 Introduction

The development of radio-interferometry started in the 1940's (Ryle and Vonberg, 1946) and led to the development of earth rotation aperture synthesis, a technique used by both connected element and Very Long Baseline Interferometry (VLBI) arrays. Aperture synthesis has provided radio astronomers with an exceptionally powerful imaging tool (Thompson et al., 2001). These arrays are used to synthesise a larger effective aperture, with superior angular resolving power, over that provided by a single radio telescope alone.

The basic theory which renders interferometry possible is the van Cittert-Zernike theorem which demonstrates that there is a Fourier transform relationship between the brightness distribution of an astrophysical source and the complex spatial coherence function of the radiation in the plane orthogonal to the source direction (Born and Wolf, 1980).

This relationship is given below:

$$V(u,v) = \int B(l,m) e^{-i2\pi(lu+mv)} e^{-j\omega\tau} dl\, dm \tag{2.1}$$

Here $V(u,v)$ is the complex coherence function, $V(u,v) =< E(\mathbf{r_1}) E^*(\mathbf{r_2}) >$,

where $E(\mathbf{r_1})$ indicates the electric vector phasor of the electromagnetic radiation from the source measured at antenna position vector $\mathbf{r_1}$, <> indicates ensemble averaging and * denotes complex conjugation. The separation vector $\mathbf{r_1} - \mathbf{r_2}$ can be rewritten in terms of coordinates (u, v) the projection of $(\mathbf{r_1} - \mathbf{r_2})$, measured in units of wavelength, onto a plane perpendicular to the field centre direction of the incident radiation. The (l, m) coordinates are direction cosines of the angular position of the source on the sky (Clark, 1989; Thompson et al., 2001).

The Fourier transform relation holds in the limiting case of spatially incoherent incident radiation, of limited angular extent and observed in the far field.

The condition of spatial incoherence allows the relationship between the complex coherence function and the source electromagnetic radiation to collapse to such a simplified expression. Spatial incoherence is a reasonable assumption for most cosmic radio sources.

The antenna separation vector $\mathbf{r_1} - \mathbf{r_2}$ can be expressed in terms of three components (u, v, w) where (u, v) are in the plane perpendicular to the direction of the source radiation and w is the component in the direction parallel to the source radiation. In reality the complex coherence function is a function of all three of these terms. It can thus be expressed by the following Fourier transform relation involving these three variables and their Fourier conjugate variables $(l, m, \sqrt{1 - l^2 - m^2})$.

$$V(u, v, w) = \int B(l, m) e^{-i2\pi(lu+mv+w(\sqrt{1-l^2-m^2}-1)} dldm \qquad (2.2)$$

Here the (l, m) co-ordinates are direction cosines measured with respect to the u and v axes respectively and the $\sqrt{1 - l^2 - m^2}$ is the third direction cosine measured with respect to the w axis. The assumption that the observed source is of limited angular extent allows one to neglect the final term in the exponent of the above expression thus simplifying it to a two dimensional transform.

In an interferometer, the source radiation is detected by antennas at widely-spaced separations and the antenna output voltages are crosscorre-

lated. Once correlated, the products are referred to as visibilities (Thompson, 1989). The visibility the correlator writes out is thus a sample of the complex coherence function $V(u, v)$ at the coordinates (u, v) which corresponds to the projected orthonormal separation of the two antennas whose outputs were correlated. The presence of multiple antenna pairs means that a number of $V(u, v)$ values are sampled. Earth rotation causes the (u, v) values to vary during the course of the observation. Thus an interferometer obtains a sampling of the coherence function over the (u, v) plane, although this sampling may often be sparse. The Fourier transform relation can, in principle, be inverted to yield the desired image of the source (Clark, 1989).

In general, the correlator outputs do not exactly replicate the desired complex coherence function as the signal has been corrupted by a variety of instrumental, propagation and geometric effects at each antenna. However through careful application of appropriate calibration steps it should be possible to recover the true coherence function.

There are two kinds of interferometers. The original interferometers were all of the connected-element variety and many current interferometers are still of this design including the Very Large Array (VLA) [1], the Multi-Element Radio Linked Interferometer Network (MERLIN) [2] and the Atacama Large Millimeter Array (ALMA) [3]. In this arrangement, the antennas are close enough to one another to allow real time correlation of the signal. A single local oscillator signal is distributed to each antenna to be used in the receiving electronics and the detected signals are sent via a radio link, waveguide or fibre optic cable to a central correlator and correlated in real time. Obviously such an arrangement is limited by the maximum distance over which it is technically practical to connect all the interferometer elements together (Walker, 1989); this distance has been steadily increasing with advances in network bandwidth and infrastructure.

With time it became clear that many radio sources have structures that cannot be resolved by interferometers with baselines of a few hundred kilo-

[1] www.vla.nrao.edu
[2] www.merlin.ac.uk
[3] www.vla.nrao.edu

meters. The technique of VLBI was developed in the late sixties, in response to this realisation. This style of interferometry doesn't require communication between antennas and as such there is no limit to the baseline lengths. In VLBI, each station has a separate high quality local oscillator and clock signal and the signals from the antennas are recorded on high density digital tape or high capacity disk drives to be correlated at a later stage (Thompson et al., 2001). While connected-element and VLBI interferometry are fundamentally similar, there are differences which complicate the calibration and analysis of VLBI data sets; the most important differences arise because of the use of separate time and frequency standards, uncorrelated atmospheric phase errors at each array and because of the increased difficulty of determining the geometry of the array.

As mentioned previously, the measured visibilities are corrupted by several instrumental effects; this chapter aims to discuss the origins of these effects and the means by which they can be determined and removed.

2.2 Geometric effects

Consider the geometry of two antennas observing an object at a field center direction $\mathbf{s}$. On inspection of the diagram in figure 2.1 it is evident that the radiation from a plane wave reaches antenna 2 later that it arrives at antenna 1. This offset is referred to as the geometric delay and has a value of $\tau_g = (\mathbf{r_1} - \mathbf{r_2}).\mathbf{s}$. Thus a delay must be inserted into the signal path to ensure that the signals arrive at the correlator simultaneously.

The correlator adopts a coordinate reference frame; early VLBI networks used a designated reference antenna on each baseline as the center of the reference frame. Later interferometers, such as the VLBA, use the earth's geocenter. In both cases the signal from each of the antennas is aligned with the time of arrival of the signal at the centre of the correlator reference frame (Thompson, 1989). For a real interferometer, the geometric delay is not the only mechanism which causes the signal at one antenna to be delayed with respect to another. In order to determine the total delay it is necessary to consider the effects associated with the antennas being located at different

altitudes, the shape of the earth and viewing the source at different elevations through the atmosphere (Formalont and Perley, 1989). A further geometric effect to be compensated for is the Doppler shift of the observed spectral line induced by the motion of the correlator reference frame relative to the source (Reid, 1995).

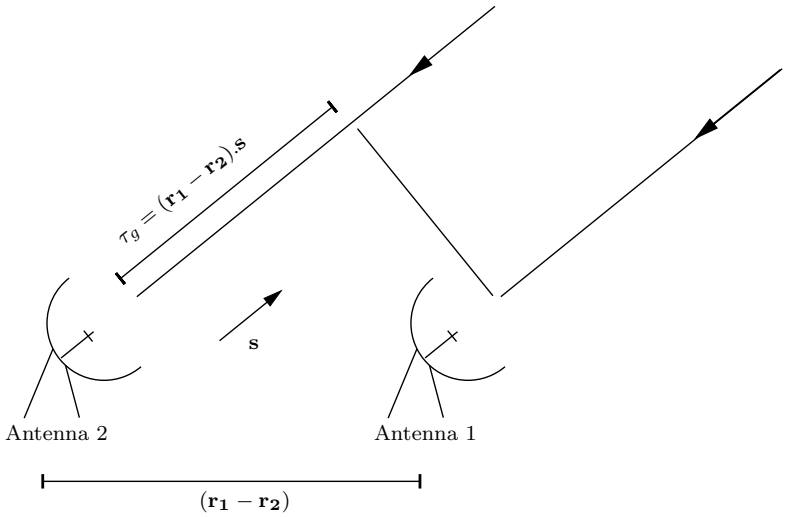

Figure 2.1: Geometric delay between antennas.

2.3 Atmospheric effects

Refractive effects in the troposphere and the ionosphere also cause signal delay between antennas. The extra time needed to traverse a medium with refractive index n compared to travelling the same distance in free space is given by $\delta t = \int (n-1)ds$ where ds is an element of the path length (Moran and Dhawan, 1995). The atmospheric delay differs for each antenna because of their different altitudes and because the separation of the antennas demands that they observe the source at different elevations. Path length through the atmosphere, f, increases with increasing zenith angle as $f = \sec(z)$, where z is zenith angle.

The troposphere or neutral atmosphere is non-dispersive at frequencies below 300GHz and its refractive effects are considered to have two origins;

fairly constant dry component which gives excess travelling time of 8 ns at zenith and a variable wet component which requires measurements of the total water vapour content to estimate (Formalont and Perley, 1989).

In contrast, the ionosphere is a dispersive medium which gives an excess path length in the zenith direction:

$$L_i = -40\nu^{-2}N_e, \tag{2.3}$$

where the N_e is the electron density in the plasma (Moran and Dhawan, 1995). The subscript i indicates that the excess path length is introduced by the ionosphere. An important feature of the ionosphere is that it has a different refractive index for left- and right-circularly polarised radiation, ie it is birefringent. Consequently a linearly polarised wave will have its plane of polarisation rotated as it propagates through the medium.

This phenomenon is known as ionospheric Faraday rotation (IFR) and it causes a differential phase offset between right- and left-circularly polarised radiation of:

$$\gamma^{R-L} = \frac{2\pi}{c\nu^2}\int \nu_p^2\nu_B cos\theta \; ds, \tag{2.4}$$

where ν_p is the plasma frequency, which is dependent on ionospheric electron density, ν_B is the gyrofrequency and θ is the angle between the earth's magnetic field and the direction of propagation (Thompson et al., 2001). This expression demonstrates that there are strong variations of Faraday rotation with observing geometry and that the effect is greater at lower frequencies. The diurnal variation of the electron density due to variable exposure to ionising radiation from the sun will also cause the Faraday rotation to change significantly over time. The electron density will also vary globally with the solar cycle. Thus the effects of Faraday rotation will vary as a function of source position, antenna location and local ionospheric conditions as a function of time. Faraday rotation has important consequences for polarisation observations at frequencies below approximately 2 GHz (Cotton, 1995).

2.4 Receivers and LO down-conversions

The incident radio-frequency signals are processed by the antenna receiver systems. Although the details of receiver systems vary widely from antenna to antenna, it is useful to consider the signal path through a typical receiving system. A schematic of a typical VLBI signal path is given in figure 2.2. This section follows the discussion in chapter 9 of Thompson et al. (2001).

A common feature of coherent radio receivers is that of superheterodyne frequency conversion whereby the incoming radio signal is mixed with a local oscillator signal in order to convert it to a more convenient intermediate frequency. If the incoming monochromatic signal at antenna one (taken to be the reference antenna) is represented as $S = S(t)e^{j2\pi\nu t}$, then the same signal arriving at antenna two time τ_2 later will be $S(t)e^{j2\pi\nu(t-\tau_2)}$. Here it is assumed that τ_2 subsumes all the possible causes of pre-detection delay relative to the reference antenna. The local oscillator systems at each antenna can be considered to have phases:

$$\begin{aligned} &2\pi\nu_{LO} + \theta_1 \\ &2\pi\nu_{LO} + \theta_2, \end{aligned} \tag{2.5}$$

where ν_{LO} is the frequency of the local oscillator and θ_1, θ_2 represent the local oscillator phase. In the case of upper sideband conversion the phase of the signals after mixing is as given below:

$$\begin{aligned} \phi_1 &= 2\pi(\nu - \nu_{LO})(t - t_{c1}) - \theta_1 \\ \phi_2 &= 2\pi(\nu - \nu_{LO})(t - t_{c2}) - 2\pi\nu\tau_2 - \theta_2 \end{aligned} \tag{2.6}$$

Here the t_{c1} and t_{c2} terms represent the clock errors at each of the antennas.

At a later stage in the processing the correlator will attempt to align the two incoming signals in time. In order to achieve this the phase at antenna 2 will be advanced by the instrumental delay τ_2'. The instrumental delay τ_2' is the best estimate of the total delay at the time of correlation and the final

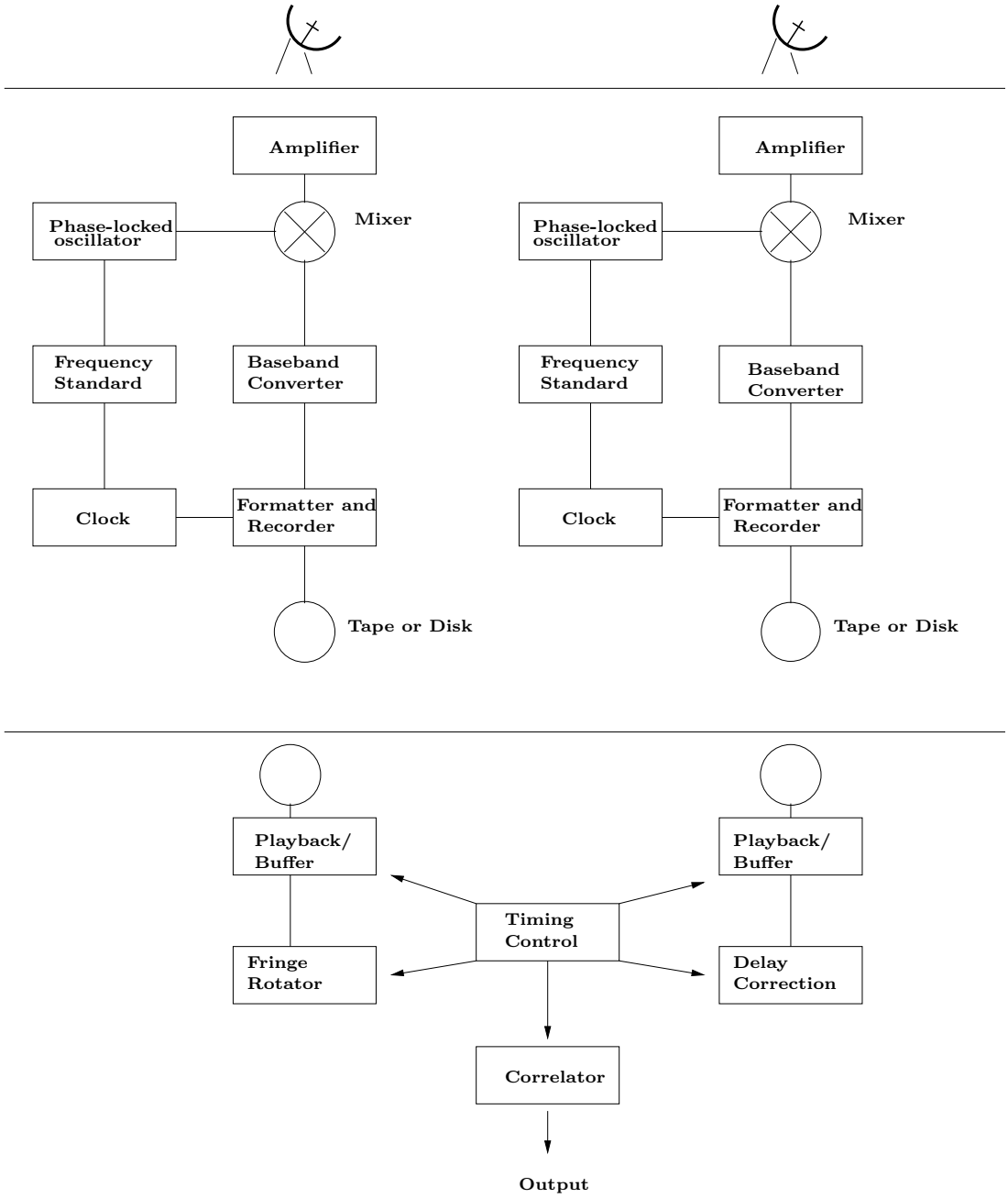

Figure 2.2: A schematic of a typical VLBI signal path, adapted from Thompson et al. (2001).

phase after the advancement has taken place is:

$$\phi_2 = 2\pi(\nu - \nu_{LO})(t - t_{c2} + \tau_2') - 2\pi\nu\tau_2 - \theta_2 \tag{2.7}$$

Thus the final phase of the crosscorrelation of these two signals is given as below:

$$\begin{aligned}\phi_{12} = &2\pi\nu_{LO}\tau_2 + 2\pi(\nu - \nu_{LO})(t_{c2} - t_{c1}) \\ &+ 2\pi(\nu - \nu_{LO})(\tau_2 - \tau_2') + \theta_2 - \theta_1\end{aligned} \tag{2.8}$$

The first term in this expression arises because the instrumental delay is inserted after the signal has been mixed with the LO signal. The variation of τ_2 with time means that the crosscorrelation output will be modulated by quasi-sinusoidal fringes and this term must be removed via process known as fringe rotation. The fringe rotation effectively rotates the phases of the correlated output by an amount of $2\pi\nu_{LO}\tau_2$ (Thompson, 1989). The subsequent terms arise from clock errors, errors in the delay model and local oscillator phase variation respectively. Thus by examining the above expression it is clear that propagation through the atmosphere and the antenna receiving systems introduces an excess phase term $\Delta\phi$ to the incoming signal. In interferometry it is common to refer to the group-delay τ, phase-delay θ and phase-delay rate $\dot{\theta}$ of the incoming signal these terms are all related to the introduced excess phase via the following relations:

$$\begin{aligned}\tau &= \frac{1}{2\pi}\frac{\partial\Delta\phi}{\partial\nu} \\ \theta &= \frac{1}{2\pi}\frac{\Delta\phi}{\nu} \\ \dot{\theta} &= \frac{1}{2\pi}\frac{\partial(\frac{\Delta\phi}{\nu})}{\partial t}\end{aligned} \tag{2.9}$$

Thus far the focus has been on the effect of the receivers and LO chain on the phase of the signal. A complete time-variable gain factor is sufficient to characterise the total frequency-independent voltage gain the signal

experiences as a result of its path through the electronics. The bandpass filters of the receiving system may have variable gain across the observed spectrum, however, and this effect has to be taken into account in spectral line observations (Diamond, 1989). Thus the cumulative receiver response to an incoming signal $S_i(t) = S_i(\nu)e^{2\pi\nu}$:

$$S_i'(\nu) = G_i(t)B_i(\nu)S_i(\nu)e^{2\pi(\nu-\nu_{LO})(t-t_{ci}+\tau_i')-2\pi\nu\tau_i-\theta_i}, \tag{2.10}$$

where $G_i(t)$ is the time-variable receiver system gain and $B_i(\nu)$ is the frequency-dependent gain of the net bandpass response.

The discussion in the previous sections has served to illustrate that the correlated signal appears at a group delay, phase-delay rate and phase-delay which is dependent on several factors including the geometry of the interferometer, the atmosphere, the instrumental hardware in the receivers and electronics.

In connected element interferometry it is usually possible to measure and model the effects of geometry sufficiently well that the difference between the actual delay and the calculated instrumental delay is negligible. In VLBI, absolute *a priori* determination of the delay is not possible. The delay may be affected by instrumental timing errors arising from the use of separate time standards at each antenna and there is greater uncertainty concerning the atmosphere and geometry of the array (Walker, 1989). The higher resolution of the observations also means greater sensitivity to these geometric uncertainties. The data will thus be unavoidably affected by unmodelled residual group-delays and phase-delay rates which must be removed as part of the calibration procedure.

2.5 Digitisation and correlation

The correlator forms the complex crosscorrelation function for each antenna pair after inserting the instrumental delay τ_i' into the signal path. The correlator also corrects the signal for geometric and atmospheric group-delay, phase-delay rates and phase delays in a correlator reference frame. These

corrections are generally referred to as the correlator model (Walker, 1999)

Depending on its architecture the correlator computes the complex visibilities in either the delay or frequency space. In the XF architecture the data are crosscorrelated over a range of offset delays:

$$r_{ij}(u,v,\tau) =< S(r_i,t)S(r_j,t+\tau_j'-\tau) > \tag{2.11}$$

This can be converted to the complex cross-power spectrum by taking the Fourier transform of these inputs so that:

$$r(u,v,\nu) = \int r(u,v,\tau)e^{-2\pi i\nu\tau}d\tau \tag{2.12}$$

Often this Fourier transform step is also done by the correlator.

In the alternative FX architecture, a short time series of voltages from the telescopes are first Fourier transformed and then cross multiplied in the frequency domain. In this case the correlator output is the complex visibility as a function of frequency (D'Addario, 1989). This is the chosen architecture for the VLBA correlator

Prior to correlation the signals are digitised, formatted and recorded to tape or disk. Digitisation involves both sampling and quantisation. Sampling is the process of converting a continuous time signal to a discrete time sequence of its samples. Provided that the samples are taken at twice the Nyquist frequency no information is lost. Quantisation converts a continuously-variable signal to one of a finite set of digital values, the systematic effects of the quantisation on the cross-power spectrum and the steps taken to correct them are discussed thoroughly in D'Addario (1989). Quantisation corrections depend on the type of correlator architecture.

2.6 Effect of discrete (u,v)-sampling

In practice, the interferometer cannot measure the spatial coherence function $V_\nu(u,v)$ everywhere, instead it samples the function in locii on the $u-v$ plane corresponding to the projected antenna separations over time. The sampling

can be described by a sampling function $S(u,v)$ which is zero where no data have been taken and a Dirac delta function $\delta(u,v)$ at each point at which data are sampled (Clark, 1989). The Fourier transform of the sampled visibilities can then be calculated as:

$$I_\nu^D(u,v) = \int\int V_\nu(u,v)S(u,v)e^{2\pi i(ul+vm)}dudv \tag{2.13}$$

Radio astronomers often refer to I_ν^D as the dirty image. It is related to the desired intensity distribution $I_\nu(u,v)$ as (using the convolution theorem for Fourier transforms):

$$I_\nu^D = I_\nu \star B + N, \tag{2.14}$$

where the $\star$ denotes convolution, N denotes noise and,

$$B(l,m) = \int\int S(u,v)e^{2\pi i(ul+vm)}dudv \tag{2.15}$$

is the synthesised or dirty beam corresponding to the sampling function. $B(l,m)$ is also commonly referred to as the point spread function. If the sampling of the (u,v) plane is sparse then the dirty beam will have large sidelobes that will cause the structure of the observed source to be corrupted in the dirty image I_ν^D (Högbom, 1974). It is thus necessary to have some mechanism to deconvolve these two functions in the presence of noise to obtain an estimate of the true source brightness distribution I_ν .

2.7 Polarisation

Polarisation measurements can provide useful insights into underlying astrophysical processes. As such, the technique of polarisation VLBI has proved to be an invaluable complement to the traditional total intensity measurements in both continuum and spectral line observations. The polarisation morphology of maser emission in circumstellar environments can provide estimates of magnetic field distributions at high angular resolutions and thus help to determine the relative dynamical influence of such a field (Kemball

et al., 1995). Continuum polarisation studies provide insight into the fundamental properties of the synchrotron emitting plasmas of active galactic nuclei (Wardle and Roberts, 1988).

To map the polarised brightness distribution of a radio source in all four Stokes parameters, each antenna should be outfitted with two receivers and feed systems whose responses should be, as nearly as possible, mutually orthogonal (Walker, 1989). These are typically dual-linear or dual-circular receptors. During observing, dual orthogonal polarisations are recorded at each antenna and all polarisation cross-products are formed during subsequent correlation. The VLBA uses orthogonal circular receptors.

Early VLBI networks were not very well suited to polarisation measurements. Frequently not all of the antennas in the array could record dual polarisations and mixed linear and circular receptors were often used across the array. Despite these difficulties, the first VLBI linear polarisation studies of 3C454.3 were published by Cotton et al. (1984). Further studies of milliarcsecond resolution polarisation of active galactic nuclei were reported by Roberts and Wardle (1986); Wardle et al. (1986) and Roberts et al. (1987). A series of papers by Roberts et al. (1991); Cotton (1993); Kemball et al. (1995) and Leppanen et al. (1995) document refinements in the calibration procedures of this technique.

There are a number of polarisation-dependent instrumental and propagation effects which must be taken into account when making polarisation measurements. An effect which has already been considered above is that of ionospheric Faraday rotation. This effect causes the phases of left- and right-hand signals arriving at the antenna to be offset by some unknown amount γ^{R-L}.

Imperfections in the circularly polarised feeds mean that they don't respond exclusively to the nominal polarisation. Imperfect feeds can be modelled as being sensitive to the desired polarisation plus a complex factor, labelled the D-term, multiplying the orthogonal polarisation (Conway and Kronberg, 1968). Alternatively the feeds can be modelled as responding to an elliptically polarised signal (Fomalont and Wright, 1974). In its full generality the D-term formalism is completely equivalent to the elliptical feed

representation. However the D-term treatment is more convenient as it is easily linearised for small D-terms. The voltage detected in response to incoming radiation is given by ($\mathbf{G^p}.\mathbf{E}$) where $\mathbf{G^p}$ is the feed response and $\mathbf{E}$ is the electric field after it has propagated through the atmosphere. This expression is expanded as (Kemball et al., 1995):

$$\begin{aligned}
\mathbf{G^p}.\mathbf{E} &= \frac{1}{\sqrt{1+D^{p*}D^p}} S^p e^{2\pi i\nu(t+\tau)+\gamma^p} \\
S^R &= E^R e^{-j\alpha(t)} + D^R E^L e^{j(\alpha(t)+\gamma^{L-R})} \\
S^L &= E^L e^{+j\alpha(t)} + D^L E^R e^{-j(\alpha(t)+\gamma^{R-L})}
\end{aligned} \tag{2.16}$$

Here E^R and E^L are the electric field strengths of the signal in right- and left-hand polarisations and τ incorporates all of the non-polarisation dependent delay caused by the atmosphere. The γ^p term is the total polarisation-dependent excess phase caused by the ionosphere and γ^{R-L} is equivalent to $\gamma^R - \gamma^L$. The (D^p, D^q) terms are complex numbers which reflect the degree of instrumental contamination from the orthogonal polarisation, they are usually assumed to be constant in time and frequency and independent of direction over sufficiently small fields of view. The α term represents the parallactic angle.

The parallactic angle is the angle between the elevation great circle of the antenna and the direction of north at the point being observed. The elevation great circle can be thought of as the cirle traced out by the antenna in elevation when its azimuth angle is set to that of the source. Explicitly it is given by:

$$\alpha(t) = \arctan\left[\frac{\cos\lambda_{lat}\sin H}{\sin\lambda_{lat}\cos\delta - \cos\lambda_{lat}\sin\delta}\right] \tag{2.17}$$

Here λ_{lat} is the antenna latitude and the (H, δ) are the apparent hour angle and declination of the source at the antenna respectively. The parallactic angle is important for altitude-azimuth antennas as these antennas rotate with respect to a given source direction as a function of time (Roberts et al., 1991) causing the parallactic angle to change over the course of the observation. Thus in these antennas the parallactic angle introduces a constantly varying phase term to the detected source radiation. As a result of the wide separa-

tion of the antennas in the VLBA the parallactic angle phase contribution will be different at each antenna.

After detection, the signals pass through independent receiver systems and electronics before being correlated. The use of independent receiver systems introduces differences between the two recorded polarisation modes for two reasons. Firstly the characteristic amplitude gain and bandpass response of the receiving systems will be different for each polarisation and thus independent determinations of these quantities must be made for each of the two polarisations (Kemball et al., 1995; Leppanen et al., 1995). Secondly differences in cable lengths, filters, receiving electronics and local oscillator phase offsets introduce delay and phase offsets between the polarisations and some calibration scheme must be undertaken to remove them (Cotton, 1993). The antenna electronics are sufficiently stable that the residual phase-delay rates are approximately zero between the two polarisations. It is useful to note at this stage that the standard phase calibration schemes will adjust these phase differences to the reference polarisation at the reference antenna (Roberts et al., 1991). This will allow an arbitrary phase and delay difference to remain between the two parallel hand systems. The phase difference converts directly into an arbitrary but constant rotation of the apparent electric field vectors on the sky.

The correlator performs a polarisation-independent delay correction before cross-correlating each pair of input antennas based signals to produce a time series of visibilities $r^{pq}_{mn}(u,v,\nu)$. The $p,q \in [RCP, LCP]$ denotes the polarisation state of the signal and the subscripts indicate the antenna number of the signal. These visibilities can be related to the source radiation via a Fourier transform relationship as noted earlier (Kemball et al., 1995):

$$r^{pq}_{mn} = (G^p_m G^{*q}_n)(B^p_m B^{*q}_n) \times \int\int_\Omega < S^p_m(l,m,\nu) S^{*q}_n(l,m,\nu) > e^{-j2\pi(lu+mv)} dl dm, \tag{2.18}$$

where $<>$ denotes the time averaging and $S^p_m(l,m,\nu)$ is proportional to the voltage response of the feed as given in equation 2.16.

The residual antenna gain factor for the nominal recorded polarisation

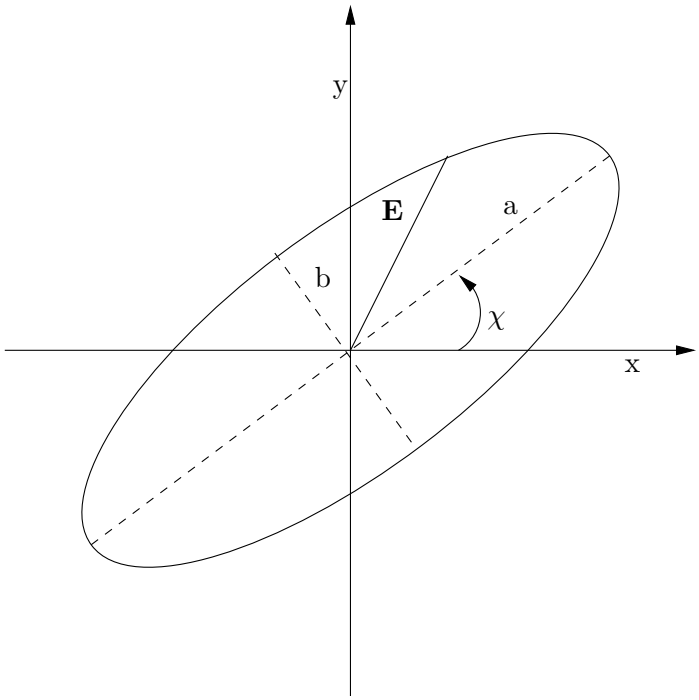

Figure 2.3: A schematic of elliptically polarised light.

p is denoted by $G^p(\nu,t) = g^p(t)e^{j\phi^p(\nu,t)}$ where the $g^p(t)$ term contains the receiver gain of the earlier chapter and also subsumes the $\frac{1}{\sqrt{1+D^{p*}D^q}} \simeq 1$ term. The phase term of the gain factor incorporates all the phase effects including the atmosphere and the receiving system. The remaining B^p term is the bandpass response for the polarisation p.

The polarisation and intensity of a beam of radiation can conveniently be described by a set of four quantities known as the Stokes parameters. The polarisation properties of an astrophysical source are thus commonly described by specifying the spatial distribution of these four parameters across the source.

The relationship between the Stokes parameters and the measured visibilities will be described later in this section and we include for the sake of completeness a brief introduction to the Stokes parameters and their physical meaning. The Stokes parameters can be used to describe any beam of partially polarised light. Such a beam of light can be resolved into two components: an unpolarised component of intensity I_u and an elliptically polarised component, intensity I_e.

The polarised component can be described by considering the diagram in

figure 2.3 (Shurcliff and Ballard, 1964). This diagram represents the ellipse traced out by the electric vector of the source radiation as it propagates towards us (i.e., out of the paper). The ellipse has semi-axes $a > b$ and its orientation angle χ is measured with respect to the $+x$ axis. It is useful to define another angle β such that $\tan(\beta) = \pm\frac{b}{a}$ where the plus sign indicates clockwise rotation and the minus sign indicates anticlockwise rotation of the electric vector. The angle β takes values between $-\frac{\pi}{4}$ and $+\frac{\pi}{4}$. The Stokes parameters can be described in terms of the above defined quantities as follows:

$$\begin{aligned} I =& I_e + I_u \\ Q =& I_e \cos 2\beta \cos 2\chi \\ U =& I_e \cos 2\beta \sin s\chi \\ V =& I_e \sin 2\beta \end{aligned} \tag{2.19}$$

Thus the Stokes parameter I describes the total intensity of the radiation and Q, U and V describe the polarised part of the radiation and $I_e = \sqrt{Q^2 + U^2 + V^2}$. The Stokes parameter V is equal to the intensity of the circularly polarised component of the radiation with the sign of V indicating the sense of rotation (Shurcliff and Ballard, 1964). Parameters Q and U describe the linearly polarised component of the radiation. The intensity and angle of the linearly polarised component of the radiation can be obtained by the following relationships :

$$\begin{aligned} I_l =& \sqrt{Q^2 + U^2} \\ \chi_l =& \frac{1}{2} \arctan(\frac{U}{Q}) \end{aligned} \tag{2.20}$$

Here I_l is the intensity of the linearly polarised component of the radiation and χ_l the electric vector angle of the same component.

The Stokes parameters $\{I, Q, U, V\}(l, m, \nu)$ of the incident radiation in the circularly polarised basis(E^R, E^L) can be related to the parallel and cross-

hand correlation pairs via the following equations (Conway and Kronberg 1969):

$$\begin{aligned}
< E^L E^{L*} > (l,m,\nu) &= LL = I(l,m,\nu) + \ V(l,m,\nu) \\
< E^R E^{R*} > (l,m,\nu) &= RR = I(l,m,\nu) - \ V(l,m,\nu) \\
< E^R E^{L*} > (l,m,\nu) &= RL = Q(l,m,\nu) + jU(l,m,\nu) \\
< E^L E^{R*} > (l,m,\nu) &= LR = Q(l,m,\nu) - jU(l,m,\nu)
\end{aligned} \tag{2.21}$$

The counterparts of the Stokes parameters in the visibility plane are (Kemball et al., 1995):

$$\begin{aligned}
I(l,m,\nu) \ \ \mathcal{F} \ \ \mathcal{I} &= \frac{1}{2}[\mathcal{RR}(u,v,\nu) + \mathcal{LL}(u,v,\nu)] \\
V(l,m,\nu) \ \ \mathcal{F} \ \ \mathcal{V} &= \frac{1}{2}[\mathcal{LL}(u,v,\nu) - \mathcal{RR}(u,v,\nu)] \\
Q(l,m,\nu) \ \ \mathcal{F} \ \ \mathcal{Q} &= \frac{1}{2}[\mathcal{RL}(u,v,\nu) + \mathcal{LR}(u,v,\nu)] \\
U(l,m,\nu) \ \ \mathcal{F} \ \ \mathcal{U} &= \frac{j}{2}[\mathcal{LR}(u,v,\nu) - \mathcal{RL}(u,v,\nu)]
\end{aligned} \tag{2.22}$$

where $\mathcal{F}$ denotes the Fourier transform operation and the spatial Fourier transform of the visibilities $\{RR, LL, RL, LR\}(l,m,\nu)$ are denoted by the terms $\{\mathcal{RR}, \mathcal{LL}, \mathcal{RL}, \mathcal{LR}\}(u,v,\nu)$. Using the expression for the S^p in equation 2.16 to expand $< S^p_m(l,m,\nu) S^{*q}_n(l,m,\nu) >$ yields the relationships denoted below (Kemball et al., 1995):

$$
\begin{aligned}
r_{mn}^{RR}(u,v,\nu) =& (G_m^R G_n^{R*})(B_m^R B_n^{R*})[(\mathcal{RR})e^{-j(\alpha_m-\alpha_n)} + (\mathcal{RL})D_n^{R*}e^{-j(\alpha_m+\alpha_n)}e^{j\gamma_n^{R-L}} \\
&+ (\mathcal{LR})D_m^R e^{j(\alpha_m+\alpha_n)}e^{j\gamma_m^{L-R}} + (\mathcal{LL})D_m^R D_n^{R*}e^{j(\alpha_m-\alpha_n)}e^{j(\gamma_m^{L-R}-\gamma_n^{L-R})}] \\
r_{mn}^{LL}(u,v,\nu) =& (G_m^L G_n^{L*})(B_m^L B_n^{L*})[(\mathcal{LL})e^{j(\alpha_m-\alpha_n)} + (\mathcal{LR})D_n^{L*}e^{j(\alpha_m+\alpha_n)}e^{j\gamma_n^{L-R}} \\
&+ (\mathcal{RL})D_m^L e^{-j(\alpha_m+\alpha_n)}e^{j\gamma_m^{R-L}} + (\mathcal{RR})D_m^L D_n^{L*}e^{-j(\alpha_m-\alpha_N)}e^{j(\gamma_m^{R-L}-\gamma_n^{R-L})}] \\
r_{mn}^{LR}(u,v,\nu) =& (G_m^L G_n^{R*})(B_m^L B_n^{R*})[(\mathcal{LR}e^{j(\alpha_m+\alpha_n)} + (\mathcal{LL})D_n^{R*}e^{j(\alpha_m-\alpha_n)}e^{j\gamma_n^{R-L}} \\
&+ (RR)D_m^L e^{-j(\alpha_m-\alpha_n)}e^{j\gamma_m^{R-L}} + (\mathcal{RL})D_m^L D_n^{R*}e^{-j(\alpha_m+\alpha_n)}e^{j(\gamma_m^{R-L}-\gamma_n^{L-R})}] \\
r_{mn}^{RL}(u,v,\nu) =& (G_m^R G_n^{L*})(B_m^R B_n^{L*})[(\mathcal{RL})e^{-j(\alpha_m+\alpha_n)} + (\mathcal{RR})D_n^{L*n}e^{-j(\alpha_m-\alpha_n)}e^{j\gamma_n^{L-R}} \\
&+ (\mathcal{LL})D_m^R e^{j(\alpha_m-\alpha_n)}e^{j\gamma_m^{L-R}} + (\mathcal{LR})D_m^R D_n^{L*}e^{j(\alpha_m+\alpha_n)}e^{j(\gamma_m^{L-R}-\gamma_n^{R-L})}]
\end{aligned}
\tag{2.23}
$$

Equations 2.23 give the relationship between the measured parallel and cross-hand visibilities which are corrupted by instrumental and atmospheric effects and the actual parallel and cross-hand correlation of the source emission. These equations can thus be used to remove as many corrupting effects from the data as possible before attempting to image the source.

2.8 Calibration

2.9 Bandpass calibration

In spectral line observations the observing bandwidth is divided into several baseband spectral windows, each sampled over a discrete number of frequency channels. These channels will not have exactly identical amplitude and phase response and the process of determining and compensating for the antenna gain as a function of frequency (or channel number) is referred to as bandpass calibration (Diamond, 1989). The bandpass response of the set of frequency channels can be determined by observing a continuum calibrator which has an expected flat amplitude spectrum and constant phase response over the spectral window (Formalont and Perley, 1989). The bandpass response can

be determined from the autocorrelation data of the calibrators alone, however in a narrow bandwidth the baseband filters may suffer from aliasing leading to differences in the autocorrelation and crosscorrelation bandpass amplitude response. In order to mitigate these considerations a full complex bandpass response must be determined from the cross-power spectra for the continuum calibrators (Kemball et al., 1995).

Before solving for the bandpass response, residual linear phase slopes in time and frequency must be determined using fringe fitting and removed from the data. The spectra are then averaged over time and an antenna-based simultaneous fit is performed for each channel which minimises:

$$Error = \sum_{m=1}^{N_a} \sum_{n=m+1}^{N_a} \sum_{l=1}^{N_c} ||r_{mn}^{pp}(\nu_l) - B_m^p(\nu_l) B_n^{p*}(\nu_l)||, \qquad (2.24)$$

where N_a is the number of antennas and N_c is the number of frequency channels, $r_{mn}^{pp}(\nu_l)$ is the time averaged parallel-hand calibrator cross-power spectrum at frequency (ν_l) for the baseline $(m-n)$. The $B_m^p(\nu_l)$ is the complex bandpass response at antenna m for polarisation p as a function of frequency.

The bandpasses are determined independently in each hand of circular polarisation using the parallel-hand data (Kemball et al., 1995). Since the cross-power spectra contain only the difference of the phase of the bandpass response of each antenna the system of equations are undetermined by an additive constant. A reference antenna is thus chosen and the bandpass phase response is set to zero at this antenna; the phase responses solved for all the other antennas are then the difference between their bandpass response and the bandpass response of the reference antenna. It is preferable that this reference antenna be the same reference antenna that was used during the fringe fitting process. The removal of phase slopes in time and frequency before bandpass determination means that the bandpass phase response will not have a net group delay, if there was such a group delay in the bandpass response then a time-variable group delay offset could be introduced between the two polarisations (Kemball et al., 1995).

The cross-power data are corrected in the form:

$$r_{mn}^{pq'} = \frac{r_{mn}^{pq}(\nu)}{B_m^p(\nu)B^{q*}n(\nu)} \tag{2.25}$$

The autocorrelation bandpass response $A_m^p(\nu)$ is determined by directly averaging the autocorrelation spectra of the calibrator sources in time, and the autocorrelation data are corrected as (Diamond, 1989):

$$r_m^{pp'} = \frac{r_m^{pp}(\nu) - A_m^p(\nu)}{A_m^p(\nu)} \tag{2.26}$$

2.10 Doppler shift correction

As mentioned in section 2.2 the correlator model places the correlated spectra in a certain reference frame. For the VLBA, this is a geocentric reference frame. The relative motion of this reference frame with respect to the motion of the source induces a time-variable Doppler shift in the spectrum. The LO at each antenna generally do no track the residual Doppler effect in real time as it is too complicated logistically. Instead a fixed correction at the midpoint of the run is used and thus a residual time-variable offset remains in the correlated data. This effect is typically of the order of a few kilometers per second.

The Doppler effect can be corrected using the shift theorem of Fourier transforms. The procedure is to Fourier transform the spectrum to delay space and then multiply the delay function by $e^{i2\pi\Delta\nu\tau}$ where $\Delta\nu$ is the desired frequency shift and then transform back to frequency space (Reid et al., 1980).

Using the radio definition for Doppler shift, the spectrum needs to be shifted by:

$$\Delta\nu = \nu_{obs} - \nu_0(1 - \frac{V_{tot}(t)}{c}), \tag{2.27}$$

where ν_{obs} is the observed frequency, ν_0 is the line rest frequency, c is the speed of light and V_{tot} is the total velocity of the reference frame with respect to the local standard of rest (Thompson et al., 2001).

2.11 Amplitude calibration

The recorded crosscorrelation co-efficients r^{pq}_{mn} can be expressed in units of correlated flux density by multiplying by the geometric mean of the power in each recorded signal (Reid, 1995):

$$J^{pq}_{mn}(\nu) = b\sqrt{P^p_m(T^p_a m + T^p_{sm})P^p_n(T^q_{an} + T^q_{sn})}\ \ r^{pq}_{mn}(\nu) \tag{2.28}$$

In this expression, $J^{pq}_{mn}(\nu)$ represents the amplitude calibrated cross-power spectrum, T^p_{am} is the averaged antenna temperature across the band due to the source emission at antenna m and T^p_{sm} is the off-source system temperature; the sum of these two quantities gives the system temperature during the observations. The P^p_m term is the point source sensitivity of the antenna in Jansky per Kelvin. The point source sensitivity of an antenna is inversely proportional to its effective aperture. As effective aperture varies with elevation and the antenna elevations will change with time the gain correction is time-dependent (Moran and Dhawan, 1995). The dependence of the aperture efficiency on elevation is due primarily to the deforming effect gravity has on the reflector surface. As the antenna changes elevation the position of the focus of the antenna will alter and thus will no longer co-incide with the position of the antenna subreflector the overall effect of which is a reduction of effective collecting area (Moran and Dhawan, 1995).

The system temperatures at all of the antennas are recorded throughout the observations usually using switched noise source calibration. The point source sensitivities are monitored independently over longer time scales (Walker, 1989). The b term is the factor that accounts for digitisation losses etc and is dependent on the encoding system and on details of the correlator. In this system it is possible to factorise the correction term into the antenna amplitude gain factors:

$$\frac{1}{g^p_m(t)} = b^{\frac{1}{2}}\sqrt{P^p_m(T^p_{am} + T^p_{sm})} \tag{2.29}$$

This method of calibration is employed in continuum observations. In the case of high-SNR spectral line observations a more accurate method of cali-

bration can be used. The template-fitting calibration procedure uses the autocorrelation spectrum of a single well-determined reference scan (Reid et al., 1980). The bandpass autocorrelation data are related to the calibrated total power spectrum by:

$$r_m^{pp}(\nu) = \frac{1}{P_m^p(T_{am}^p + T_{sm}^p)} J^{pp}(\nu) - \frac{T_{am}^p}{(T_{am}^p + T_{sm}^p)} + \epsilon_m(\nu), \tag{2.30}$$

where the final $\epsilon_m(\nu)$ is the residual instrumental baseline after bandpass correction (Walker, 1977). This differs from the correction for the cross-hand spectra because the autocorrelation process includes correlated self-noise. Since each antenna observes the same total power spectrum it is reasonable to assume that the corrected autocorrelation spectrum shape should stay the same throughout the observation. Exploiting this assumption, the $g_m^p(t)$ amplitude gain correction factors can be determined by performing the following least-squares minimisation:

$$Error = \sum_{\nu=\nu_1}^{\nu_2} [r_m^{pp}(\nu) - (g_m^p)^2 J^{pp}(\nu) + \sum_{k=0}^{n_{poly}} a_k \nu^k]^2 \tag{2.31}$$

The J^{pp} here represents the reference template spectrum which has been calibrated according to the relationship in equation 2.30. This scan should be chosen as one which has a high signal-to-noise ratio and is preferably at high elevation. The polynomial term at the end is included to account for the effect of imperfect bandpass removal and includes the offset term $a_0 = -\frac{T_{am}^p}{T_{am}^p + T_{sm}^p}$.

This method is less sensitive to individual measurements of system temperatures recorded throughout the run; its accuracy is limited by the systematic accuracy of the system temperature measurements taken during the reference scan.

The gain curves are determined separately for each hand of polarisation by fitting the parallel hand data to the parallel hand spectrum of the template spectrum from the reference scan. These template scans are independent and the amplitude calibration is thus vulnerable to amplitude offsets between the

two polarisations which may be introduced by systematic errors in the measured calibration parameters for each of these scans (Kemball, 1999). An offset in the amplitudes of the two polarisations at the reference scan will translate into an amplitude offset between the two polarisations throughout the observing run. Such an effect must be determined and corrected. Assuming that the source has nearly zero net circular polarisation it is possible to determine the amplitude offset term in a fit to direct ratios of the RR and LL data (Kemball, 1999).

2.12 Phase calibration

Instrumental and propagation effects at each antenna result in an instrumental phase contribution to the final recorded visibilities. This instrumental phase is approximated over short time intervals by linear slopes in time and frequency; these slopes are defined by the residual phase-delay rate $\dot{\theta_m^p}$ and the residual group delays, τ_m^p, plus a residual phase offset $\theta(\nu_0, t_0)$. These solutions are expressed relative to a reference antenna which is set to have an instrumental phase of zero. The solutions thus take the form:

$$\phi_m^p(\nu, t) = (\nu - \nu_0)(\tau_m^p - \tau_0^p) + (\dot{\theta_m^p} - \dot{\theta_0^p})(t - t_0) + (\theta_m^p - \theta_0^p), \qquad (2.32)$$

where ν_0 is the band-edge frequency, t_0 is the reference time of the solution interval and the terms with subscript zero refer to the delay, fringe rate and phase offset of the reference antenna (Walker, 1989). The residual phase is initially set to the values, $\theta_m^R = -\alpha_m; \theta_m^L = +\alpha_m$, as a first order correction for the parallactic angle terms in the equation 2.23 (Kemball et al., 1995).

2.13 Fringe fitting

The residual delays and fringe rates are estimated via a process known as fringe fitting. A discussion of global fringe fitting techniques can be found in Schwab and Cotton (1983). Global techniques derive their name from their fit for all of the antenna-dependent delays,rates and residual phase offsets in

a simultaneous solution. The global fringe search is implemented by way of a least-squares minimisation procedure. This procedure requires a reasonably good initial guess of the delays and rates as an input. This can be obtained by Fourier transforming the data to the delay-time domain in order to perform an initial baseline-based search for the group-delay and phase-delay rate.

The least-squares minimisation fringe search used by Schwab and Cotton (1983) minimised the expression:

$$\chi^2 = \sum_{k,l} \sum_{i<j} w_{ijkl} \times |e^{i[\tilde{\theta_{ij}}(t_k,\nu_l)-\theta_{ij}]} - e^{i[(\theta_i-\theta_j)+(\dot{\theta_i}-\dot{\theta_j})(t_k-t_0)+(\tau_i-\tau_j)(\nu_l-\nu_0)]}|^2 \tag{2.33}$$

The $\tilde{\theta_{ij}}$ are the measured phases of the visibilities and θ_{ij} are the phases of the initial source model.

Global fringe fitting techniques are advantageous because the delays and rates can be determined in antenna-based form from the parallel hand data and then applied to the cross-hand polarised correlations. This means that the fringes do not have to be directly detected in the cross-hand data.

It is difficult to determine the residual delays from the spectral source since the structure phase of the source changes with frequency. Thus independent residual delays are found in each polarisation by fringe fitting a continuum calibrator (Cotton, 1993). The delays found by this procedure $\tau_m^R - \tau_0^R$ and $\tau_m^L - \tau_0^L$ are constrained to have the same reference antenna but not the same reference antenna polarisation. Since the right- and left-hand systems involve substantially different electronics and cabling there may be a delay difference between these two systems. This delay offset can be determined from the baseline-based cross-hand delays τ_{mn}^{RL} and τ_{mn}^{LR} using relations of the general form:

$$\begin{aligned}
\delta\tau_m^{R-L} &= \tau_{mn}^{RL} - \tau_{mn}^{LL} \\
\delta\tau_m^{R-L} &= \tau_{mn}^{RR} - \tau_{mn}^{LR} \\
\delta\tau_n^{R-L} &= \tau_{mn}^{RL} - \tau_{mn}^{RR} \\
\delta\tau_n^{R-L} &= \tau_{mn}^{LL} - \tau_{mn}^{LR}
\end{aligned} \tag{2.34}$$

The cross-hand delays can be directly estimated from the phase slopes of the cross-power spectra of the continuum calibrators as they satisfy the relations $\tau_{mn}^{RL} = \frac{1}{2\pi}\frac{\partial\theta_{mn}^{RL}}{\partial\nu}$ and $\tau_{mn}^{LR} = \frac{1}{2\pi}\frac{\partial\theta_{mn}^{LR}}{\partial\nu}$ (Brown et al., 1989).

The delay offset is expected to be stable for the duration of a typical observation and can thus be determined from a single scan to the reference antenna (Brown et al., 1989). The cross-hand delay in the continuum calibrators can be taken to be of instrumental origin as these sources are essentially circularly unpolarised. The delay corrections for the two polarisations are then adjusted to remove the delay offset between them by adding the determined delay difference δ_m^{R-L} to the delay solutions for left-hand parallel correlations.

After finding the delay solution, estimates of the residual fringe rate and phase offsets $(\theta_m^p, \dot{\theta_m^p})$ are determined by fringe-fitting the source data in a spectral reference channel (Reid et al., 1980). The reference channel is selected to have adequate signal to noise ratio and a compact structure. The fringe rate and phase solution is only weakly-dependent on frequency and the solutions determined from the reference channel can be applied to all the other channels in the observing bandpass (Reid et al., 1980). These initial estimates are accurate enough to allow the visibilities to be coherently averaged in time. The quality of the fringe fit is affected by errors in the initial source model which are manifested as inaccuracies in the estimate of the residual phase offset and so these values are more accurately determined at a later stage by self-calibration techniques (Thompson et al., 2001).

The parallel hand data is used to determine the residual fringe rates and phase offsets but in order to retain positional coincidence of the right- and left-hand phase data the solutions cannot be determined independently in each hand of polarisation. Instead of determining independent solutions the solution is determined for the reference channel in the reference polarisation and then this solution is applied to the complementary polarisation after correcting for polarisation offset terms $(\dot{\delta\theta_m^{R-L}}, \delta\theta_m^{R-l})$ (Kemball et al., 1995). If LCP is used as the reference polarisation then the total phase solution is

constructed as:

$$\begin{aligned}\phi_m^L(\nu,t) =&(\tau_m^L - \tau_0^L)(\nu-\nu_0) + (\dot{\theta}_m^L - \dot{\theta}_0^L)(t-t_0) + (\theta_m^L - \theta_0^L)\\ \phi_m^R(\nu,t) =&(\tau_m^R - \tau_0^R + \delta\tau_0^{R-L})(\nu-\nu_0) + (\dot{\theta}_m^L - \dot{\theta}_0^L + \delta\dot{\theta}_m^{R-L})(t-t_0)+\\ &(\theta_m^L - \theta_0^L + \delta\theta_m^{R-L})\end{aligned} \tag{2.35}$$

,where:

$$\begin{aligned}\delta\tau_m^{R-L} =&\tau_m^R - \tau_m^R\\ \delta\dot{\phi}_m^{R-L} =&\dot{\phi}_m^R - \dot{\phi}_m^L\\ \delta\phi_m^{R-L} =&\phi_m^R - \phi_m^L\end{aligned} \tag{2.36}$$

The antenna electronics should be sufficiently stable that the fringe-rate offset term is negligibly small. The phase offset is determined using the parallel-hand cross-power phases by solving the system of equations (Kemball et al., 1995):

$$\Phi_{mn}^{RR} - \Phi_{mn}^{LL} = \delta\theta_n^{R-L} - \delta\theta_m^{R-L}, m \in 1..N_a, n \in m+1,..N_a \tag{2.37}$$

Since this system of equations is underdetermined it is only possible to solve for $\delta\theta_m^{R-L} + constant$ which leaves the RCP and LCP system offset by an unknown constant of phase. This implies that the observed angle of the linearly polarised emission is rotated by an unknown angle from its absolute position, as noted above.

2.14 Self-calibration

The final phase offsets and fringe rates are estimated using self-calibration. Self calibration is an iterative procedure which simultaneously solves for the source intensity distribution and the complex antenna gains (Cornwell and Fomalont, 1989). There are a number of schemes for implementing self-calibration and a review of these techniques is given by Pearson and Readhead (1984). Most of these methods have a similar form involving alternating

calibration and imaging steps between the image- and the visibility-plane with adjustments and constraints in each domain.

An initial estimate of the source structure is Fourier transformed to obtain a set of trial visibilities $\tilde{r_{ij}}(u_k, v_k)$, then a least-squares minimisation is performed to obtain the complex antenna gains $g_m(t_k)\ g_n^*(t_k)$:

$$\sum_k \sum_{m=1}^{N_a} \sum_{n=m+1}^{N_a} [r_{mn}(u_k, v_k, \nu_r) - g_m(t_k) g *_n (t_k) \tilde{r_{mn}}(u_k, v_k)]^2 \qquad (2.38)$$

In this expression the $r_{ij}(u_k, v_k)$ are the measured visibilities and $\tilde{r_{mn}}(u_k, v_k)$ are the trial visibilities determined from the the initial estimate of the source structure (frequently a point source estimate is used). Often the amplitude gains are corrected *a priori* and held fixed, and only the antenna phase gain is regarded as a free parameter.

The original self-calibration procedures made explicit use of closure phases to obtain a set of trial visibilities. A closure phase is the sum of the observed phases around a closed triangle, this sum contains no instrumental and propagation effects as the total contribution of these effects cancel when summed over a closed triangle. One of the most popular self-calibration procedure of this type was the one proposed by Readhead and Wilkinson (1978). In their method a model was used to provide estimates of the visibilities on two of the baselines for all independent closure phases. The phase on the third baseline was derived from the measured closure phase. This was used to make corrections to the phases on individual baselines. The process of solving for antenna based gains as in equation 2.38 is fully equivalent to the phase closure technique and leads to a naturally concise formulation of the problem (Cornwell and Wilkinson, 1981).

The phases derived from the least-squares procedure are combined with the observed amplitudes and Fourier transformed to the image domain. The output of a non-linear deconvolution algorithm such as CLEAN on this image is then adopted as an improved model of the source structure. The CLEAN algorithm is used to compensate for the effect of poor sampling in the (u, v)-plane (see equation 2.13)and can also be used to impose reasonable physical

constraints such as positivity and compactness in the final source model. The action of CLEAN is discussed more thoroughly in a later section. The source model from CLEAN is transformed to the visibility domain and used in the least-squares procedure to obtain a second estimate of the antenna phase gains. This procedure continues iteratively until a satisfactory solution for the antenna complex gains and source brightness distribution has been obtained (Thompson et al., 2001).

2.15 Imaging

As described in section 2.6 the image formed by taking the Fourier transform of the calibrated, sampled visibilities is the convolution of the sky brightness distribution and the dirty beam. In order to produce a high quality image of the source these two function must be deconvolved. However it is clear that the solution to this convolution equation is non-unique as any finite visibility distribution can be assigned to the unsampled points in the u, v plane and the corresponding intensity distribution, labelled the 'invisible distribution', will still be consistent with the measured visibilities (Cornwell and Braun, 1989). Significant constraints can be placed on this problem by making use of *a priori* information about the source such as its probable limited spatial extent.

Thus the predominant method of producing plausible source images is via non-linear deconvolution algorithms which place reasonable constraints on the invisible distribution. The 'CLEAN' algorithm, devised by Högbom (1974), is a popular choice. The action of the 'CLEAN' algorithm is described by Cornwell and Braun (1989) as follows:

1. Compute the dirty image and dirty beam. Then find the intensity and position of the brightest point in the map.

2. Subtract over the whole image a dirty beam pattern which is centred on the position of the brightest point in the image. The subtracted dirty beam is multiplied by the source strength at the brightest point and a damping factor γ termed the *loop gain*.

3. Go to step 1, each time replacing the dirty image with the residual map from the previous iteration. Stop when any remaining peaks in the map are below some user specified level

4. Convolve all the components removed in step 2 with an idealised 'CLEAN' beam (usually an elliptical Gaussian fitted to the central lobe of the dirty beam) and return them to the final residual map.

2.16 Feed calibration

The problem of orthogonal feed contamination is discussed in section 2.7. In the case of nearly perfect feeds and weakly polarised emission the system of equations 2.23 can easily be linearised by neglecting second-order terms, $D_m D_n$, and terms involving the product of D and polarised emission such as $(\mathcal{Q} + j\mathcal{U})D_m$ (Cotton, 1993). After applying the amplitude and phase corrections discussed in the preceding sections the system of equations reduces to:

$$\begin{aligned}
r'^{RR}_{mn}(u,v,\nu) &= \mathcal{RR} \\
r'^{LL}_{mn}(u,v,\nu) &= \mathcal{LL} \\
r'^{RL}_{mn}(u,v,\nu) &= \mathcal{RL} + D^{L*}_n(\mathcal{RR})c^{j2\alpha_n}e^{-j\gamma^{R-L}_n} + D^{R}_m(\mathcal{LL})e^{j2\alpha_m}e^{-j\gamma^{R-L}_m} \\
r'^{LR}_{mn}(u,v,\nu) &= \mathcal{LR} + D^{L}_m(\mathcal{RR})e^{-j2\alpha_m}e^{j\gamma^{R-L}_m} + D^{R*}_n(\mathcal{LL})e^{-j2\alpha_n}e^{j\gamma^{R-L}_n},
\end{aligned} \tag{2.39}$$

where r'^{pq}_{mn} are the corrected cross-power spectra. After considering the above equations in combinations with the equations 2.22 it is clear that the stokes I and V image can be obtained directly from the calibrated parallel hand data , however the cross-hand data must have the effect of feed contamination removed before successful imaging of the stokes U and Q parameters can take place. The last two equations in the above expression are linear in D^{L*}_m and D^{R}_m and can thus be solved for using complex linear least-squares techniques if the polarisation of the source structure is well-determined. Thus the process of feed calibration uses a parametrised representation of the polarisation

structure of a calibrator source together with the observed visibilities of the source in a composite least-squares procedure to simultaneously solve for the polarisation structure and the D-terms (Kemball, 1999).

There is some flexibility in the choice of calibrator and the subsequent assumptions which are made about its polarisation structure. One may use a continuum source which is approximately linearly unpolarised so that $(\mathcal{Q},\mathcal{U}) = 0$ (e.g., Brown et al. (1989)), or one which is unresolved so that $(\mathcal{Q},\mathcal{U}) = constant$. As these two cases are relatively rare in VLBI observations Cotton (1993) suggested a method referred to as the similarity approximation where the linear polarisation structure of the source is assumed to be a scaled version of the total intensity structure ie $(\mathcal{Q} + j\mathcal{U}) = \beta\mathcal{I}$. This method works well with a moderately resolved continuum calibrator source. In spectral line observations Kemball et al. (1995) uses each spectral channel in the source observations as an independent polarisation calibrator. Thus for each channel the source polarisation structure is parametrised as $(\mathcal{Q}(\nu)+j\mathcal{U}(\nu)) = \beta\mathcal{I}(\nu)$. As each channel is likely to have independent structure this method reduces the likelihood of systematic errors in the estimation of the D-terms.

Once the D-terms are corrected, the Stokes Q and U images can be made using standard image deconvolution techniques. All that remains is to remove the arbitrary phase offset which originates from the phase difference between the right- and left-hand polarisation systems at the reference antenna. This can easily be achieved by observing a calibrator source with known electric vector position angle. The difference between the known polarisation angle and the observed angle is the required offset and subsequently the linear polarisation angle of the source is rotated by this amount (Cotton, 1993).

Chapter 3

Data reduction

3.1 Introduction

The 1612 MHz OH maser emission from the circumstellar envelope of OH 0.9+1.3 was observed using the VLBA. As highlighted in the previous chapter the recorded visibilities obtained from such an observation must undergo a series of calibration procedures before a reliable image of the source can be obtained. This chapter describes the data reduction process undertaken to calibrate and image the observations of OH 0.9+1.3.

The data was calibrated within NRAO's Astronomical Image Processing System (AIPS). In AIPS, calibration steps are performed by independent applications, called tasks, which are launched from the main program. The results of these calibration tasks are stored in a calibration table attached to the main uv-data file. These tables can be manipulated in various ways in order to improve the overall calibration. They can be smoothed, extrapolated, interpolated and merged with other calibration tables. At each calibration stage a new table is created which incorporates all the accumulated calibration information determined thus far (Diamond, 1995). This system is advantageous because the actual visibilities remain unaltered until one is satisfied that the best possible calibration file has been obtained. This final calibration file is then explicitly applied to the visibilities prior to imaging.

3.2 Observations

The source was observed on the 24th and 25th of October 1994. The total observing run lasted 11.9 hours and included interleaved observations of the continuum calibrators 3C84, 3C273 and J1613+3412. The observations of the continuum calibrators were included for the purpose of group-delay, bandpass and polarisation calibration. These observations were done in spectral line mode and the data was recorded in dual circular polarisation in two overlapping spectral windows of 250 kHz each. These two windows have leading edge frequencies of 1612.5 and 1612.68 MHz. Two bit sampling was used in the recording. These spectral windows will be referred to as spectral window 1 and 2 respectively throughout the rest of the chapter.

The spectrum of OH 0.9+1.3 consists of a set of strong blue-shifted spectral peaks and weaker red-shifted emission. The frequency range of the two observing bandwidths is such that they each encompass one of these emission features. The calibrator J1613+3412 was also observed in a wider frequency bandwidth of 1000 MHz

The data was recorded in VLBA format and correlated in Socorro, New Mexico. The correlator accumulation time was 9.4 seconds and the spectra were generated with a sampling of 128 frequency channels over each of the bandwidths. This provides a nominal channel separation of approximately 0.36 km.s^{-1}. The observing bands for the blue- and red-shifted lines were respectively centred at -120.0 km.s^{-1} and -87.5 km.s^{-1} with reference to the local standard of rest (LSR).

3.3 Data loading

The data was loaded into AIPS via the task FITLD. The correlator introduces digital signal processing effects which were corrected for by FITLD during the data loading process. This task can also be used to exclude all data with playback weights below a certain threshhold. The weight depends on the number of valid bits correlated in each integration interval and is an indication of the data quality. The data weights are normalised to unity so

that good data normally have weights close to 1. Data with weights below 0.8 were excluded at this stage of the reduction.

3.4 Parallactic angle

The parallactic angle α_m is defined in section 2.7 of the previous chapter. As outlined previously the rotation of the altitude-azimuth antennas over the course of an observation results in the introduction of constantly varying phase terms, equal to the instantaneous parallactic angle, to the observed source radiation. The large separation of the antennas of the VLBA means that the parallactic angles will be different for each observing station. Thus, if left uncorrected, they will introduce time variable phase offsets in the recorded visibilities. The phase contribution of constantly changing parallactic angle to the polarisation correlation pairs is shown in equation 2.23. Thus at the outset of the calibration process the phase-delays of the calibration table were set to $\theta_m^R = -\alpha_m; \theta_m^L = +\alpha_m$. This effect is calculated analytically for all antennas including the reference antenna. If uncorrected, terms of the form $e^{j(\alpha_m - \alpha_0)}$ are carried forward in the analysis and complicate the smoothing of the calibration tables (Kemball et al., 1995). The calculated parallactic angles at the antenna Brewster are given in figure 3.1.

3.5 Flagging

Before proceeding to calibration, several rounds of flagging were applied to the data. Flagging is the process of discarding discrepant or severely corrupted data points which arise as a result of array malfunctions or poor observing conditions; retaining these data will compromise imaging performance (Formalont and Perley, 1989).

The first set of flags applied to the data were those flags obtained from the on-line antenna monitoring systems. The on-line monitoring systems perform a set of internal checks designed to determine whether the data being collected are of good quality. These on-line flags were supplied in an

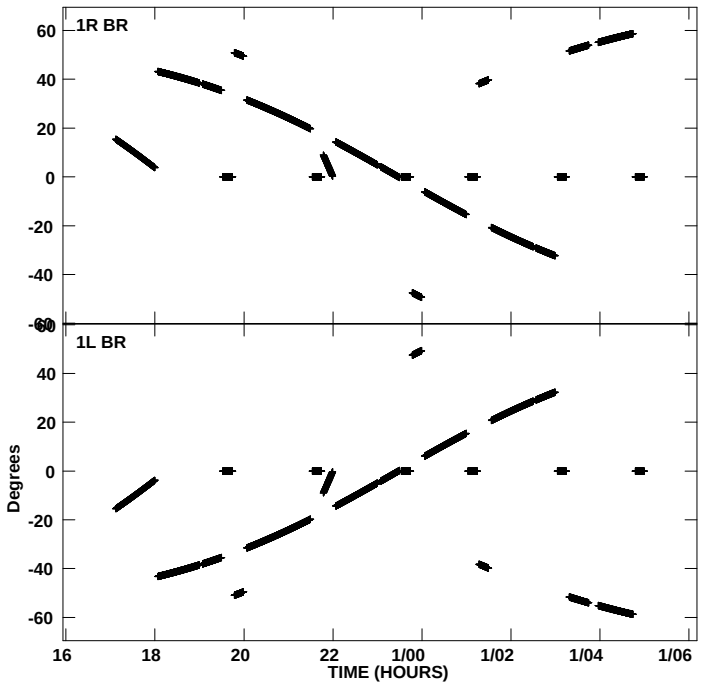

Figure 3.1: The variation of parallactic angle over the course of the observation at Brewster.

ancillary text file which was read in and applied to the data using the task UVFLG. The antenna operator logs were also examined to determine if there was any other bad data that needed to be flagged. The operator noted a brief electronics fault at Pie Town at 0d 17h 11m UT and this time period was flagged.

Data from antennas at elevations below 5 degrees was flagged using the task UVFLG. This flagging was necessary because at lower elevations there will be a large atmospheric contribution to the recorded system temperature. The system temperature consists of the receiver temperature plus an atmospheric contribution which increases at lower elevations and is given by the expression below:

$$T_{sys} = T_R + T_0(1 - e^{-\tau_0 \sec z}) \tag{3.1}$$

Here T_R is the receiver temperature, z the zenith angle, τ_0 is the atmospheric opacity at zenith and T_0 is the atmospheric temperature contribution at zenith.

Finally the data was flagged by weight. The appropriate weight threshold was determined by examining the data weights with a plot task called VPLOT. The plot of data weight versus time is shown in figure 3.2 and it is clear that the majority of good data points have weights above 0.15310. Thus this value was used as the cutoff threshold.

3.6 Calibrator autocorrelation data

3.6.1 Autocorrelation bandpass

The antenna-based autocorrelation bandpass responses, $B_m^R(\nu), B_m^L(\nu)$, were determined from the autocorrelation spectra of the continuum calibrators. The continuum calibrators are expected to have a flat amplitude response across the bandpass; any frequency dependent amplitude variations in their spectra can be attributed to the bandpass response. The continuum data underwent further editing prior to the bandpass determination. It was interactively flagged using a task (IBLED) which plots the visibility amplitude

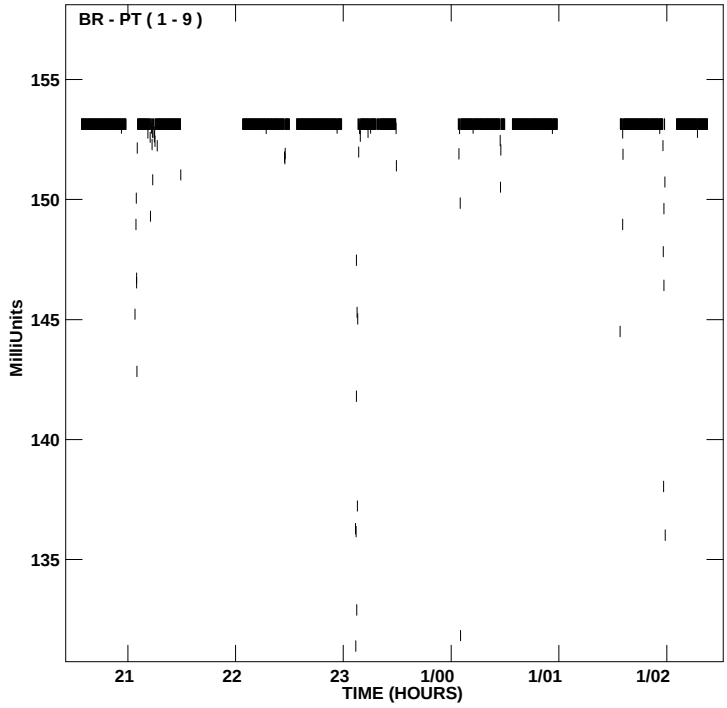

Figure 3.2: Data weight vs time on the Brewster to Pie Town baseline.

versus time graphically. Using this task, outliers were easily identified and subsequently flagged.

The bandpasses were determined with the task CPASS. This task uses a least-squares algorithm to fit a complex polynomial to a time-averaged continuum calibrator spectrum as indicated in equation 2.24 of the previous chapter. As the bandpass response is expected to be fairly stable over the course of an observation it was sufficient to determine a single bandpass response per antenna in each hand of polarisation. This bandpass would be valid for the whole course of the observation. In order to obtain the best possible estimate of the total bandpass response the continuum autocorrelation spectra were averaged in time over the whole observation before attempting to fit a polynomial response over frequency. These bandpasses were examined using a plotting task and found to have satisfactory profiles with the characteristic steep roll-off and flat passband expected of a bandpass response profile. This procedure was followed for both the observing bandwidths and

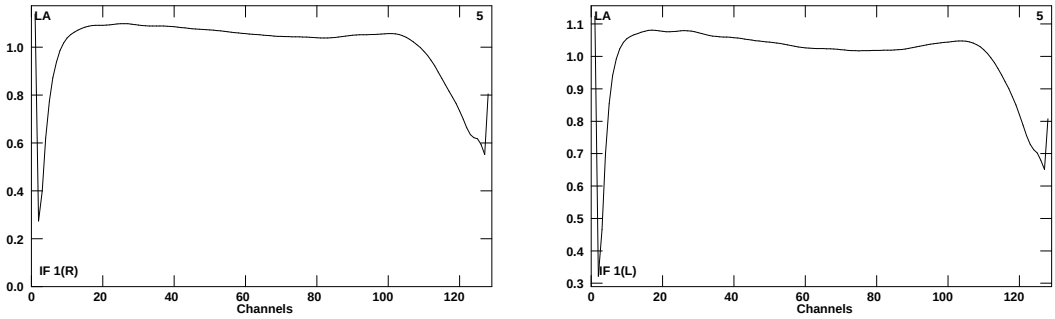

(a) Right-circular bandpass response (b) Left-circular bandpass response

Figure 3.3: The bandpass responses of the right- and left-circular receiving systems at Los Alamos.

figure 3.3 illustrates the autocorrelation bandpass response of LA.

3.6.2 Digital sampler bias corrections

In multi-level quantisation schemes of digital sampling (2-bit or more), amplitude offsets may arise between the two recorded polarisations if they are systematically assigned different sets of samplers. This is because higher quantisation samplers introduce amplitude offsets if the threshold voltage levels deviate from their nominal values and the threshold voltages of the different samplers will drift independently of one another (Kogan, 1995). This situation may arise in the VLBA correlator where amplitude offsets for 2-bit quantisation are typically of the order of 5-10%. The amplitude errors introduced by this effect were estimated from the autocorrelation spectra using a task ACCOR. The theory of this correction is discussed by Kogan (1995). This effect was estimated independently for both the calibrators and the source using their autocorrelation spectra.

3.7 OH 0.9+1.3 autocorrelation data

3.7.1 Doppler shifting

The motion of the correlator reference frame with respect to the observed source induces a residual time-variable Doppler shift in the source spectra as discussed in section 2.10. This effect can be corrected by calculating the required frequency shifts and applying them via the Fourier shift transform theorem. This effect was corrected in the source auto- and crosscorrelation spectra using the task CVEL. The 1612 MHz OH maser line has a rest-frequency of 1612.231 MHz and the spectra were corrected to have a central velocity of -120 and -87.5 km.s^{-1} in the blue- and red-shifted emission respectively, as used during observing. These Doppler shifts were also applied to the source crosscorrelation data.

3.7.2 Amplitude calibration

The antenna-based amplitude gains of the blue-shifted spectral window were determined using the template fitting method devised by Reid et al. (1980). This calibration procedure uses the calibrated total power spectrum of a single well-determined template scan and fits this template spectrum to all other total power spectra as indicated in equation 2.31. The required template spectrum should be chosen from a reliable antenna at a high elevation and should have a good signal to noise ratio. After examining a number of spectra the scan from Los Alamos from 0d 22h03 to 0d 22h30 UT was adopted as a suitable candidate. The left and right parallel-hand autocorrelation spectra of this scan were calibrated to units of jansky according to equation 2.30. The point source sensitivity of the VLBA antennas display a negligible variation with elevation at 18 cm wavelengths and the template scan was calibrated by adopting a single elevation-independent point source sensitivity, P_{LA} throughout the scan. The relevant point source sensitivities and system temperatures used in the calibration of the template scan are given in table 3.1.

This template fitting procedure was applied in AIPS using the task AC-

	T_{sys} (JY)	P_{LA} (JY/K)
RCP	41.5	10.42
LCP	49.25	7.75

Table 3.1: System Temperatures and Point Source Sensitivities for Los Alamos 0d 22h03 - 0d 22h30 UT.

FIT after applying corrections for the bandpass, residual Doppler shifts and sampler biases. In this procedure left- and right-circular gains are determined independently by fitting all the left-circularly polarised spectra to the left-circularly polarised spectrum of the template scan and similarly for the right-circularly polarised spectra. Thus, as discussed previously, an amplitude offset between the *a priori* calibration of the two parallel hand spectra at the reference scan will result in an amplitude offset in all the calibrated auto- and crosscorrelation spectra. This offset was determined by fitting the left-circular spectrum of the template scan to the right-circular spectrum using ACFIT. This task calculated a direct ratio of 0.935 between the two scans.

The red-shifted spectral window contained significantly weaker emission than the blue-shifted spectral window and very few of the recorded spectra had visible spectral structure. The ACFIT task fits a complex polynomial to the baseline of the spectral emission in each spectra and then scales the input spectrum to that of the template spectrum. This procedure has limited success if, as in the case of the red-shifted emission, the spectrum is almost completely flat. In this case the procedure will be unable to separate an appropriate spectral feature which is sufficiently orthogonal to the baseline polynomial. Thus ACFIT was unsuccessful in determining the appropriate antenna gains for the spectra of the red-shifted emission and instead these were calibrated using equations 2.30 and 2.28. The recorded system temperatures for the whole observation and the antenna point source sensitivities were supplied in an ancillary text file which was read into AIPS using the task APCAL. This method is less accurate than the template fitting method as it is limited by the inherent accuracy of the *a priori* calibration (5%).

The antenna gains for both observing bandwidths were examined and any outliers in the tables were removed.

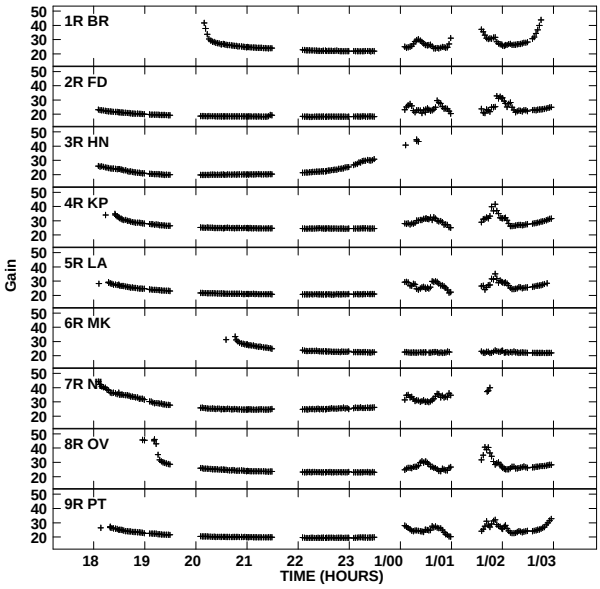

(a) Spectral window 1

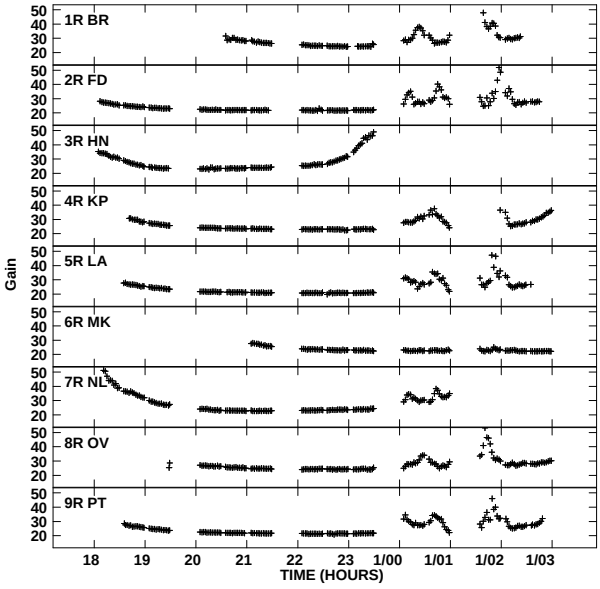

(b) Spectral window 2

Figure 3.4: The antenna-based amplitude gain factors in spectral windows 1 and 2.

3.8 Calibrator crosscorrelation data

The primary calibration purpose served by these data is to determine the crosscorrelation bandpass function, the antenna based group-delays and the difference between the right- and left-circularly polarised group-delays at the reference antenna. The amplitude of these spectra were calibrated by the traditional method of multiplying by the geometric mean of the power in the two correlated signals (Walker, 1989). After amplitude calibration, an initial fringe fit of the calibrator data was performed. This fringe fitting procedure, executed by the task FRING, estimated the residual group-delays, phase-delays and fringe rates. The quantities can only be determined with respect to a reference antenna. In this case the reference antenna was chosen to be Los Alamos and the phase response of this antenna was fixed at zero.

This initial fringe fit was used to remove residual phase slopes in time and frequency so that the visibility data could be averaged in time. The data were averaged in time and subjected to a further round of editing in IBLED which removed outliers in the visibility amplitudes and phases. By averaging the data over periods of $\sim$ 20 s the volume of data to be edited was significantly reduced.

3.8.1 Crosscorrelation bandpass

As in the case of the autocorrelation bandpass solution, the goal of this calibration step is to obtain a time-independent characterisation of the frequency-dependent gain of the receiving system. In this case, the calibration procedure must solve for both the phase and amplitude of the net bandpass response at each antenna. This is implemented using a least-squares fitting procedure to estimate the antenna-based complex gain in each spectral channel using continuum calibrator spectra pre-averaged in time. If this strategy is to be successful the phase slopes introduced by residual group-delays and fringe rates must be removed as accurately as possible before averaging the calibrator spectra together. Thus fringe fitting was performed after the visibility editing took place.

The task BPASS was used to estimate the net bandpass response using

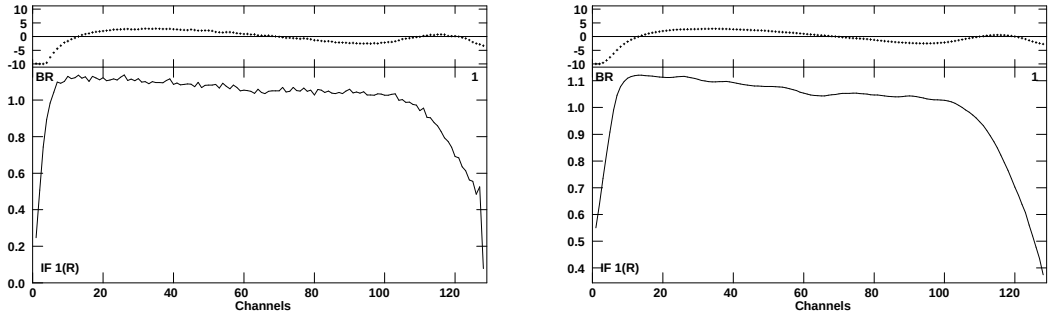

(a) Without Smoothing (b) With Smoothing

Figure 3.5: The bandpass responses of the right-circular receiving system at the Brewster antenna determined by BPASS, before and after smoothing was applied.

the Los Alamos antenna as the reference antenna. As BPASS solves for each spectral channel separately the bandpass solution estimated by BPASS was smoothed using a Hanning smoothing function with a function diameter of 10 channels.

3.8.2 Group-delays

The group-delays, $\tau_m^R(t), \tau_m^L(t)$, for the stronger, blue-shifted spectral windows were obtained by a linear interpolation of the matching continuum calibrator delays. These delays were determined via a straightforward fringe fit of the calibrator data. This fringe fit was performed after the data had been edited and bandpass calibrated. The resultant calibration table was smoothed and any outliers were deleted from the table before proceeding to interpolate these results in time in order to apply them to the source visibilities.

3.8.3 Spectral window group-delay offsets

Unfortunately the signal from the red-shifted emission was so weak as to prevent a successful self-calibration of the phase gains. Thus the phase gains of this spectral window were determined by adopting the phase solutions of the spectral window containing the stronger emission but modified by the

phase and delay offsets between the two spectral windows. These offsets were also determined from the continuum calibrator cross-power spectra. Thus the delay solution for the red-shifted spectral window was constructed from the blue-shifted spectral window as

$$\tau_m^1 = \tau_m^2 + \delta\tau_m^{1-2}, \tag{3.2}$$

where $\delta\tau_m^{1-2}$ is the delay offset between the two spectral windows.

This offset was determined by first applying the phase and delay solutions already obtained from the continuum calibrators in spectral window 2 to the calibrator data in spectral window 1 and then performing another fringe fit for the residual. The results of this second fringe fit were the time-dependent group-delay, fringe rate, and phase delay offsets between the two spectral windows. The fringe rate offset was found, as expected, to be approximately zero. The remaining offsets determined from the calibrators were then linearly interpolated in time to determine the appropriate offsets for the source data.

3.8.4 Polarisation group-delay offsets

There is also a group-delay offset between the two polarisation hands as discussed in section 2.7. This was determined by fringe fitting the cross-hand calibrator data in the Los Alamos to Pie Town baseline. This fringe fit was only performed after the phase gain solutions, determined from the previous round of fringe fitting, were applied to the data. As indicated by equation 2.34, the residual delays in the RL, LR cross-hand spectra, after the application of the parallel hand delay corrections, are equal to the delay offsets (but with opposite sign in LR and RL). Fringe fitting the cross-hand data thus determined two independent estimates of the delay offset over time which were subsequently averaged together and averaged over time. This procedure calculated a delay offset $\delta\tau^{R-L}$ of -68.3 ± 65.3 and 224.7 ± 53.3 ns for spectral windows 1 and 2 respectively.

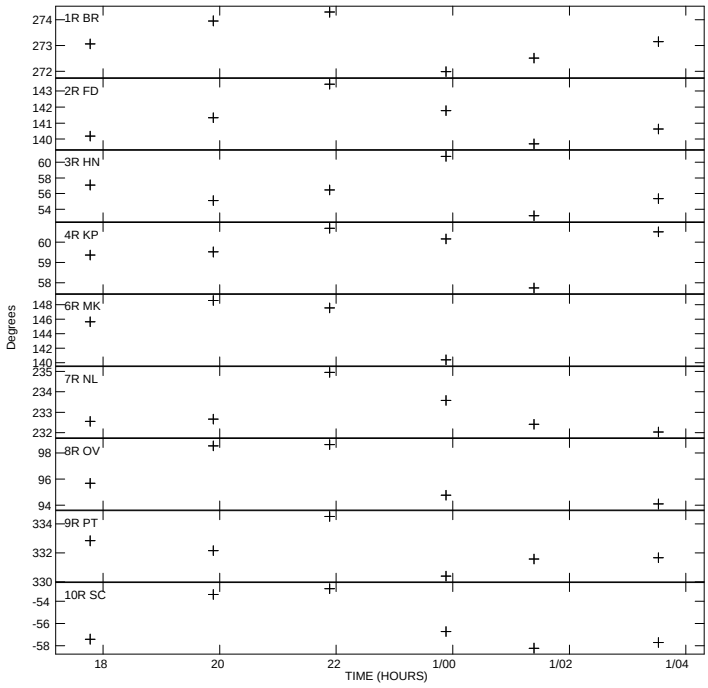

(a) The phase-delay offsets between Spectral Windows 1 and 2

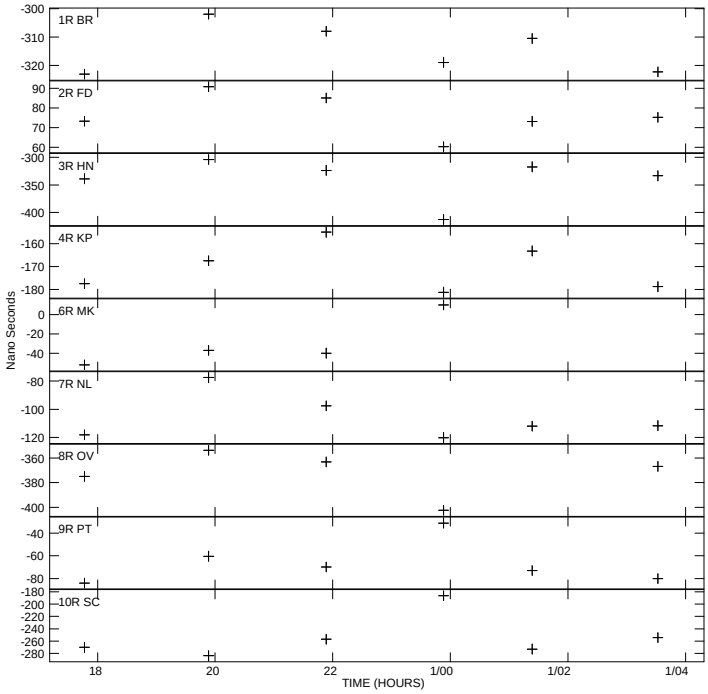

(b) The group-delay offsets between Spectral Window 1 and 2

Figure 3.6: Time-dependent offsets between spectral window 1 and 2.

3.8.5 Phase delay offsets

The determination of the phase delay offset between the two spectral windows was determined using a fringe fitting procedure as described in the previous section. This section with therefore only deal with the method employed to determine the phase offset between the two hands of polarisation.

The first step in the procedure was to apply the group-delay solutions obtained from fringe fitting. This step was a prerequisite for the next step which involved splitting out all the baselines to the reference antenna and then averaging these parallel hand spectra in frequency across the entire observing bandwidth. Taking the difference between the parallel hand phases of these averaged visibilities determines, according to equation 2.37, the following quantities:

$$\Phi_{m0}^{RR} - \Phi_{m0}^{LL} = \delta\theta_{m}^{R-L} - \delta\theta_{0}^{R-L}, m \in 1 \ldots N_a, m \neq 0 \tag{3.3}$$

Thus this procedure determined the phase offset up to an additive constant, a constant which is equal to the phase offset at the reference antenna. The phase offset is expected to be fairly constant throughout the observation and as such the phase offset solutions were examined to determine if they were fairly stable. Large variations in the phase offset were determined at the Pie Town antenna consequently some of the data at this antenna was flagged. A rapidly changing phase offset between the two polarisations may be the result of ionospheric Faraday rotation. An attempt was made to correct for ionospheric Faraday rotation using the AIPS task FARAD. This task calculates the appropriate ionospheric Faraday rotation correction using a phenomenological model of ionospheric electron density. This model, devised by Chiu (1975), takes the Zurich sunspot number as an input. It predicted a peak ionospheric phase rotation of ~ 9 degrees for an input Zurich sunspot number of 44, which was the appropriate sunspot number for Oct 1994.

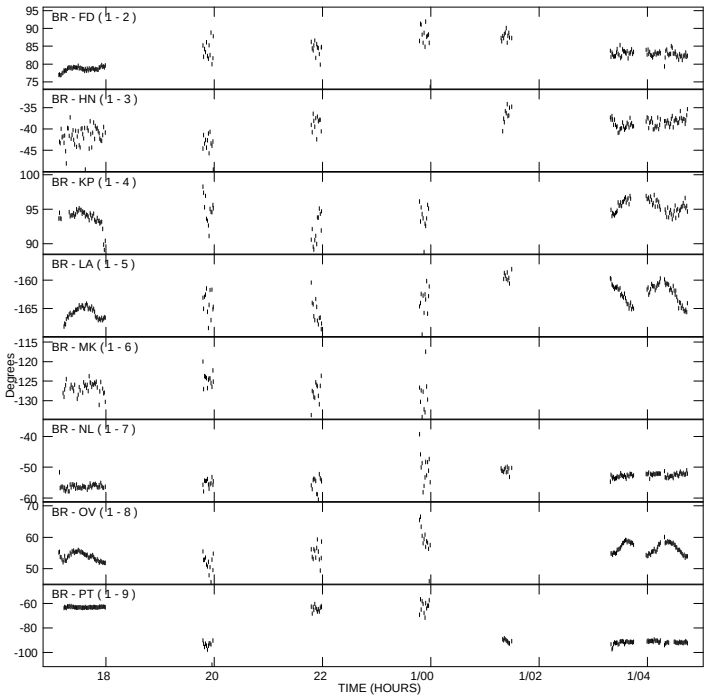

Figure 3.7: The time-dependent difference between the parallel hand phases of the continuum calibrators in spectral window 1.

3.9 OH 0.9+1.3 crosscorrelation data

3.9.1 Phase-delay rate and phase-delay

An initial estimate of the fringe rate and phase is obtained by fringe fitting the source cross-power spectra. This fit was only performed once the results of the amplitude, bandpass and group-delay calibration procedures had been applied to the data. This preliminary fringe fit was performed on channel 74 with V_{LSR}= -123.3 km.s^{-1}, and its primary purpose was to to remove residual fringe rates from the data as the self-calibration procedure is a phase-only correction.

In spectral window 2 the final phase-delays and phase delay rates were estimated via self-calibration on the reference channel (channel 74) in the RR parallel hand data. The details of this procedure are outlined in section 2.14. The self-calibration procedure was implemented by alternately using the CALIB and IMAGR tasks in AIPS. The CALIB task compares (u, v) data with visibilities derived from the source model and calculates the antenna-based phase gains. The phase gains are applied to the data which is subsequently imaged by IMAGR and this image serves as the source model for the next iteration of the algorithm. The initial source model adopted in this procedure was that of a point source and a total of 10 iterations of the algorithm were performed. The first three iterations halted the IMAGR deconvolution at the first negative CLEAN component, thereafter the CLEAN was halted after a specified number of CLEAN components had been removed from the image. The limiting number of CLEAN components removed from the image was increased at each iteration starting from 300 components in the fourth iteration and ending with 4000 components in the final image. In all cases all the CLEAN components found by IMAGR were used in the starting model for the subsequent iteration of CALIB. The solution interval used in CALIB was held constant at approximately 3 minutes for the first three iterations and subsequently the solution interval was linearly reduced at each iteration to yield a final solution interval of approximately 20s.

The final rms noise in the image should be a small multiple of the thermal

noise S:

$$S = \frac{\text{SEFD}}{\eta_s \sqrt{N_{vis} \delta t_{corr} \Delta\nu}}, \tag{3.4}$$

where η_s is the quantisation efficiency, assumed to be unity, N_{vis} is the total number of visibility data points, δ_{corr} is the correlator integration time and $\Delta\nu$ is the bandwidth of the channel. SEFD is the system equivalent flux density which is the system temperature of the array in units of Jansky. It can be obtained by multiplying the system temperature of the array with its point source sensitivity. Using a nominal SEFD of 303 Jy at 18 cm (Ulvestad and Woebel, 2006), a correlator integration time of 9.4 s, a channel bandwidth of 1.9 kHz and a total number of imaged visibilities of 37380 yields a thermal noise of 0.012 Jy. This compares well with off-source rms in the final image of 0.028 Jy.

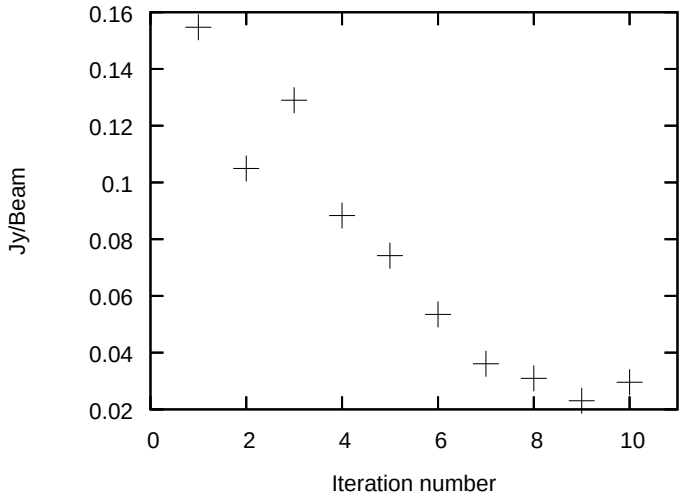

Figure 3.8: The off-source rms versus iteration number.

The fit to the reference channel in closure phase is shown in figure 3.9. After self-calibration the antenna gain phases for the LL parallel hand data were then constructed from the RR solutions as indicated in equation 2.35.

The antenna phase gains for spectral window 1 were then constructed from the phase solutions for spectral window 2 as follows:

$$\phi_m^2(\nu, t) = \phi_m^1(\nu, t) + \delta\tau_m^{2-1}(\nu - \nu_0) + \delta\theta_m^{2-1}, \tag{3.5}$$

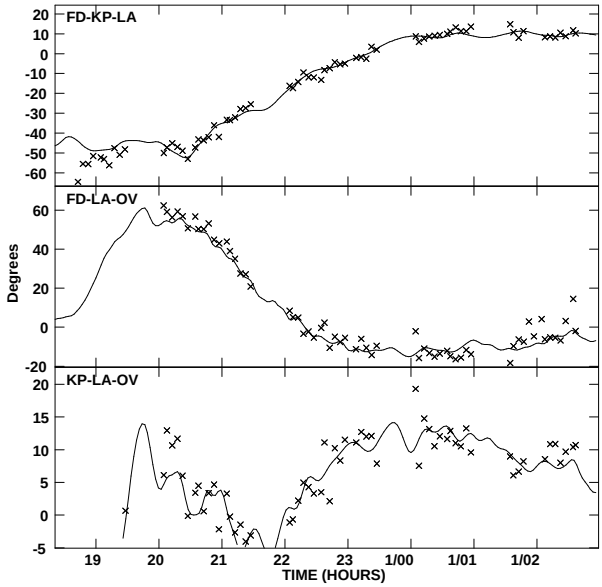

Figure 3.9: The closure phases in Stokes I for the (u, v) data in the reference channel at a selection of short and intermediate baselines. The closure phase predicted by the source model is plotted as a solid line.

where $\delta\tau_m^{2-1}$ is the group-delay offset and $\delta\theta_m^{2-1}$ is the phase-delay offset between spectral windows 1 and 2.

3.9.2 Imaging

The derived antenna gain phases were applied to the data cube to obtain the calibrated data set suitable for generating the Stokes Iand V images. The images were generated by the AIPS task IMAGR which implements the non-linear deconvolution algorithm CLEAN, a uniform weighting scheme was applied to the (u, v) data points before Fourier transforming to the image domain. A restoring beam with dimensions 33.2×12.6 mas was used for all the final maps. The final maps have 1024×1024 pixels and a pixel spacing of 1.7 milliarcseconds

3.10 Polarisation calibration

3.10.1 D-term calibration

The phase and amplitude calibrated data were used to determine the D-terms, representing the degree of instrumental feed contamination. This was achieved by using the spectral line source as a polarisation calibrator where each channel was assumed to be an independent linearly unpolarised source. As explained in section 2.16 the D-terms and the source structure are simultaneously determined from the source cross-power spectrum in a fit to equation 2.39. This fit was implemented using the AIPS task SPCAL where only the channels in the velocity range $V_{LSR} = -118.2$ to -125.5 km.s^{-1} were used in the calibration of spectral window 2. A solution interval of 10 minutes was used in the fit and the results of this procedure are given in the table 3.2. These D-terms are within the expected range for the VLBA. The D-terms determined from spectral window 2 were also used in the instrumental feed calibration for spectral window 1. This step is justifiable because the frequency dependence in the D-terms is usually only significant over frequency intervals much larger than the separation between the spectral windows in this observing configuration. Since the emission in spectral window 2 is much stronger and persists over a larger range of channels it yields a more robust D-term estimation.

After applying a correction for the instrumental polarisation, the Q and U Stokes parameters of the source emission were imaged using the same imaging parameters described above.

3.10.2 Absolute electric vector position angle determination

The absolute position of the source polarisation vector was derived from an associated VLA observation of the polarisation calibrator source 3C286 which has a known polarisation angle of 33°. The observation in question took place on 11 November 1994 and the observing schedule included observations of the continuum source J1613+3412. The VLA observations were

Antennas	D^R		D^L	
	$\mid D^R \mid$	$\arg(D^R)$ (deg)	$\mid D^L \mid$	$\arg(D^L)$ (deg)
Brewster	0.0230	-11.1	0.0355	112.7
Fort Davis	0.0197	-81.1	0.0057	117.1
Hancock	0.0285	38.5	0.0281	59.2
Kitt Peak	0.0044	116.2	0.0104	-152.3
Los Alamos	0.0011	166.1	0.0265	128.8
Mauna Kea	0.0000	0	0.0000	0
North Liberty	0.0217	147.4	0.0227	-62.7
Owens Valley	0.0062	-168.6	0.0144	136.5
Pie Town	0.0115	-108.2	0.0129	151.5
St Croix	0.0236	-115.7	0.0168	179.8

Table 3.2: D-terms solved for in the polarisation calibration step.

reduced in AIPS and the standard calibration for VLA polarisation data was followed. Upon imaging it was determined that 3C286 and J1613+3412 had apparent polarisation angles of $\sim -72^\circ$ and -53° respectively. This implies that the polarisation angles in this set of VLA observations are offset from their absolute values by 105°. Adding this offset to the polarisation angle of the VLA observations of J1613+3412 resulted in a final angle of 52°.

As J1613+3412 was observed as a continuum calibrator in the original set of observations by the VLBA it was possible to compare this true polarisation angle of J1613+3412 with the apparent angle derived in the VLBA observations. The VLBA observations gave an apparent polarisation angle of 54° and as such it is clear that a correction of -2° should be applied to all polarisation vectors derived from these observations.

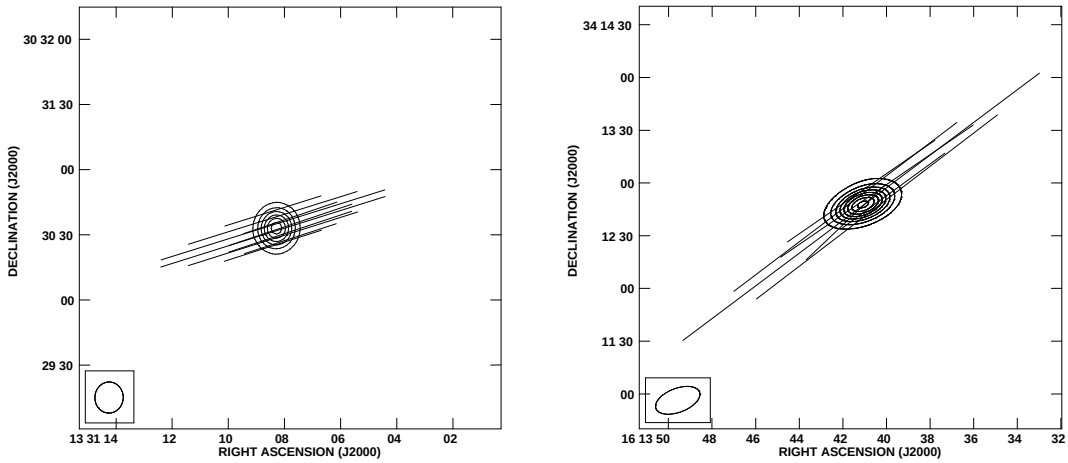

(a) 3C286 (b) J1613+3412

Figure 3.10: Images of the electric vector polarisation angles of 3C286 and J1613+3412 derived from the observations with the VLA.

Chapter 4

Review of Source Properties

4.1 Introduction

It is widely held that OH/IR stars are the precursors of planetary nebulae. These sources undergo a period of intense mass loss which results in a slowly expanding cool gaseous envelope surrounding the central star. This envelope can produce an OH maser line that is detectable throughout the galaxy. There are many complexities in the evolutionary path of these objects. In the transition from AGB to planetary nebula the central star will ultimately ionise the surrounding envelope to form a planetary nebula. This leads to a period where the inner region of the envelope is ionised, resulting in radio continuum emission, while the outer regions remain neutral and as such will continue to exhibit OH maser emission. This transitional period is expected to last only a few thousand years and thus such objects would be relatively scarce. The source OH 0.9+1.3 has been identified as a possible candidate for this evolutionary phase.

The source OH 0.9+1.3 was initially identified as a strong 1612 MHz OH maser emitter by Kerr and Bowers (1974), it was only some time later that the detection of it's associated radio continuum emission by Pottasch et al. (1987) led to speculation that this object may provide an evolutionary link between OH/IR stars and planetary nebulae. The source has no optical counterpart but is a strong infra-red emitter; this is typical of OH/IR stars and young

planetary nebulae as the dust in the circumstellar envelope absorbs much of the stellar radiation and causes a high degree of optical extinction. The dust then re-radiates the emission at infra-red wavelengths (Zijlstra et al., 1989).

This object's unusual evolutionary status requires further investigation and the VLBI maps of the OH masers of this source presented in this thesis will hopefully prove illuminating in this regard. This chapter presents a review of the current literature on OH 0.9+1.3 with a view to interpreting the observations presented in this thesis.

4.2 Maser emission

4.2.1 1612 MHz emission

The 1612 MHz OH emission spectrum has a highly asymmetric double peak profile with a weak red-shifted component at -93.3 km.s^{-1} of 0.5 Jy and several blue-shifted components around 120 km.s^{-1}. The blue-shifted emission consists of four closely spaced components at $-123.5, -122.3, -121.2$ and -116 km.s^{-1} which have varied considerably in relative strengths over the course of several observations (Shepherd et al., 1990; Zijlstra et al., 1989), thus it has been concluded that the source is variable on a timescale of months. This spectral profile can be observed in the spectra obtained by Zijlstra et al. (1989), these spectra are presented in figures 4.1 and 4.2. Single dish observations of the source by Shepherd et al. (1990) in 1988 revealed that the blue-shifted emission underwent a steady increase in flux density at a rate of approximately 1 Jy per year since it was first observed in 1973. The most recent observations by Szymczak and Gérard (2004) using the Nancay radio telescope in 2004 indicate that this trend of increasing flux has persisted over the intervening period and the peak blue-shifted flux density is now in the region of 70 Jy . In contrast the red-shifted emission appears to have remained constant over the same period of time (Szymczak and Gérard, 2004).

The very high velocity of the source combined with its position near the galactic centre indicates that it is part of the galactic bulge which places it

at a distance of approximately 8 kpc.

OH/IR stars typically have a double-peaked spectrum whose components have steep outer and shallow inner slopes. This profile is explained as arising in a spherical uniformly expanding shell where the longest pathlength at a constant velocity occurs along the line of sight through the centre of the nebula. Thus the blue-shifted peak arises from the front of the nebula and the red-shifted peak from the rear. In this scenario the circumstellar envelope is expanding at rate equal to half the velocity separation of the two components which in the case of OH 0.9+1.3 would indicate an expansion velocity of approximately 15 km.s^{-1}. As the inner envelope has high densities, an ionised region of the nebula would rapidly become optically thick at 18cm and as such would absorb much of the emission arising on the far side of the nebula. Hence the relative weakness of the red-shifted peak in OH 0.9+1.3 's spectrum provides further possible evidence of its transitional status.

The presence of three or four separate velocity components in the blue-shifted emission combined with the observation that parts of the same maser group experience different time variations represents a significant departure from the typical OH/IR star. It has been shown that multiple peaks can be caused by strong bipolar outflows (Chapman, 1988), alternative explanations for this structure include an irregular density structure, where individual lines correspond to a density enhancement, and the presence of a velocity gradient in the emitting shell. Work done by Nedoluha and Watson (1988) indicates that a velocity change of a few km.s^{-1} is sufficient to break the spectrum up into multiple narrow lines. This final scenario is deemed particularly attractive in the case of OH 0.9+1.3 by Zijlstra et al. (1989) as the high intrinsic luminosity of this source indicates that the shell is likely to be quite thick.

4.2.2 OH main-line emission

Preliminary observations by Pottasch et al. (1987) indicated the presence of weak 1665 MHz emission at the level of 200 mJy. This result was confirmed by Zijlstra et al. (1989) who also observed 1667 MHz OH emission.

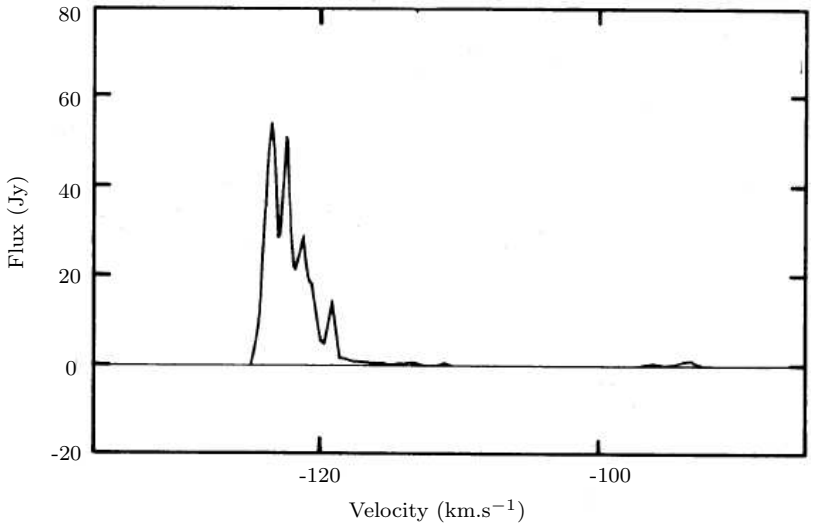

Figure 4.1: The 1612 MHz spectrum of OH 0.9+1.3 obtained by Zijlstra et al. (1989). This spectrum is of the right circularly polarized emission only.

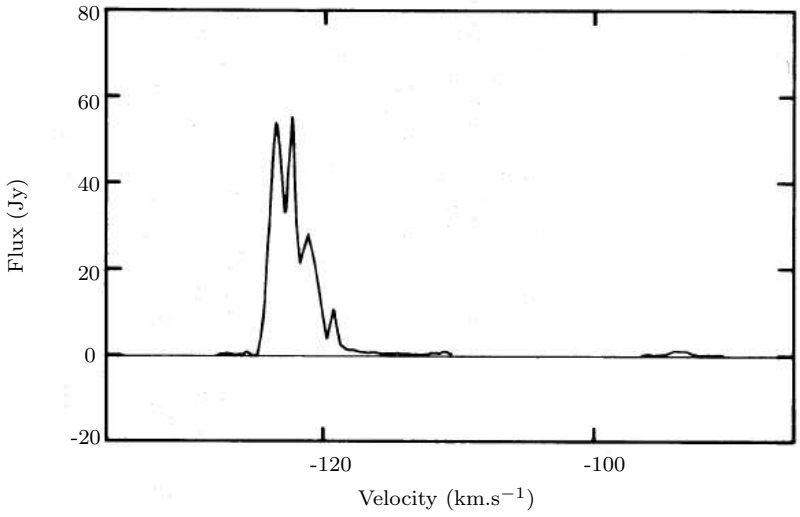

Figure 4.2: The 1612 MHz spectrum of OH 0.9+1.3 obtained by Zijlstra et al. (1989). This spectrum is of the left circularly polarised emission only.

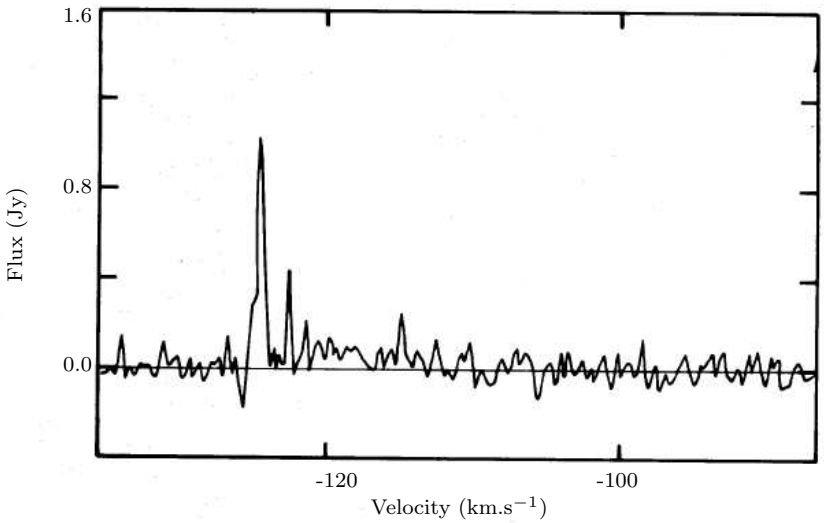

Figure 4.3: The 1667 MHz spectrum of OH 0.9+1.3 obtained by Zijlstra et al. (1989). This spectrum is of the right circularly polarised emission only.

The emission spikes in the 1667 MHz spectrum are coincident in velocity with the 1612 MHz emission and the strongest of these has a flux density of approximately 1.3 Jy. Additional features in the spectrum include a weak plateau of emission extending from -125 to -93 km.s^{-1} and an absorption feature at -125.9 km.s^{-1} coinciding with the edge of the 1612 MHz profile. The 1667 MHz spectra obtained by Zijlstra et al. (1989) are reproduced in figures 4.3 and 4.4.

The 1665 MHz emission is by far the weakest of the three maser lines with a peak flux density of 150 mJy in a maser feature centred on -124 km.s^{-1}. Unfortunately no observations have been done to determine whether there is a 1665 MHz counterpart to the emission feature at -93 km.s^{-1} seen in 1612 MHz emission. A comparison between the blue-shifted emission of the 1665 MHz and 1612 MHz emission reveals a clear correlation between these features with a peak in the 1612 MHz emission corresponding to a dip in the 1665 MHz profile. This is illustrated in figure 4.5 where the spectra of these two lines of emission, obtained by Zijlstra et al. (1989), are overlaid in the same plot. This interesting feature can be explained

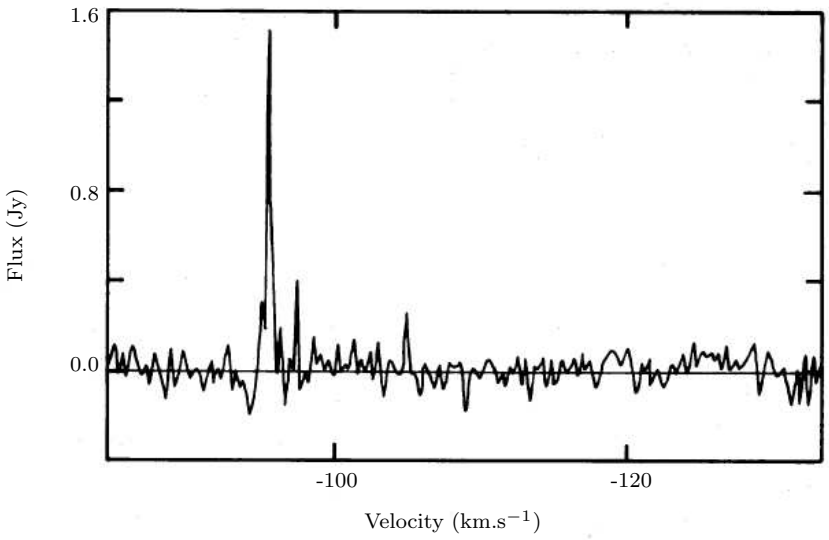

Figure 4.4: The 1667 MHz spectrum of OH 0.9+1.3 obtained by Zijlstra et al. (1989). This spectrum is of the left circularly polarised emission only.

when one considers that the two frequencies share a common upper level but have different ground levels, thus they compete for the same inverted OH population as they saturate the medium. This process is known as competitive gain. Field (1985) has performed some calculations on the effects of competitive gain in the relative amplitudes of maser lines. In the scenario where the 1612 MHz line saturates before the 1665 MHz line has reached sufficient intensity to do so the latter frequency is strongly suppressed as each 1665 MHz and 1612 MHz photon which gets absorbed by OH will be rapidly picked up by the saturated 1612 MHz maser. This line locking between the two maser lines can explain the observed correlation between the spectra.

It has been proposed that the presence and relative strengths of main-line masers may be used to classify an OH source. An early classification scheme proposed by Turner (1970) indicates that sources where the main-line emission is stronger than the 1612 MHz satellite-line emission are likely to be HII regions, these are classified as Type I maser objects. Objects where the reverse is true, classified as type IIb objects, are then thought to be evolved objects such as OH/IR stars. With a 1612 MHz emission line that is

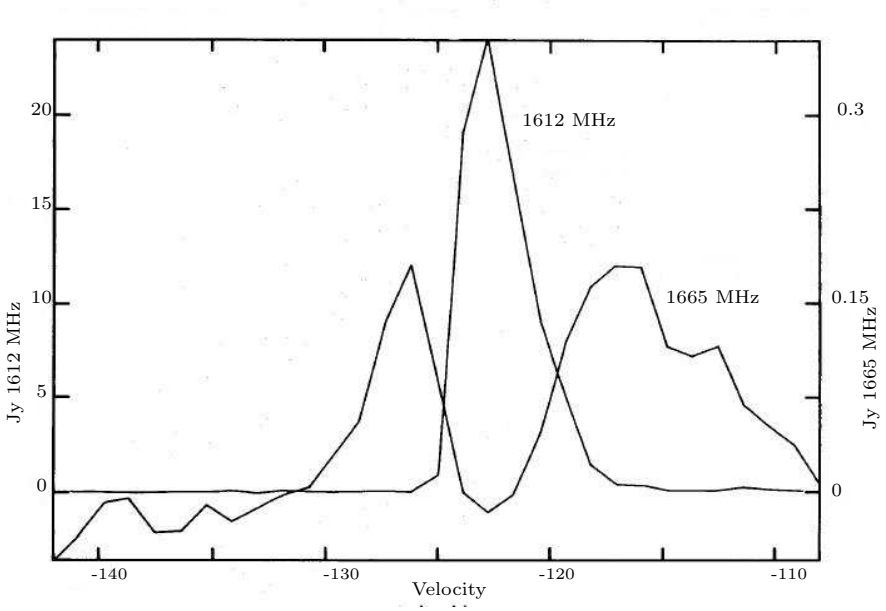

Figure 4.5: The 1612 MHz spectrum of OH 0.9+1.3 with the 1665 MHz spectrum overlaid taken from (Zijlstra et al., 1989). This figure illustrates the phenomenon of line-locking in this source.

approximately 100 times the strength of the 1665 MHz emission OH 0.9+1.3 is an object which is placed firmly in the latter catergory. However Zijlstra et al. (1989) have warned that such a scheme should be used with caution as there are several objects which do not conform to these norms.

Lewis (1989) has proposed an evolutionary sequence for the transition from the AGB to the planetary nebula stage. In this sequence OH main-line emission appears at the early stage of the formation of the circumstellar envelopes and in its terminating proto-planetary emission but doesn't appear nearly as predominantly at the intermediate stages of the envelopes evolution. It has been suggested that competitive gain with the 1612 MHz emission in the thick outer shell may be responsible for the disappearance of the main-line emission at the intermediate stages a situation which is reversed when the shell is no longer renewed. Thus the detection of this emission in OH 0.9+1.3 could be an indicator of its evolved status.

4.2.3 Other maser lines

A search for SiO and H_2O maser emission at 43 GHz and 22.2 GHz respectively by Gomez et al. (1990) did not detect any emission associated with the source. More recent searches for SiO emission at both 43 and 86 GHz by Mauersberger et al. (1988),Nyman et al. (1993) and Nyman et al. (1998) were similarly unsuccessful. The lack of SiO masers could indicate that the fast stellar wind has recently turned on as this wind would destroy SiO masers in the inner shell. As SiO masers exist in a region that is closer to the central star than any other type of maser they are the first to be affected by changes in the stellar wind. Interactions between the more recent wind and older slower winds result in turbulent conditions which destroy the velocity coherence required for maser emission as a result the maser emission ceases.

No 6.7 GHz methanol masers were detected in surveys conducted by van der Walt et al. (1996) and Walsh et al. (1997).

4.3 Thermal molecular emission

Mauersberger et al. (1988) detected CO emission in the J=1-0 and J=2-1 lines. These emission lines were determined to have peak main-beam brightness temperatures of 0.19 and 0.26 K respectively and used to determine the mass loss rate of the central star as being $2\times10^{-4}M_{\odot}.yr^{-1}$. It should be noted that the estimation of mass loss rates assumes a spherically symmetric outflow and many PNe and PPNe have bipolar or irregular outflows.

The CO emission spectra affords two additional methods for determining the expansion velocity, in the first instance it can be derived as half the linewidth in the emission spectrum. Alternatively the difference between the centroid velocity of the CO, measured as -107 $km.s^{-1}$, and the OH maser velocities should also equal the expansion velocity. Both these methods yield values of approximately 15 $km.s^{-1}$ which is in good agreement with the value derived solely from the OH velocity profile.

A survey by Bronfman et al. (1996) for the CS(J=2-1) rotational transition line at 98 GHz did not detect any emission.

4.4 Continuum observations

The radio continuum emission was first detected by Pottasch et al. (1987) who observed the object using the VLA in the B configuration at 2 cm and in the C configuration at 6 cm. These measurements yielded flux densities of 3 and 1.4 mJy respectively. Continuum emission was also detected at 2 cm by Zijlstra et al. (1989) and at 3.6 cm by Yusef-Zadeh et al. (1996) using the VLA thus confirming the PPNe status of this object.

4.5 Infra-red emission

The source is designated as IRAS 17393-2727 in the IRAS point source catalogue, it has a low variability index and the flux densities are as listed in table 4.1.

12 μm	25 μm	60 μm
1.83 Jy	17.83 Jy	36.85 Jy

Table 4.1: IRAS flux densities of OH 0.9+1.3.

There have been various attempts to use the IRAS two color diagram to describe stellar evolution from the AGB to the planetary nebulae phase (Bedijn, 1987; van der Veen and Habing, 1988) and these measured flux densities place OH 0.9+1.3 in the region of the diagram which is largely, but not exclusively, occupied by planetary nebulae (Sevenster, 2002). In general OH/IR stars have a much higher ratio for the 12 to 25 micron flux, the lower value that OH 0.9+1.3 exhibits indicates the presence of a cool evolved dust shell (Pottasch et al., 1987).

More recent measurements of this source's infra-red emission are given in the MSX Infra-red Point Source Catalog. The flux densities measured by this satellite are given in table 4.2.

Both Zijlstra et al. (1989) and Pottasch et al. (1987) used IRAS fluxes to estimate the total observed far infra-red flux of this object. These estimates

4.29 μm	4.35 μm	8.28 μm	12.13 μm	14.65 μm	21.34 μm
-10.30 Jy	-0.56 Jy	0.25 Jy	1.05 Jy	2.96 Jy	10.72 Jy

Table 4.2: MSX flux densities of OH 0.9+1.3.

combined with the source flux density at the shortest observed wavelengths were subsequently used to calculate an upper limit for OH 0.9+1.3's infra-red Excess (IRE). The IRE is defined as the ratio of the observed total far infra-red flux, F_{FIR}^{obs}, over the expected far infra-red flux due to absorption by dust of nebular Lyman-α photons, F_{FIR}^{exp}. The expected far infra-red flux is derived from the optically thin radio flux density. Since it is not known whether the radiation at the shortest observed wavelength is optically thin or not the calculated IRE can only be regarded as an upper limit.

It is thus possible to use the updated MSX flux measurements to obtain an improved estimate of the observed total far infra-red flux and IRE. Integrating over the MSX flux measurements as well as IRAS measurements at the longer wavelenghts determined a total far infra-red flux of $2.70 \times 10^{-12}\ W\ m^{-2}$ and an IRE of 96. These values compare very well with those calculated by Zijlstra et al. (1989). They calculated an IRE of 73 and a total far infra-red flux of $F_{FIR}^{obs} = 2.12 \times 10^{-12}\ W\ m^{-2}$. This is a very high IRE and fully evolved PNe generally have much lower IRE of less than 3. Thus this high IRE would seem to indicate that this source is still undergoing a transition process.

The luminosities of the central star was found by Pottasch et al. (1987) under the assumption that it was equal to the total infra-red luminosity derived from the total infra-red flux. This luminosity of $6.7 \times 10^3\ L_\odot$ gives a corresponding momentum rate of $\frac{L}{c} = 8,6 \times 10^{26}$ erg.cm^{-1}. This momentum rate can be compared to the momentum of the molecular outflow $\dot{M}V_{exp} = 3 \times 10^{27}$ erg.cm^{-1} which is calculated using the mass loss rate derived from CO measurements (Mauersberger et al., 1988). Thus the momentum of the molecular flow is a factor of $\beta > 3.5$ larger than the momentum of the stellar photons. This result is consistent with the recent assertion of Bujarrabal et al. (2001) that many PPNe have outflow momenta too large to be driven

	$F_{OH}/F_{25\ \mu}$	$F_{OH}/F_{60\ \mu}$
OH 349.2-0.2	0.03	0.006
OH 0.9-1.3	1.4	0.68
Vy 2-2	0.05	0.14

Table 4.3: Ratios of OH maser flux to far infra-red flux calculated by Pottasch et al. (1987).

by radiation pressure from the central star. It also fits in with the result by Knapp (1986) which indicates that while most evolved AGB stars have $\beta \leq 1$ the opposite is true for PNe and PPNe. Thus this ratio provides further evidence that OH 0.9+1.3 is evolving beyond the AGB.

It is worth noting that as the OH satellite masers are pumped by IR emission in the envelope the ratios of the OH flux to the 60 and 25 μm IR flux provide rough lower limits to the 53 and 36 μm pumping efficiencies. Pottasch et al. (1987) calculated these ratios, presented in table 4.3, for OH 0.9+1.3 and two other PPNe candidates.

As discussed previously, Elitzur et al. (1976) calculated that the average pumping efficiency in OH satellite maser lines is approximately 25%. Upon examining table 4.3 it is thus clear that the ratios obtained for OH 0.9-1.3 are extremely high and do not appear to be completely consistent with infra-red radiative pumping. This may imply that a different or additional pumping mechanism is present in this system (Pottasch et al., 1987).

4.6 Radio interferometry at 1612 MHz

The 1612 MHz masers were resolved for the first time by Shepherd et al. (1990) using the MERLIN radio interferometer. They presented maps of both red and blue-shifted emission with a velocity resolution of 1.3 km.s^{-1} and a restoring beam of 0.2×0.4 arcseconds. These maps are presented in figure 4.6. In these observations the source showed evidence of the thin-shell structure characteristic of OH/IR stars and thus it seems very likely the OH

emission is indeed a fossil remnant of the OH/IR phase.

Fitting the thin-shell model to the emission yielded the estimates of 0.24±0.03 arcseconds for the shell radius which at an inferred distance of 8 kpc gives an absolute radius of 2.9×10^{14} m. This compares very well with the radius of 3.9×10^{14} m determined from the mass loss rate and the assumed strength of the ambient ultraviolet radiation field.

The fit also estimates 15.2±0.5 km.s^{-1} for the expansion velocity and a central velocity of -107±0.5 km.s^{-1} which is in excellent agreement with values obtained from the CO observations.

A final point of interest was that not all of the emission followed the thin-shell model and some of the powerful blue-shifted emission near -120 km.s^{-1} came from a compact region nearer the line of sight to the star. This may be associated with a disruption of the molecular envelope by stellar ultraviolet radiation of a fast stellar wind.

Further observations of the red-shifted emission of this source are presented by Migenes et al. (1995). These observations were also made using MERLIN but an improved signal-to-noise ratio on the longest baseline afforded better resolution.

4.7 Polarisation

The polarisation properties of OH maser emission provides one of the most important tracers of magnetic fields in the outer circumstellar regions of post-AGB stars and can provide information of the direction, strength and orientation of the magnetic fields (Szymczak and Gérard, 2004). Circular polarisation from OH 0.9+1.3 was first detected by Zijlstra et al. (1989) at a level of approximately 10% in the 1612 MHz maser line. A more recent study by Szymczak and Gérard (2004) investigated the polarisation properties of 47 PPNe candidates, including OH 0.9+1.3, at 1612 and 1667 MHz using the Nançay Radio Telescope. The properties of the strongest polarised OH emission feature detected in OH 0.9+1.3 by this survey are listed in table 4.4.

The paper by Szymczak and Gérard (2004) noted two interesting features of the polarisation observations of this source. The first of these is

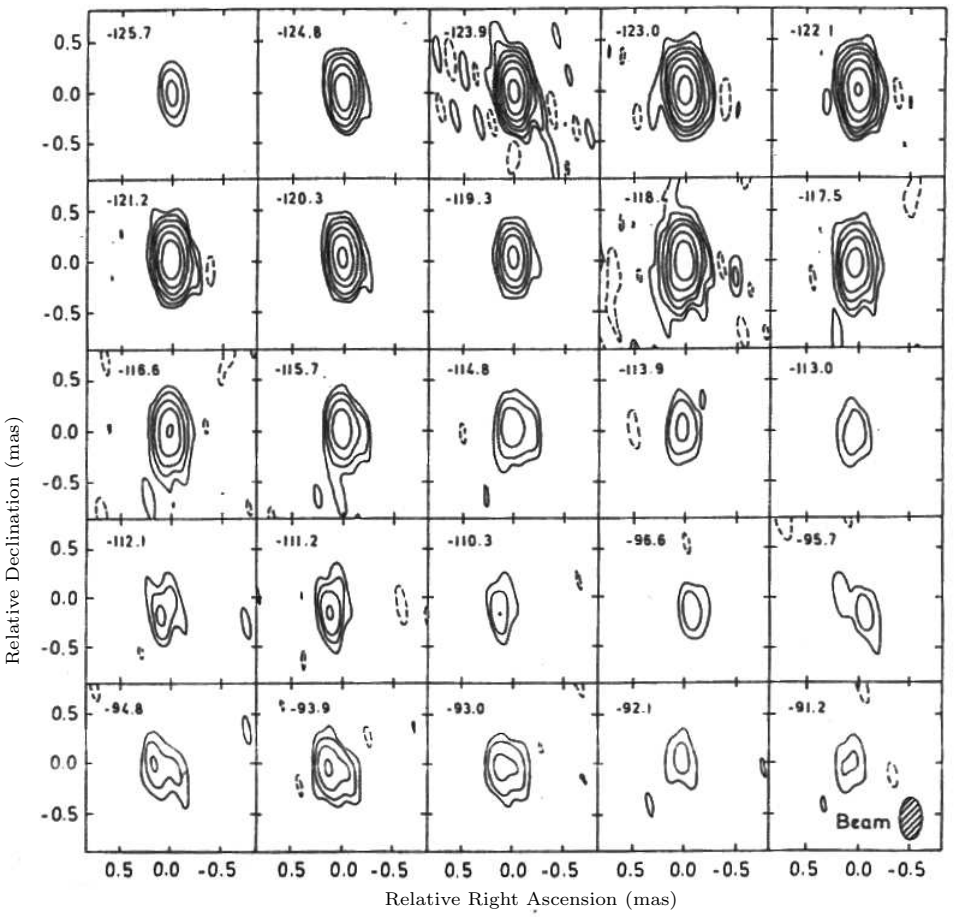

Figure 4.6: Maps of OH 0.9+1.3 made by Shepherd et al. (1990) using the MERLIN array. Contours are plotted at -0.05 (dashed), 0.05, 0.1, 0.2, 0.4, 0.8, 1.6, 2.4, 3.2, 6.4, 12.8, 25.6 Jy per beam.

Line (MHz)	V_c (km.s^{-1})	$m_c(\sigma)$ (%)	V_l (km.s^{-1})	$m_l(\sigma)$ (%)	$\chi(\sigma)$ (°)
1612	-120.5	12.9 (0.8)	-123.5	4.2 (0.2)	-60.8 (3.3)
1667	-124.5	-13.5 (3.2)	-124.5	24.3 (4.3)	6.6 (13.8)

Table 4.4: The strongest polarised feature in OH 0.9+1.3. Here V_c is the velocity of the most circularly polarised feature and m_c is the percentage of circularly polarised emission in this feature. Similarly V_l is the velocity of the strongest linearly polarised emission feature and V_l is the percentage of linearly polarised emission.

that the polarisation angle varies considerably across the polarised frequency spectrum. The source OH 17.7-2.0 also displays this feature and has been revealed to have a large scale regular magnetic field structure (Bains et al., 2003). As such the author speculates that large variations in polarisation angle with frequency may be an indicator for structured magnetic fields and if this is the case identifies OH 0.9+1.3 as the best candidate in the sample in which to map such a field. This is because the source has a polarised flux density of greater than 1 Jy over a velocity extent of greater than 6 km.s^{-1} and the polarisation angle varies from -90° to 90° in a characteristic way.

The second point of interest is that the source exhibits a decreasing degree of polarisation with increasing intensity. This effect was observed in the linear polarisation spectra of two other sources and could be described by a power law $m_L = AI^{\alpha}$ where $\alpha = -0.57 \pm 0.05$ effectively characterises all the data from these three sources. This depolarisation effect is also observed in the circularly polarised emission of the source, no depolarisation is observed in the circularly polarised emission of sources which did not display this effect in the linear polarisation. This suggests that the mechanism which causes depolarisation is common to both the linear and circular emission (Szymczak and Gérard, 2004).

In searching for an explanation for this depolarisation effect the authors noted that sources which do not show depolarisation have an extremely low

dispersion, (°), in the position angles of their linear polarisation vectors, between 1°.2 and 2°.3. In contrast depolarised sources typically have a much higher dispersion of between 4°.3 and 12°.5. Thus it was suggested that depolarisation depends on the global magnetic field structure in the envelope where sources without depolarisation have magnetic fields whose projections are well aligned along specific polarisation angles and those with depolarisation have a far more complex arrangement of magnetic fields.

Chapter 5

Results and Analysis

5.1 Introduction

The final imaging process resulted in an image cube for each of the four Stokes parameters for both the red- and blue-shifted emission of the source. The velocity profiles of the integrated flux from the deconvolved image in each channel in the Stokes I, V and P parameters are given in figure 5.1. It is clear that the Stokes I profile of the blue-shifted emission is very strong ($\sim$50 Jy) and irregular, it consists of four separate emission features each centred at approximately -124, -123, -122 and -119 km.s^{-1}. The red-shifted emission is considerably weaker than the blue-shifted emission with a peak emission feature of 600 mJy. It consists of three emission features at -93, -92.5 and -92 km.s^{-1} and it is thus consistent with the red-shifted emission feature reported by Zijlstra et al. (1989). This spectral profile was explained by Zijlstra et al. (1989) as originating in a shell structure expanding at constant velocity where the red-shifted emission is absorbed by a small ionised region in the centre of the expanding envelope.

The Stokes V profile of the blue-shifted emission consists of five separate features with only one of these being positive. The blue-shifted emission of the linearly polarised flux consists of four distinct emission peaks which are easily identified with the four emission features visible in the Stokes I profile. It is interesting to note that the second strongest peak in the linearly

polarised emission is associated with the weakest feature in the total intensity profile.

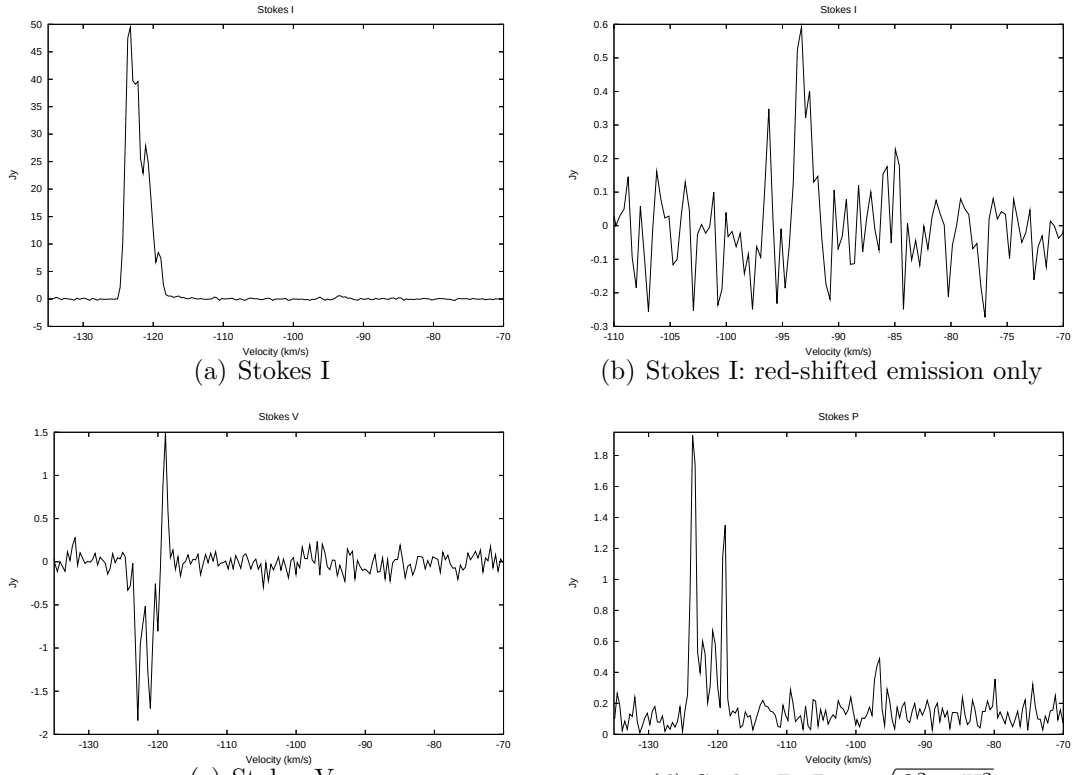

(a) Stokes I

(b) Stokes I: red-shifted emission only

(c) Stokes V

(d) Stokes P: $P = \sqrt{Q^2 + U^2}$

Figure 5.1: Velocity profiles of the integrated flux in the final CLEANed maps.

The total-power autocorrelation spectrum of the observed OH emission is given in figure 5.2. A comparison of the total flux in this spectrum with the recovered total flux density in the final Stokes I image reveals that a substantial amount of flux has been lost because of the lack of intermediate baselines in the VLBA. The flux recovered in the synthesis image is approximately 67% of the total power in the autocorrelation spectrum. The spatial distribution of this missing flux is unknown.

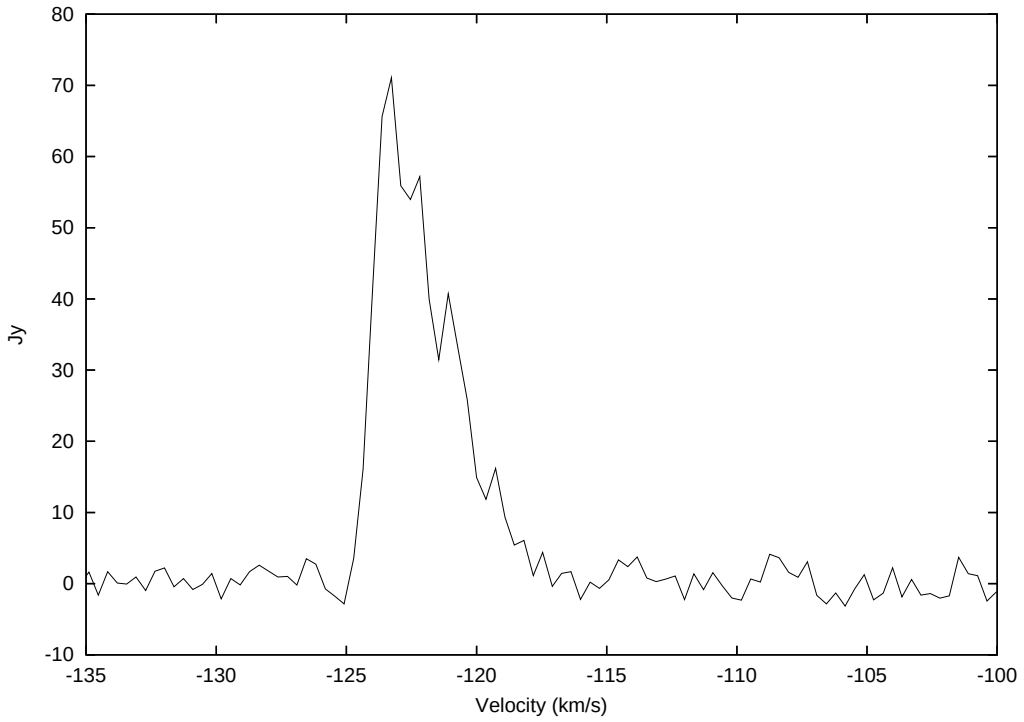

Figure 5.2: Single-dish autocorrelation spectrum in Stokes I of the OH maser emission of OH 0.9+1.3 taken from the Los Alamos antenna.

5.2 Maser components

The individual Stokes I components were fitted by elliptical Gaussian components in relative right ascension and declination. This was achieved using the AIPS task JMFIT which uses a least-squares minimisation to fit an elliptical Gaussian to an interactively defined rectangular region. This rectangular region is selected such that it tightly encloses the fitted component in the image plane. This process resulted in a total of 72 believable components.

The individual channels in the Stokes I, Q, U and V cubes are subject to a non-Gaussian noise distribution resulting from systematic calibration and imaging errors. These are caused by inadequate (u, v) sampling as well as calibration and deconvolution errors which typically add a non-Gaussian tail to the noise distribution. In practice these errors vary across the map and are most dominant in the central region of the image. Consequently the measured off source rms in each channel, denoted by σ_I^0, systematically

underestimates the noise variance of the central regions of the map. Negative values in the Stokes I maps, which have no physical interpretation, provide some measure of these systematic errors and were thus used to broaden the rms noise estimates. The broadened noise rms estimates were obtained by the method outlined in Kemball (1992). Following this method the noise rms is broadened by assuming that the deepest negative is obtained with a probability of $\frac{1}{1024\times1024}$ in a map with 1024×1024 pixels. The broadened rms is calculated by multiplying the off-source rms, σ_I^0, by a factor β where $\beta = \frac{|I_{neg}|}{4.768\sigma_I^0}$. The deepest negative and the off source rms in each channel was found using the AIPS task IMSTAT. The value 4.768 is the value X such that the integral from minus infinity to X of the standard normal distribution is equal to a probability of $\frac{1}{1024\times1024}$. Thus 4.768 is the solution to the equation:

$$\frac{1}{1024 \times 1024} = \int_{-\infty}^{X} \frac{1}{\sqrt{2\pi}} e^{\frac{-t^2}{2}} dt \tag{5.1}$$

Each OH maser component extends over multiple channels. Thus the fitted Stokes I components were grouped into a single spectral feature if they occurred in 2 or more adjacent channels with positions within 30 milliarcseconds of their occurrence in each consecutive channel. This coincidence requirement ensures that each of the grouped maser components are co-located within the CLEAN beam size. This process resulted in 18 maser features, the details of which are given in table 5.1. The spectral channels have a nominal velocity separation of 0.363 km.s^{-1}, this separation does not correspond to the spectral resolution of the observations as this depends on the fast Fourier transform weighting in the correlator. The velocity width of each Stokes I feature was determined from a one-dimensional Gaussian fit over velocity. This field is left blank for those cases where a reliable fit could not be obtained. The right ascension and declination quoted in this table is the peak position, derived from the two dimensional elliptical Gaussian fit, of the component with the highest intensity in the group. The quoted positions are relative to the centre of the map. The errors in the component positions were found using the method of Condon (1997) which deals with errors in elliptical Gaussian fits. These were transformed into a convenient

form for right ascension and declination measurement by Kogan (1996) as given below:

$$\begin{aligned}\sigma_\alpha^2 =& \frac{2}{\rho^2}\frac{1}{8ln(2)}(\theta_M^2 sin^2\phi + \theta_m^2 cos^2\phi) \\ \sigma_\delta^2 =& \frac{2}{\rho^2}\frac{1}{8ln(2)}(\theta_m^2 sin^2\phi + \theta_M^2 cos^2\phi)\end{aligned} \tag{5.2}$$

Here σ_α and σ_δ are the errors in right ascension and declination, θ_M and θ_m are the major and minor axis of the fitted Gaussians and ϕ is the position angle of the major axis. The parameter ρ is a measure of the overall signal-to-noise ratio of the Gaussian fit. Kogan (1996) evaluates ρ in two limiting cases: that of an extended source and a point source. In the intermediate case of a partially resolved source this becomes a difficult quantity to evaluate and it is suggested that an interpolation of the results at the two extremes might be appropriate. As the observations in this work fall into this intermediate category the factor $\frac{2}{\rho^2}$ is given by the expression:

$$\frac{2}{\rho^2} = \frac{\sigma_I^2}{I^2}\left[0.8 + \frac{1}{4}\left(\frac{\theta_{bM}\theta_{bm}}{\theta_M\theta_m} - 0.1\right)\right] \quad \text{if } 0.1 \leq \frac{\theta_{bM}\theta_{bm}}{\theta_m\theta_m} < 0.9, \tag{5.3}$$

where the θ_{bM} and θ_{bm} are the major and minor axis of the CLEAN restoring beam and σ_I is the broadened noise variance (Kogan, 1996). The formal error estimates need to be adjusted using the Kogan (1996) expressions to adjust for the fact that the noise in adjacent pixels is not independent in the deconvolved image.

5.3 Polarised maser components

The polarisation state of the source radiation can be most conveniently quantified via the fractional linear polarisation m_l and fractional circular polarisa-

tion m_c. These quantities are derived from the Stokes parameters as follows:

$$m_l = \frac{\sqrt{Q^2 + U^2}}{I} = \frac{P}{I}$$
$$m_c = \frac{V}{I} \tag{5.4}$$

These quantities were calculated for the individual maser features by extracting the values of the Stokes parameters at the pixel position where the peak of the strongest maser component in the feature occurred. Both m_c and m_l are drawn from non-Gaussian probability distributions and the significance of a detection should be carefully considered. This work adopted the criteria for the rejection of false detections developed by Kemball (1992). Here the measured off-peak RMS noise in each image, $\sigma_I^0, \sigma_V^0, \sigma_U^0, \sigma_Q^0$, was found in an off-source box in the corner of the image. These values were broadened using the assumed Stokes I noise variance to give $\sigma_V = \beta\sigma_V^0, \sigma_U = \beta\sigma_U^0, \sigma_Q = \beta\sigma_Q^0$, where β is given by $\beta = \frac{|I_{neg}|}{4.768 \times \sigma_I^0}$. Kemball (1992) asserts that a non-zero fractional linear or circular polarisation can be established with 95% confidence if $m_l > u_l$ and $m_c > u_c$ where u_l, and u_c are given by:

$$u_c \sim \frac{1.96\sigma_V}{I}$$
$$u_l \sim \frac{1.65}{\sqrt{2}} \left[\frac{P + \sigma_P}{I - \sigma_I} - \frac{P - \sigma_P}{I + \sigma_I} \right], \tag{5.5}$$

where $\sigma_P = \frac{\sqrt{Q^2\sigma_Q^2 + U^2\sigma_U^2}}{P}$. Consequently u_l and u_c were adopted as the fractional linear and circular polarisation thresholds above which a detection was considered to be genuine. In cases where the determined percentage polarised emission was found to be below the calculated threshold the appropriate u_l or u_c value for the feature is quoted instead of the percentage circular or linear polarisation in table 5.1. To distinguish these two circumstances u_l and u_c values are quoted in italics.

The fractional linear polarisation has a Rice probability distribution for symmetric Q and U distributions and the calculated value of m_l needs to be corrected for bias so as not to overestimate the true linear polarisation

(Wardle and Roberts, 1988). Thus the true fractional linear polarisation m_l' was calculated using:

$$m_l' = \frac{\sqrt{Q^2 + U^2 - \sigma_{QU}^2}}{I}, \tag{5.6}$$

where $\sigma_{QU} = \sqrt{\sigma_Q \sigma_U}$ for $\sigma_Q \approx \sigma_U$ (Kemball, 1992). This correction is negligible in the case of a strong signal to noise ratio, the corrected m_l' are the values quoted in table 5.1. The random probability distribution for the fractional circular polarisation m_c is symmetric about zero and therefore does not need to be corrected for bias.

For $m_l > 0$ the position angle χ for the linearly polarised emission was calculated as:

$$\chi = \frac{1}{2} \arctan\left(\frac{U}{Q}\right) \tag{5.7}$$

The probability distribution for χ is symmetric and thus no correction for statistical bias is necessary (Wardle and Roberts, 1988). The position angle listed in table 5.1, is measured from north through east. The calibrated, imaged visibilities have a polarisation angle which is offset from the true polarisation angle. Using the process outlined in section 3.10.2 this offset was determined to be $-2°$. The polarisation angle quoted in table 5.1 is the angle determined from the final Stokes Q and U image cubes corrected for this offset.

For those features with non-zero fractional linear and circular polarisation the uncertainties in these quantities as well as the uncertainties in polarisation angle were calculated according to the relations below (Boboltz, 1997):

$$\begin{aligned} \sigma_l &= \frac{1}{I}\sqrt{\sigma_P^2 + \frac{\sigma_I^2 P^2}{I^2}} \\ \sigma_c &= \frac{1}{I}\sqrt{\sigma_V^2 + \frac{\sigma_I^2 V^2}{I^2}} \\ \sigma_\chi &= \frac{1}{2P^2}\sqrt{U^2\sigma_Q^2 + Q^2\sigma_U^2} \end{aligned} \tag{5.8}$$

Feat. (No.)	V_0 (km.s^{-1})	δV (km.s^{-1})	α (mas)	σ_α (mas)	δ (mas)	σ_δ (mas)	I (Jy)	σ_I (mJy)	V (mJy)	σ_V (mJy)	U (mJy)	σ_U (mJy)	Q (mJy)	σ_Q (mJy)	m_c (%)	σ_c (%)	m_l (%)	σ_{m_l} (%)	χ (deg)	σ_χ (deg)
1_B	-118.910	0.810	-8.039	0.010	31.460	0.017	3.298	0.007	771.262	3.080	57.269	3.322	658.81	3.48	23.39	0.14	19.98	0.15	0.48	0.15
2_B	-118.547	1.066	68.544	0.117	-213.084	0.196	0.223	0.006	-1.169	5.593	-1.053	4.544	2.44	5.04	*4.91*		*5.26*			
3_B	-121.090	1.694	10.980	0.016	10.562	0.026	9.076	0.031	-813.597	15.237	45.700	8.816	60.84	5.51	-8.96	0.13	0.67	0.08	16.45	2.59
4_B	-121.090	1.208	-13.637	0.042	22.187	0.051	2.426	0.031	-103.748	15.237	19.877	8.816	-37.55	5.51	-4.28	0.57	1.53	0.31	74.01	4.30
5_B	-121.453	0.597	26.165	0.255	-121.536	0.388	0.211	0.016	1.220	5.958	2.755	3.723	-0.66	3.68	*5.54*		*4.38*			
6_B	-122.179	1.042	54.108	0.018	-117.468	0.020	3.741	0.019	-123.995	8.295	-1.894	4.431	21.91	6.78	-3.31	0.20	0.57	0.18	-4.46	8.81
7_B	-122.179	1.103	-39.492	0.016	33.091	0.024	4.959	0.019	-300.205	8.295	-93.411	4.431	-81.57	6.78	-6.05	0.14	1.64	0.13	-67.94	1.29
8_B	-125.811		74.736	0.053	-134.244	0.065	0.900	0.014	1.506	6.430	6.045	4.323	-7.08	4.87	*1.40*		*1.24*			
9_B	-127.264	1.281	-1.313	0.008	-2.954	0.012	11.620	0.023	-337.674	12.947	-245.423	6.701	-723.47	4.83	-2.91	0.11	6.23	0.07	-82.63	0.19
10_B	-127.627	0.729	-12.730	0.011	-16.988	0.010	7.229	0.020	-94.002	13.372	-317.034	5.924	-284.33	4.63	-1.30	0.18	3.93	0.10	-67.94	0.36
11_B	-127.627	1.091	11.675	0.017	-20.239	0.024	3.277	0.020	10.808	13.372	-29.835	5.924	-124.92	4.63	*0.80*		3.81	0.60	-85.28	0.06
12_B	-128.354	0.640	37.944	0.068	-115.452	0.096	0.422	0.007	-0.351	4.613	-5.938	3.497	-2.46	4.20	*2.14*		*2.05*			
1_R	-93.311	1.027	109.836	0.149	-15.584	0.194	0.332	0.006	12.865	5.624	-4.271	3.691	-5.91	4.22	6.65	3.03	11.53	2.19	-74.04	15.91
2_R	-93.675	1.096	144.396	0.196	-83.628	0.150	0.268	0.006	0.466	5.595	0.539	4.222	-3.17	5.24	*7.30*		*8.33*			
3_R	-93.675	1.068	-85.140	0.533	-142.776	0.974	0.057	0.006	-1.700	5.595	-4.336	4.222	2.02	5.24	*19.07*		*20.33*			
4_R	-94.401		136.296	0.387	-28.292	0.804	0.069	0.006	4.172	4.725	-1.814	4.649	-1.83	3.91	*13.40*		*15.33*			

Table 5.1: Details of the maser features identified in the final deconvolved map of OH 0.9+1.3. See text for an explanation of the symbols.

5.4 The total intensity contour maps

The contour maps of most of the data-cube channels containing believable emission are presented in figures 5.4, 5.3 and 5.5. The emission is mostly found at velocities clustered around the two emission peaks seen in figure 5.1. The extreme blue-shifted emission consists of a single round blob of emission which at more intermediate velocities (between -122.9 and -121.1 km.s^{-1}) splits up into three distinct components. These components are aligned along an axis of $\sim 135^{\circ}$ with no emission in the north-eastern and south-western regions of the map. In the standard explanation for the double-peaked profile of 1612 MHz maser emission the blue- and red-shifted emission peaks are interpreted as arising from the front and back of a uniformly expanding shell. In this case one expects to see a single round blob of emission in the extreme blue- and red-shifted velocities which opens into a ring of emission at more intermediate velocities. Such ring-like structures are conspicuously absent in the emission maps of OH 0.9+1.3. The red-shifted emission consists of three components two of which exist to the north east of the blue-shifted emission and one which is placed to the south west of it. These contour maps can be compared to the contour maps obtained by Shepherd et al. (1990) using the MERLIN array. In these maps the source emission is largely confined to a single circularly symmetric feature and the blue- and red-shifted emission appear to be located at quite similar positions. In contrast in the VLBA maps, which have a much higher spatial resolution than the MERLIN maps, the blue- and red-shifted emission are found at distinct locations and the blue-shifted emission appears to be preferentially distributed along a preferred axis.

Examining the MERLIN maps in figure 4.6 and comparing them with the images presented in this thesis it is clear that the emission features in the MERLIN maps are considerably larger than those mapped by the VLBA. The largest features in the VLBA maps are of the order of a 100 mas in full extent while most of the features in the MERLIN maps are at least 1000 mas in extent. This discrepancy can be accounted for by the difference in u, v coverage afforded by these two instruments. The MERLIN telescope in the

Shepherd et al. (1990) experiment provided a maximum baseline of 234 km whereas the VLBA has a longest baseline of 8611 km. The higher resolution of the VLBA affords a more detailed view of the source emission consequently the maps provided by this instrument reveal more complex structure than those provided by MERLIN. However the shorter u, v spacings are poorly sampled by the VLBA consequently it is less sensitive to extended emission features and it is likely that the VLBA observations have failed to detect the extended maser emission mapped by MERLIN. This lack of sensitivity to extended emission may also explain why MERLIN detects emission at all velocities ranging from -91 km.s^{-1} to -125 km.s^{-1} and the VLBA emission is detected only at the extreme red- and blue-shifted velocities.

5.5 Stellar position

Knowledge of the stellar position is crucial in analysing and interpreting the OH data. Several different methods for determining the inferred stellar position are advocated in the literature.

- Zijlstra et al. (2001) uses the unweighted centroid of the OH emission for those sources whose stellar position is unknown.
- Alternatively the mean position of the extreme blue- and red-shifted emission can be used.
- If the source is believed to closely resemble a thin uniformly expanding shell then a least-squares fit of the radius-velocity function of such a shell can be performed to obtain the stellar position.
- Finally if the peak feature in the blue-shifted emission is believed to be amplifying the stellar emission then the position of this feature may be adopted (Nedoluha and Bowers, 1992).

In the case of an expanding shell all these methods would ideally yield the same result. Deviations in the source geometry or velocity field from this idealised case will make the determination of this quantity difficult and none

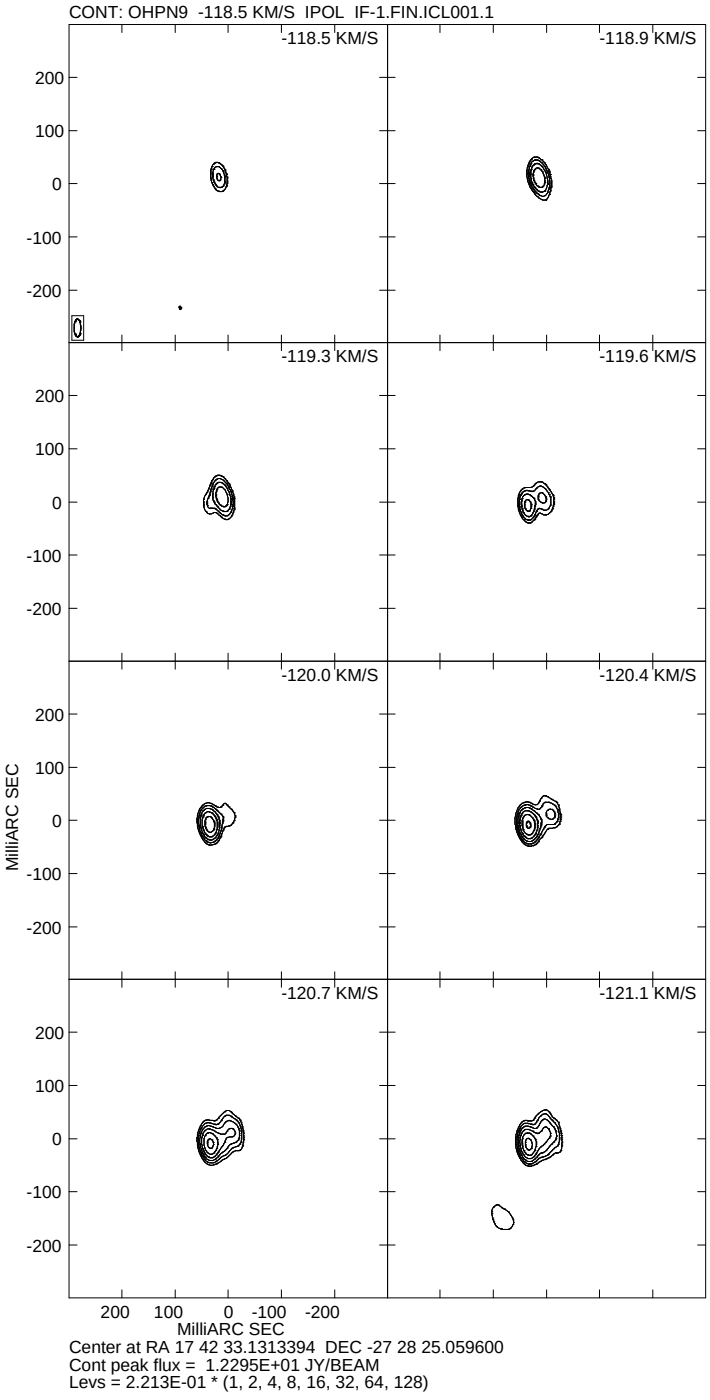

Figure 5.3: Contour maps of the Stokes I emission of the blue-shifted emission from OH 0.9+1.3.

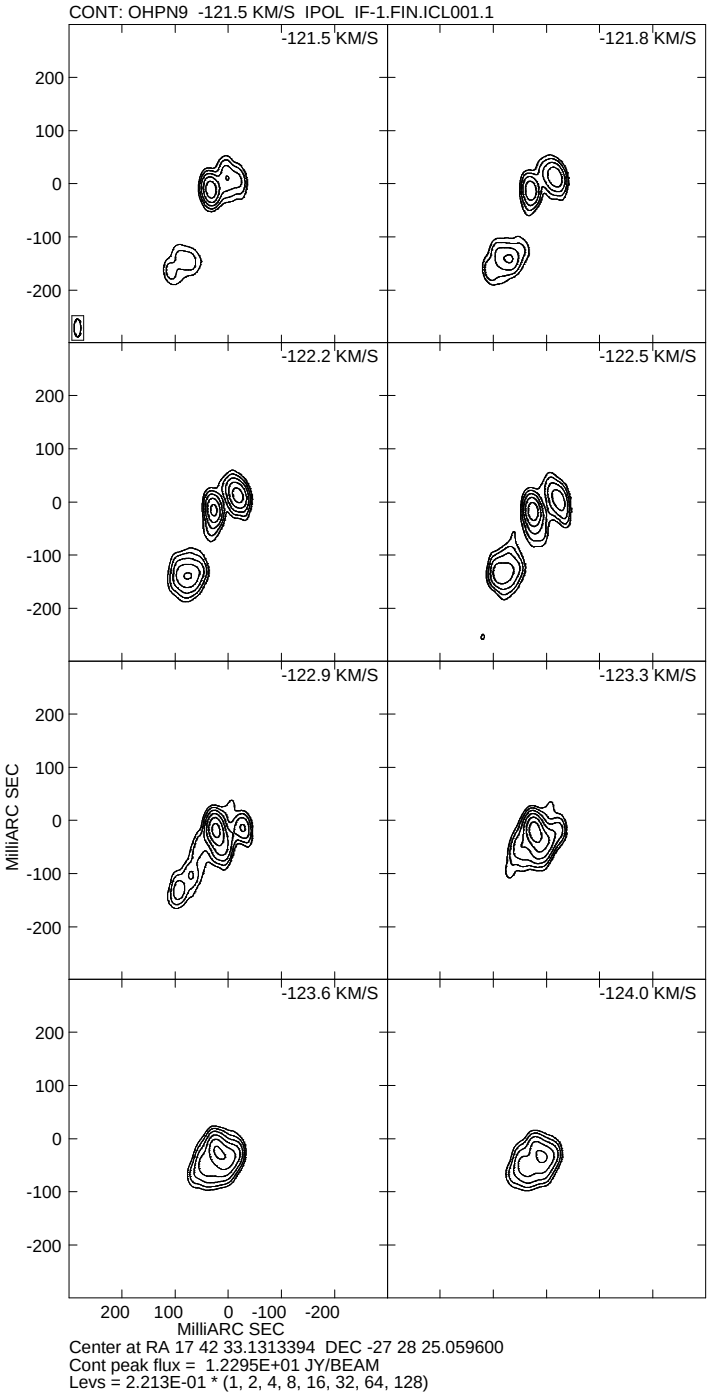

Figure 5.4: Contour maps of the Stokes I emission of the blue-shifted emission from OH 0.9+1.3.

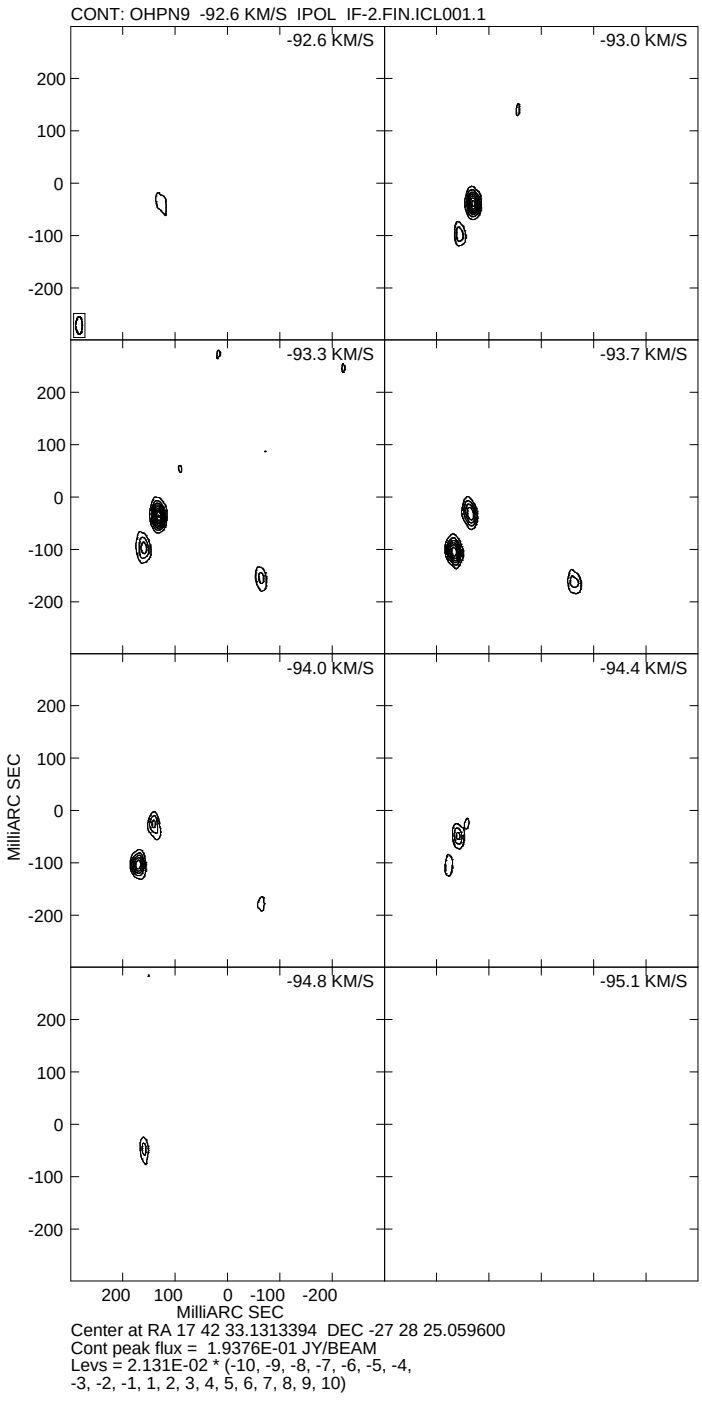

Figure 5.5: Contour maps of the Stokes I emission of the red-shifted emission from OH 0.9+1.3.

Method	$\Delta\alpha$ (mas)	$\Delta\delta$ (mas)
Blue-shifted	10.3	-36.3
Centroid	30.3	-47.5
Mid-point	53.0	-57.7
LSQ fit	3.6	-79.1

Table 5.2: Stellar position as offsets from the phase centre of the map.

of the methods outlined above is reliable for all cases (Nedoluha and Bowers, 1992).

VLBI astrometry of OH masers has revealed that in several sources the bright blue-shifted maser emission is co-incident with the stellar position and is thus amplifying the stellar continuum emission (Vlemmings et al., 2003). In light of these observations the position of the brightest blue-shifted component is listed as a possible stellar position in table 5.2, along with the stellar positions obtained via the other three suggested methods. It is clear that these four methods yield quite widely varying results.

5.6 Expanding shell model

The simple uniformly expanding shell model proposed by Reid et al. (1977) is easy to understand in terms of its expected behaviour in a maser map. Since maser intensity increases when the absolute rate of change of velocity along the line of sight decreases, the emission associated with this model will be strongest at two small caps at the front and the back of the star. The maser components which are Doppler shifted to the extreme edges of the spectrum originate from these caps which are directly in front of, or behind the star in the shell. Maser emission from intermediate concentric shell radii will occur in projected circular shells whose radii increase as the line-of-sight velocity of the emission approaches the stellar velocity. Thus the expected radial distance from the stellar position is larger at the centre of the spectrum. For an infinitely thin shell with radius R, the expected radial displacement θ of

the maser components at Doppler velocity v is given by (Reid et al., 1977):

$$\theta = R\sqrt{1 - \frac{(v - v_*)^2}{v_{exp}^2}} \tag{5.9}$$

Here v_{exp} is the expansion velocity of the envelope and v_* is the stellar velocity with respect to the local standard of rest. This thin shell model is an idealisation and many observed circumstellar masers distributions are not adequately described by it. The original proponents of this model (Reid et al., 1977) highlighted two possible scenarios whereby an AGB star might depart from this idealised case. The first of these is that the circumstellar shell may not be homogeneous. Such inhomogeneities may explain the apparent preference for masers to form in localised spots rather than the predicted ring-like structures. Secondly CSE's may not be ejected in a continuous and uniform manner but are ejected episodically. Thus the OH masers may arise from a series of circumstellar shells each with a slightly different velocity. In this case the OH masers would still be confined to a region much smaller than the diameter of the shell but would distributed in a more random fashion.

In order to determine whether the emission from OH 0.9+1.3 is consistent with the thin shell model, a least-squares fit of this model to the component data was performed. This fit was performed for each of the four inferred stellar positions in table 5.2. Plots of these fits are given in figure 5.6 and the estimates of stellar velocity, expansion velocity and shell size obtained from the fitting procedure is given in table 5.3. These parameters don't appear to be particularly sensitive to the choice of stellar position and are consistent with previous estimates obtained by Shepherd et al. (1990) using the MERLIN array. The stellar velocity also agrees well with the -107 km.s^{-1} estimated from CO observations by Mauersberger et al. (1988).

Although the red-shifted emission appears to be reasonably shell-like in these plots the more powerful blue-shifted emission is not. Observations of this source by Shepherd et al. (1990) also indicated that the blue-shifted emission was not particularly well modelled as a thin shell and suggested that some of this emission may instead be associated with the disruption of the

Method	R (mas)	V_{exp} (km.s^{-1})	V_* (km.s^{-1})	Nebular Size ($\times 10^{14}$ m)
Blue-shifted	248	15.92	-107.0	2.93
Centroid	218	16.13	-107.1	2.58
Mid-point	220	15.97	-107.5	2.60
LSQ fit	187	17.89	-106.2	2.21

Table 5.3: Results of a least-squares fit of an expanding shell model to the maser components. The method column indicates the inferred stellar position used in the fit.

inner parts of the molecular envelope by stellar ultraviolet radiation or by a fast stellar wind. It is certainly feasible that the envelope of this transitional object is undergoing some degree of disruption however the emission from these observations may also possibly be interpreted in a more conventional manner as arising from a thick expanding shell.

It is also possible that the brighter emission in this object arises from a compact inner shell physically distinct from the outer expanding shell where most of the weaker maser emission arises. This possibility is most attractive if the brighter emission is amplifying a central radio source as such a maser turns on much faster than masers in the outer circumstellar envelope and is therefore likely to be located closer to the central star. The plots in figure 5.6 indicate that if this is the case then these two shells must have similar expansion velocities as the brighter emission does not occur at a distinct velocity. The plots in figure 5.6 cannot provide conclusive support for such a scenario. Thus in the absence of further compelling evidence in favour of two physically distinct emitting regions the simplest explanation for the source emission profile is that it arises from a single expanding shell.

When considering the fits in figure 5.6 it is useful to note that the red-shifted emission should be absent at the location of the central radio source as the emission will be attenuated by this source. Thus there should be a gap in the emission at the extreme velocity of the red-shifted emission located immediately behind the blue-shifted peak. This phenomenon is visible in all

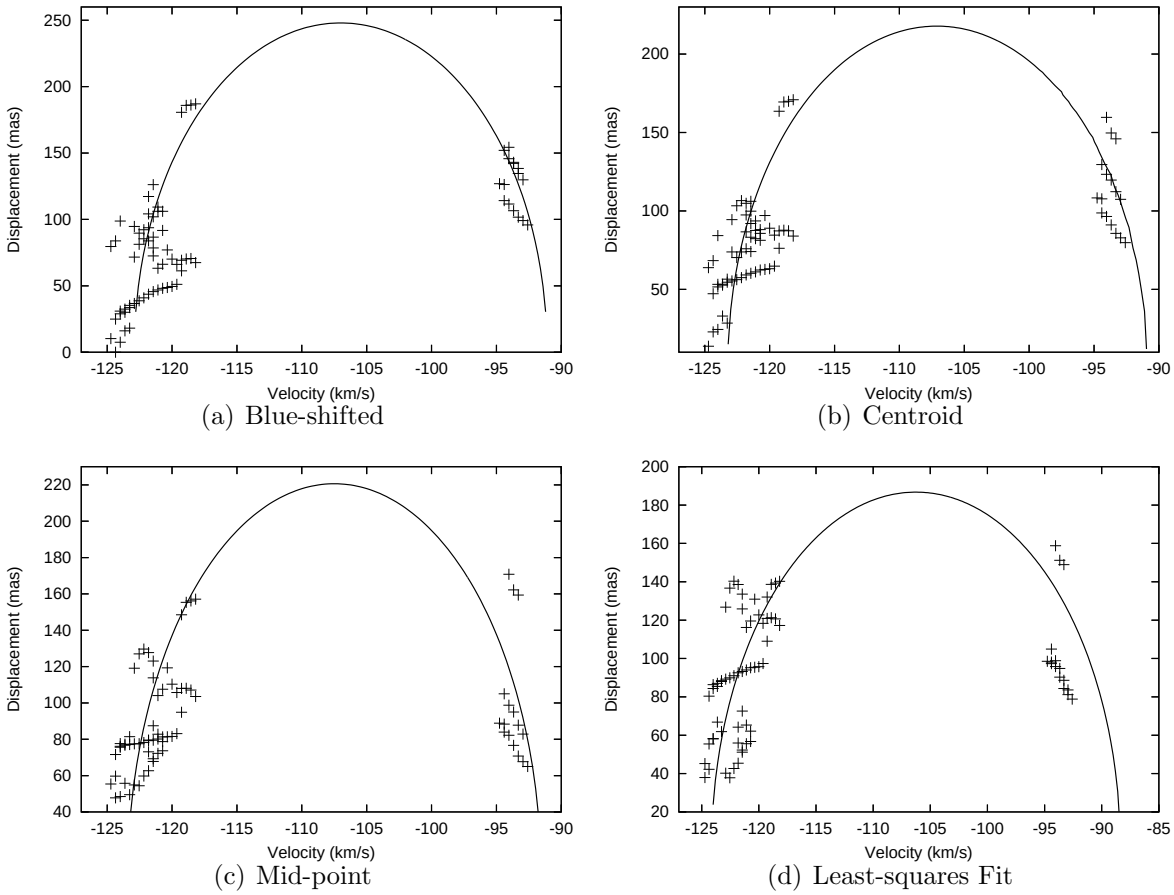

Figure 5.6: An expanding shell model fit to the maser components for four different assumed stellar position. The x-axis is velocity and the y-axis is radial displacement from the stellar position. The fitted expanding shell model is indicated by the solid line.

of the plots except plot (c) in figure 5.6. Thus it would seem that scenario (c) can be deemed the least likely of the four proposed stellar positions.

5.7 Bipolar outflows

Bipolar fast stellar winds and collimated jets are frequently cited as promising mechanisms for producing asymmetric structure in planetary nebulae. Masers provide observers with an important probe of the kinematics of these environments and H_2O masers have been observed to trace high velocity

outflows in shocked regions of the so-called 'water fountain' nebulae. Observations of OH maser emission in several proto-planetary nebulae and post-AGB stars have also been suggestive of a bipolar outflow. These include OH 37.1-0.8 (Gómez and Rodríguez, 2000) and IRAS 16342-3814 (Sahai et al., 1999).

Objects with irregular OH emission profiles which extend over a larger velocity range than is typical for AGB stars (> 50 km.s^{-1}) are often assumed to be more likely to be associated with a fast stellar wind or bipolar outflow (Zijlstra et al., 2001). However this is not a pre-requisite for the presence of bipolar structure as the OH masers of OH 37.1-0.8 exhibit the typical double-peaked 1612 MHz profile and yet have a clear bipolar spatial distribution. It is interesting to note that it has been suggested that OH masers and H_2O masers trace bipolarity in different parts of the envelope in these two sources. In both OH 37.1-0.8 and IRAS 16342-3814 the velocity range of the H_2O emission is much larger than that of the OH emission. It has been proposed that this phenomenon occurs because the H_2O masers arise in the poles of the wind as a result of shock excitation whereas the OH emission probably comes from a lower latitude region (Gómez and Rodríguez, 2000).

In light of the potentially significant role of such outflows, and the previous detection of bipolar structure in a proto-planetary nebula with a double-peaked spectral profile, the maser components of OH 0.9+1.3 were examined for any sign of a bipolar outflow. Depending on the angle of inclination of such an outflow one would expect that the maser emission would be aligned along a linear axis and that the blue- and red-shifted emission would be located on opposite ends of this axis. The plot in figure 5.7 provides convincing evidence that this is not the case for OH 0.9+1.3.

A further mechanism whereby one might discern the presence of a bipolar flow is by examining the radial displacement versus velocity plots of the maser components. Zijlstra et al. (2001) investigate the development of bipolar flows during post-AGB evolution. Their paper models the interaction of a slow outer wind with a fast inner wind with either of these two winds being non-spherically symmetric. The predicted velocity radius relation for the model of an hourglass shaped bipolar outflow is given in figure 5.8. The

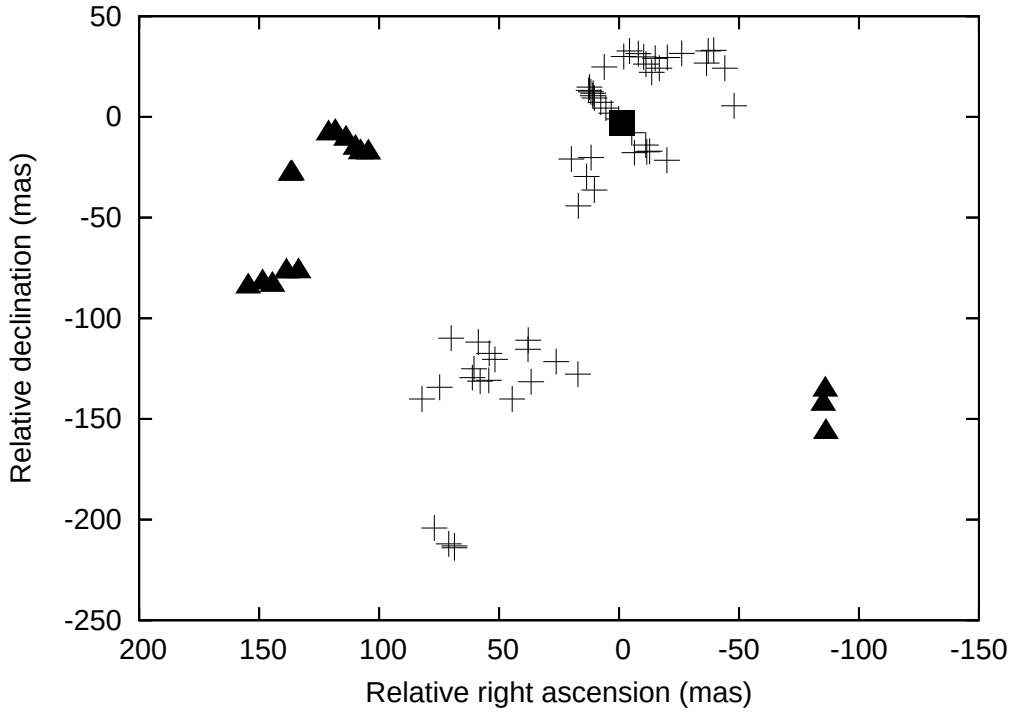

Figure 5.7: Plot of the position of the maser components relative to the map centre. The blue-shifted maser components are represented as the crosses and the red-shifted components are the filled triangles. The strongest blue-shifted maser component is represented by the filled square.

elliptical distribution of points arises from the remnant AGB shell and the linear radial features arise from the bipolar outflow. They reported linear features of this type in several post-AGB objects including OH231.8+4.2 and IRAS 11385-5517. There is no clear evidence of such linear features in the velocity-radius plots in figure 5.6 nor is there any evidence of maser emission whose velocity increases with distance from the star as would be expected in the case of a linear outflow from the star.

Another model of OH emission from a bipolar nebula was proposed in Chapman (1988). In this model the OH masers are located in two rings of uniform width on the front and back of expanding cones. The predicted spectral profile from the tilted rings has two double-peaks symmetrically placed about the stellar velocity. It is clear that the spectral profile of OH 0.9+1.3 is not consistent with this prediction. Thus the final conclusion of this section is that there is no evidence of an orderly bipolar outflow in the OH emission of this source. However this does not rule out the possibility that the overall morphology of this object is axisymmetrical as there are objects with a spherical OH maser shell whose reflection nebulae are bipolar, e.g., IRAS 17150-3224 (Hu et al., 1993).

5.8 Disks or torii

OH masers in several proto-planetary nebulae have been identified as emanating from an expanding disc or torus. These objects include OH 231.8+4.2 (Morris et al., 1982), M1-92 (Seaquist et al., 1991), and the young planetary nebula K3-35 (Gómez et al., 2006). In K3-35 the 1665 MHz OH maser emission is confined to a small band at the equator whose orientation is perpendicular to the bipolar outflow of the nebula. Interferometric maps indicate that there is some evidence of orbital rotation in these masers and that they are circularly polarised suggesting the action of a magnetic field (Gómez et al., 2006). It has been suggested that this magnetised disk is responsible for driving bipolar outflows in this nebula. The 1667 MHz OH masers of M1-92 are also situated in a torus structure which is parallel to the bipolar outflow of the source (Seaquist et al., 1991).

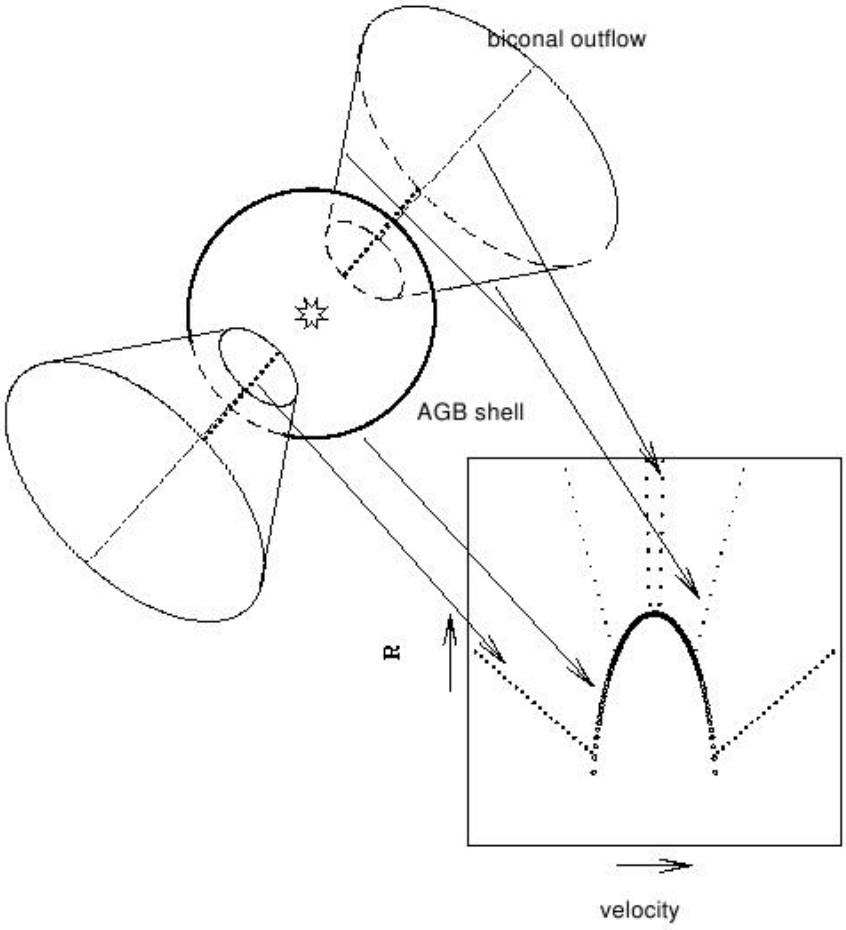

Figure 5.8: Predicted velocity radius relations for a bipolar outflow from Zijlstra et al. (2001). The geometric model consists of a remnant spherical AGB shell and a symmetric biconical outflow.

Examining the OH emission from OH 0.9+1.3 there are several reasons for rejecting the torus or disk-like structures that characterise the sources described above. The first is that Reid et al. (1977) have already established that in order for a rotating disk to produce the typical double-peaked profile of an OH/IR star, an unrealistically high stellar mass must be assumed. The second is that the OH spectral profiles of all stars that have been identified as expanding, rotating disks differ considerably from the double-peaked profile exhibited by OH 0.9+1.3. These sources have a single irregularly shaped emission feature which extends over a large velocity range (between 20 and 40 km.s^{-1}). Finally in the case of a disk-like emission one would expect to see that the maser emission is confined to a narrow equatorial band and that the blue- and red-shifted emission would be located at opposite ends of this band. An examination of figure 5.7 reveals that this is patently not the case for this source.

5.9 Polarisation

Polarised emission above the detection thresholds was measured in the eight strongest maser features of the blue-shifted emission and in only one of the red-shifted features. Upon examining table 5.1 it is clear that all of the polarised features were elliptically polarised with the exception of feature 11_B which was purely linearly polarised. In all cases the percentages of linear and circular polarisation were small, with average values of $m_l = 5.54\%$ and $m_c = 7.11\%$ while the maxima are $m_l = 20.0\%$ and $m_c = 23.4\%$. The maximum total percentage polarisation $m_T = \sqrt{m_l^2 + m_c^2}$ was 30.8%. The maximum percentage circular and linear polarisation was detected in feature 1_B which is centred at a velocity of -118.91 km.s^{-1}. In a survey of the polarisation properties of 47 proto-planetary nebulae Szymczak and Gérard (2004) concluded that the percentage polarisation in these objects is usually less than 15%. Thus with the exception of feature $1B$ the polarised emission in OH 0.9+1.3 is well within the expected range for a proto-planetary nebula. It is clear from examining table 5.1 that the maser components are predominantely negatively circularly polarised.

There is some evidence that the polarisation properties of this source have varied considerably over the last decade. More recent observations with the Nançay Radio Telescope (NRT), made in 2003 by Szymczak and Gérard (2004), determined the maximum linear and circularly polarised feature in this source and these features are not coincident with the maximally polarised feature in the observations presented in this thesis. The NRT measurements determined the maximum linear and circularly polarised features to be at -123.5 and -120.5 km.s^{-1} respectively. It is possible that these changes in the polarisation properties of the source are related to missing flux in the final source image caused by the lack of short and intermediate baselines in the VLBA. However a comparison of figures 5.1 and 5.2 reveal that although the final source image recovers only 70% of the source flux all four of the source emission components are recovered. Furthermore the relative strengths of these emission features are approximately maintained in the final source image. Therefore it would appear that each component is affected approximately equally by the phenomenon of lost flux and this effect should not result in a significant change in the observed polarisation properties of the source. The plots in figure 5.1 also clearly reveal that the component at -119 km.s^{-1} is significantly more polarised than the other three spectral components in these observations. Thus it seems likely that this variability of the source polarisation properties is a real effect.

The polarisation morphology of the source is shown in figure 5.10 Here the linear polarisation vectors are superimposed on a contour map of the total intensity, the orientation of the vectors show the orientation of the electric field vector and the length of the vectors is proportional to the linearly polarised intensity. The polarisation angle changes from $\sim 120^\circ$ at -124 km.s^{-1} to $\sim 2^\circ$ at 119 km.s^{-1}. This represents a large change in polarisation angle over the velocity range of the blue-shifted emission. Szymczak and Gérard (2004) also noted a change in the polarisation angle of approximately 120° in the blue-shifted emission of this source and speculated that such a large change might be indicative of complex magnetic field structure.

It is important to note that Faraday rotation in the intervening interstellar medium can rotate the plane of the source polarisation vectors. However the

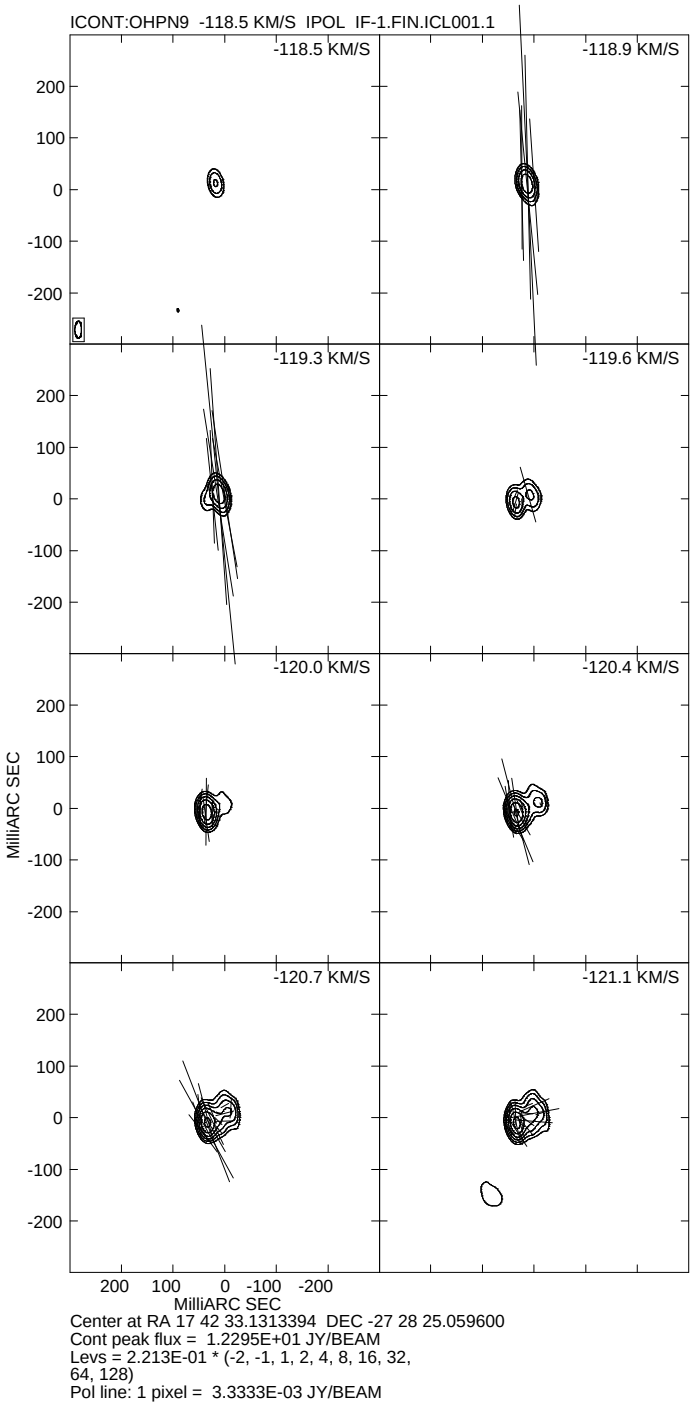

Figure 5.9: The distribution of linearly polarised emission. The orientation of the vectors show the electric field vector and the length is proportional to the linearly polarised intensity. The contours show the distribution of the Stokes I emission.

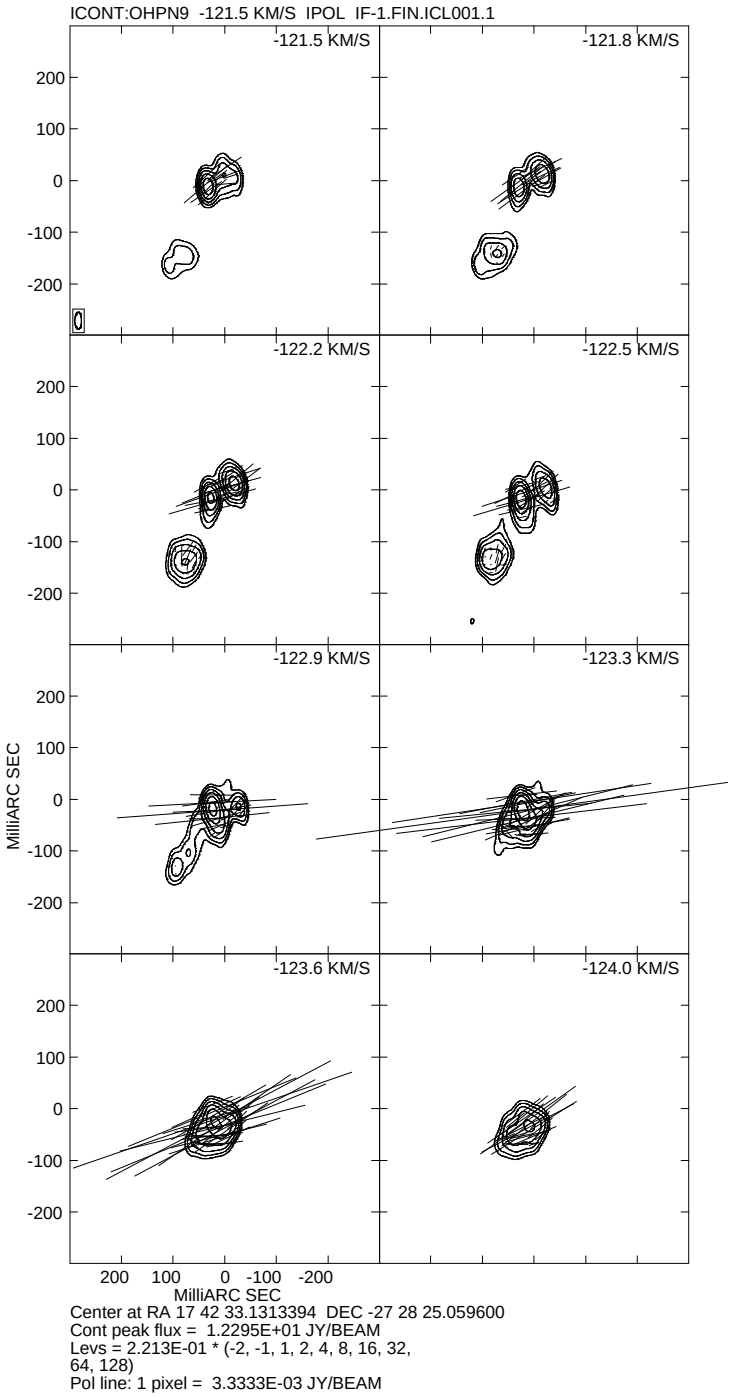

Figure 5.10: The distribution of linearly polarised emission. The orientation of the vectors show the electric field vector and the length is proportional to the linearly polarised intensity. The contours show the distribution of the Stokes I emission.

small size of OH 0.9+1.3 means that the Faraday rotation will affect all the polarisation vectors equally and thus the relative positions of the polarisation vectors will be preserved but with an overall rotation.

The polarisation angle, θ_p, is expected to remain fairly constant or vary smoothly with frequency across individual maser features (Bains et al., 2003). However inspection of figures 5.10 and 5.9 indicates that in feature 3_B the polarisation angle changes rather abruptly at -121.45 km.s^{-1} by approximately 90 degrees. This anomaly may result from localised perturbations in the magnetic and/or velocity field structure of the source. Vlemmings et al. (2006) noted a similar phenomenon in a bright H_2O maser feature in W43A and interpreted this as indicating that the linear polarisation vector changes its relative orientation from parallel to perpendicular with respect to the magnetic field across the maser feature. It is also possible that the VLBA beam size is unable to resolve the maser clouds fully so that features of similar velocities are spatially blended along the line of sight.

5.10 Depolarisation

Szymczak and Gérard (2004) reported evidence of a reduced degree of polarisation in bright Stokes I features in OH 0.9+1.3. These observations were performed with the NRT with a spectral resolution of at least 0.14 km.s^{-1}. This trend was observed in two other sources and was observed in both the linear and circular polarised emission of OH 0.9+1.3. In order to determine whether this trend is visible in the VLBA observations the fractional polarisation of the total integrated flux in each channel of the final deconvolved image was determined. The percentage circular and linear polarised flux was then plotted against the total Stokes I intensity in the channel. Similarly the percentage polarisation of each maser component was plotted against its maximum intensity. No clear evidence of a depolarisation trend was observed in these plots, however these observations were performed at a lower spectral resolution than the NRT observations. The NRT observations detected polarised emission in over 30 channels whereas the VLBA observations only detected emission in 20 channels. It is thus possible that the

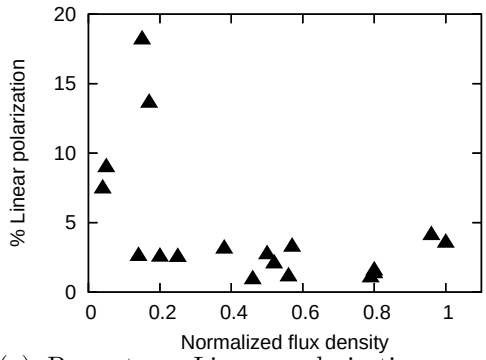

(a) Percentage Linear polarisation versus normalised intensity in each channel of the deconvolved images

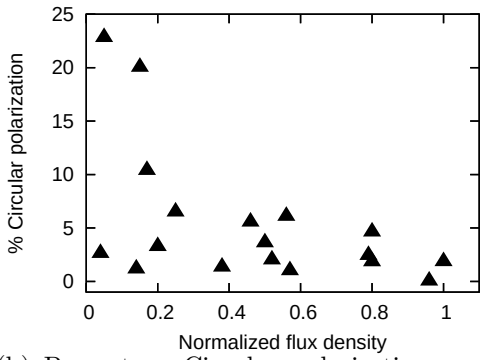

(b) Percentage Circular polarisation versus Normalised Intensity in each channel of the deconvolved images

Figure 5.11: Polarisation versus normalised intensity.

polarised emission is detected in too few channels to meaningfully imply such a depolarisation trend.

5.11 Magnetic field

Polarised maser emission provides some of the most convincing evidence to date of the presence of stellar magnetic fields in post-AGB stars. Maser polarisation measurements can also be of considerable use in establishing the morphology and magnitude of such fields. Polarised emission from OH masers has been detected in several proto-planetary nebula candidates and in some cases has been used to infer magnetic field strengths in these objects (Szymczak and Gérard, 2004; Bains et al., 2004, 2003). These measurements yield estimates of between 1 and 3 mG for the magnetic field strength at the OH emitting radius. As many promising models detailing the morphological evolution of late-type stars invoke the role of stellar magnetic fields it is useful to examine the polarisation data of OH 0.9+1.3 in order to establish whether such fields may be actively shaping this PPN. The presence of stellar magnetic fields is inferred by interpreting the circularly polarised emission from the source as arising from the Zeeman effect, thus for completeness a brief introduction to this effect is given in the next section.

5.11.1 Zeeman effect

OH is an open shell molecule with net electronic angular momentum and thus has paramagnetic properties. In a paramagnetic molecule each unit of angular momentum gives rise to a magnetic moment, the Bohr magneton, $\mu_B = \frac{e\hbar}{2M_e c}$. In this expression e is the the electron charge, $\hbar$ the Planck constant, c the speed of light and m_e is the electron mass. Each molecular level with overall angular momentum J contains 2J+1 magnetic sub-states characterised by the magnetic quantum number m. In the absence of a magnetic field all these sub-states have the same energy. This degeneracy is lifted by the introduction of an external magnetic field which causes the energy of a level with total quantum number F to split into 2F+1 levels, each with energy given by:

$$E_0 + B\mu_B g_F m_F \tag{5.10}$$

Here E_0 is the energy in zero field, m_F is the magnetic quantum number and takes the values -J,-(J-1)...(J-1),J, and g_F is the Lande splitting factor.

Transitions may now occur between the magnetic sub-states m_2 and m_1 of an upper state 2 and a lower state 1 with angular momenta J_2 and J_1 respectively. Thus the original single spectral line splits into a number of Zeeman components whose line frequencies are given by:

$$\nu(m_2, m_1) = \nu_{21} + B(\mu_B g_2 m_2 - \mu_B g_1 m_1) \tag{5.11}$$

The selection rule for electric dipole radiation is $\Delta m_F = 0$ or ± 1. Lines generated in $\Delta m = -1$ and $+1$ transitions are called $\sigma^-$and σ^+-components and these transitions generate left- and right-circularly polarised emission respectively in the plane perpendicular to the magnetic field. For propagation at an oblique angle to the magnetic field the circle is viewed in projection and the polarisation if the emission in that direction is elliptical. The ratio of the semi-major to semi-minor axis of the polarisation ellipse is given by $\cos\psi$ where ψ is the angle between the magnetic field and the line of sight. Lines generated in $\Delta m = 0$ transitions are called π-components. These lines are linearly polarised parallel to the projected magnetic field and are zero for

$\psi = 0$.

5.11.2 Maser polarisation theory

The propagation of an underlying Zeeman pattern along a maser amplification path differs from the thermal case due to the intrinsic stimulated emission process. The transport of polarised maser emission is a complex problem influenced by many parameters including the degree of saturation, the relaxation rate, Faraday rotation and the presence or absence of a magnetic field along the maser path (Kemball, 2002). The details of this process are outlined in Goldreich et al. (1973); Elitzur (1992) and Deguchi and Watson (1986) which construct the density matrix evolution and the maser radiation transfer equations including Zeeman terms. Observed maser polarisation information may be expressed in terms of the electric vector position angle χ and the fractional linear, m_l, and circular, m_c, polarisation of the emission. In general, m_c can be used to estimate the magnitude of the magnetic field and χ is used to infer the projected magnetic field orientation with respect to the line of sight (Kemball, 2002).

An important parameter which defines the degree to which magnetic transitions overlap in frequency is the splitting ratio $r_z = \frac{\Delta\nu_z}{\Delta\nu_D}$ where $\Delta\nu_z$ is the Zeeman splitting width and $\Delta\nu_D$ is the Doppler line-width. In the case of large splitting, $r_z > 1$, the individual Zeeman components are resolved and should be clearly identifiable as separate components in the emission spectra. In this case there are no theoretical ambiguities and the magnitude of the magnetic field can be deduced from the velocity shift of the Zeeman components.

In the alternative scenario, the small splitting case, $r_z < 1$, the Zeeman components significantly overlap in frequency and the Stokes V emission has a characteristic S-shaped profile which is formed by the addition of two offset Gaussian line profiles of opposite circular polarisation (Kemball, 2002). Polarised emission in the small splitting regime admits both a Zeeman and a non-Zeeman theoretical interpretation. In the Zeeman interpretation the magnitude of the magnetic field is proportional to the fractional circular

polarisation and its orientation is either parallel or perpendicular to the projected B field depending on whether the viewing angle θ is $<$ or $>$ 55° (Elitzur, 1992). In the small splitting case the component separation can be estimated using the approximation given by Troland and Heiles (1982):

$$V(\nu) = \alpha \frac{dI(\nu)}{d\nu} + \beta I(\nu), \tag{5.12}$$

where α is the splitting factor and β accounts for differential amplitude gain between polarisations. A detailed statistical analysis of this estimation technique is outlined in Sault et al. (1990) which finds that the technique is applicable when $r_z < 0.1$ and there are more than ten samples per line-width across the profile. In stellar OH masers the Zeeman splitting is intermediate with a splitting ratio $r_z \sim 1$.

The Stokes V maps were examined in order to identify possible Zeeman pairs. These maps are presented in figures 5.12 and 5.13. Further Zeeman analysis was carried out with the MIRIAD task Zeemap. This task attempts to measure the line shift due the Zeeman effect by fitting the derivative of the intensity map to the Stokes V map as given in equation 5.12. The Zeemap task did not detect any Zeeman pairs. The absence of a Zeeman pair in the circular polarisation maps prevented an estimation of magnetic field strength and any subsequent determination of the relative dynamical influence of such a field on this PPNe.

The absence of Zeeman pairs in OH maser polarisation maps is not an unusual phenomenon, indeed most observed circularly polarised features cannot be interpreted as a Zeeman pair (Nedoluha and Watson, 1990). In many cases where spatially coincident pairs are identified they do not conform with the expected theoretical line ratios and intensities. The pairs are frequently asymmetric in velocity or incompletely formed. This could be intrinsic to the polarisation mechanism or could be caused by inhomogeneities in the local masing conditions of each Zeeman component (Kemball, 2002). Velocity gradients have been proposed as one mechanism which may preferentially amplify or suppress one half of a Zeeman pair and their effect on maser polarisation has been considered at some length by Nedoluha and Watson (1990)

and Deguchi and Watson (1986).

In the case of OH 0.9+1.3 it has been speculated that velocity gradients may be partially responsible for creating multiple peaks in the blue-shifted emission of the source (Zijlstra et al., 1989). This suggestion is based on theoretical work by Nedoluha and Watson (1988) which suggests that velocity gradients may cause a single spectral line to split into several narrow components. An initial inspection of the data suggested that there was some evidence of a velocity gradient in features 3_B and 9_B. The spectrum of this region of the map indicates that there are two spectral features within 12 milliarcseconds of each other and this is consistent with the predicted line splitting. In order to characterise this velocity gradient a linear relation was fitted to the location of the two maser features. A χ^2 minimisation found the best-fit line through the components to have a P.A. of $\sim 40°$. Thereafter the maser velocity was plotted as a function of projected distance along this fitted positional axis. The plot of velocity versus projected distance along the linear axis is shown in figure 5.14. There is an obvious trend implying a monotonic change in velocity across these two maser features, however the slope of this velocity gradient is quite different across the components in each maser feature. If this velocity gradient is indeed representative of the source dynamics it may be partially responsible for the paucity of identifiable Zeeman pairs in the source. However such an observed velocity gradient may not reflect the actual dynamics of the source as velocity gradients can easily be caused by projection effects (Kemball, 1992).

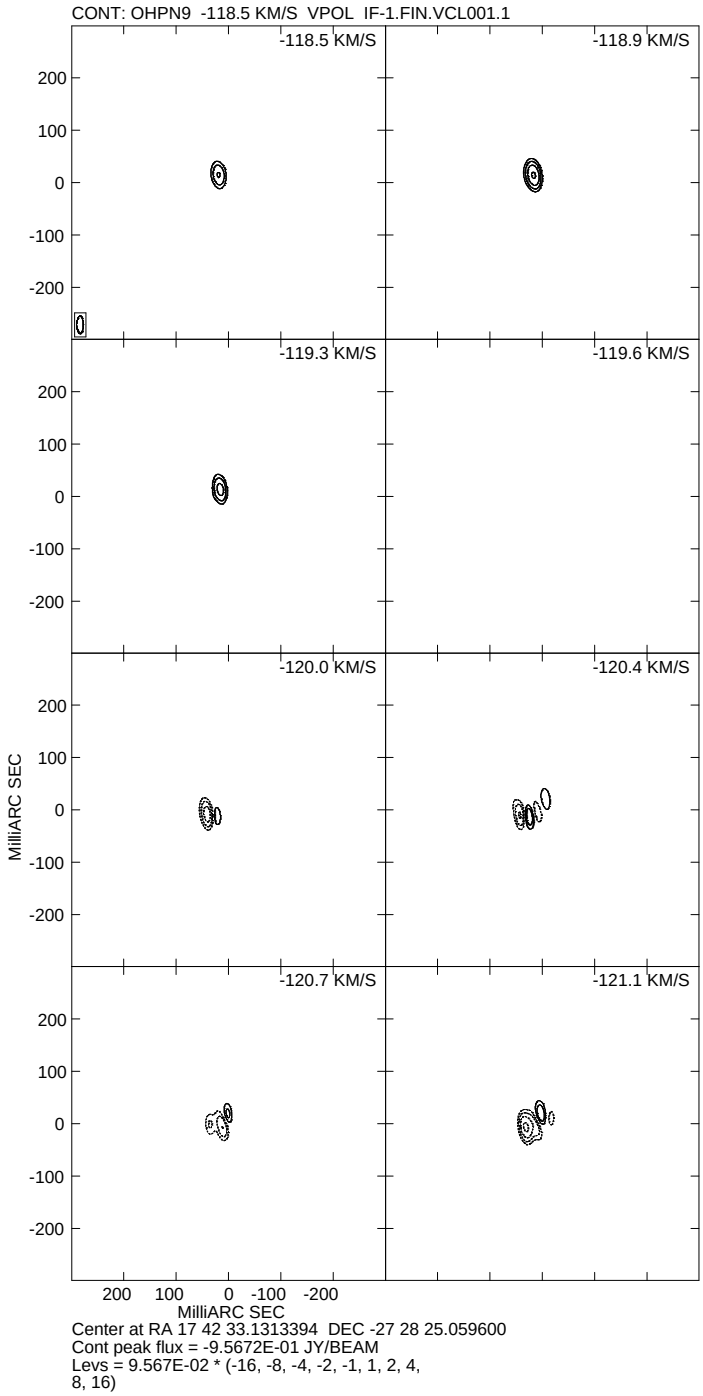

Figure 5.12: Contour maps of Stokes V emission.

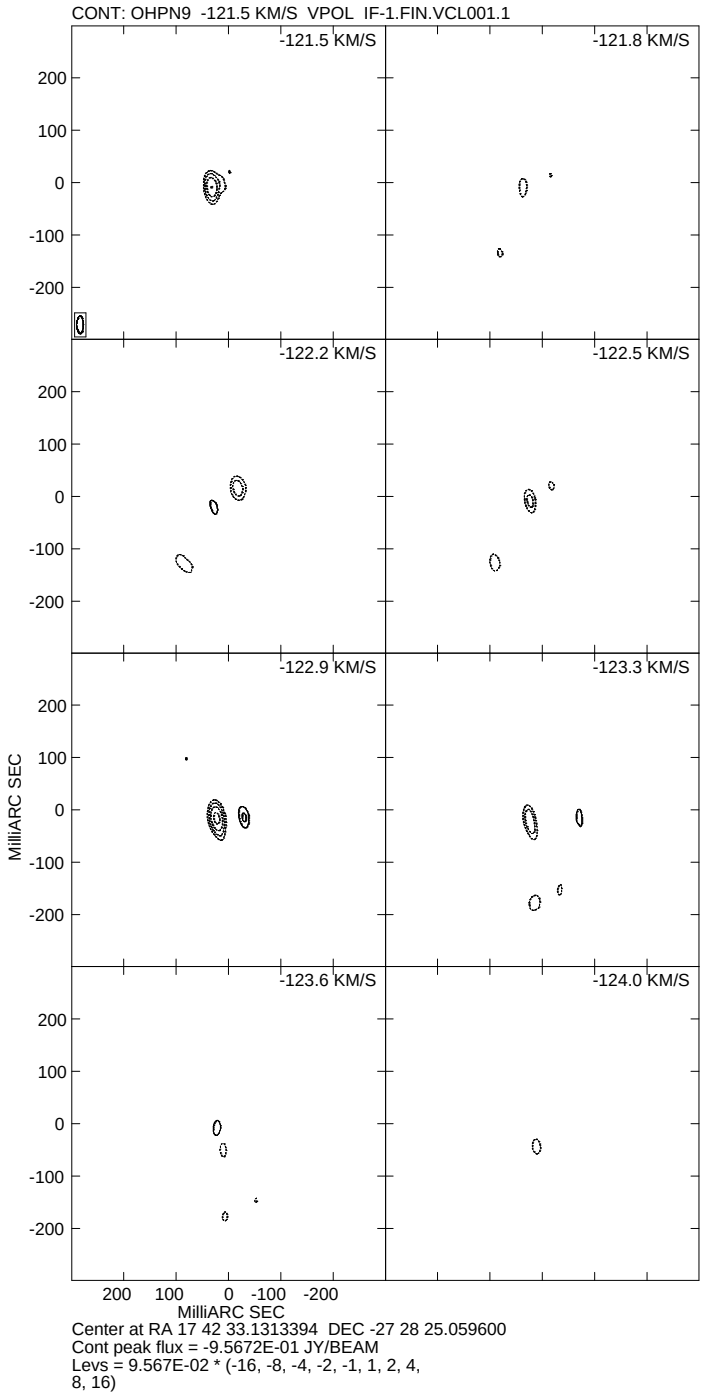

Figure 5.13: Contour maps of Stokes V emission.

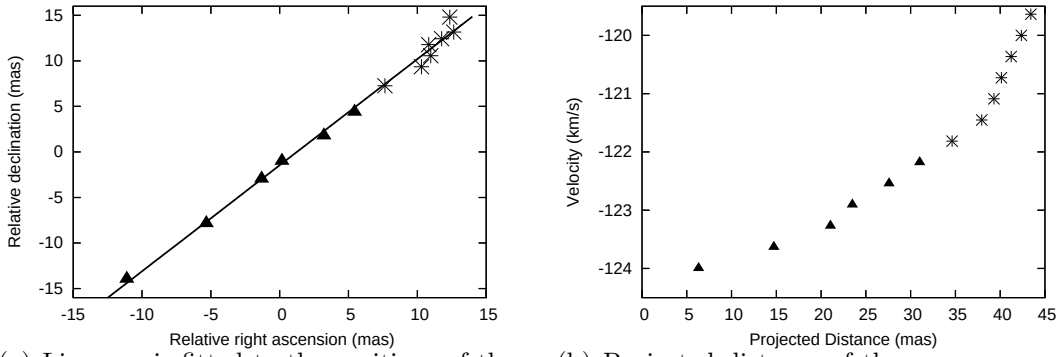

(a) Linear axis fitted to the positions of the maser components.

(b) Projected distance of the maser components versus velocity.

Figure 5.14: The triangles represent maser components from feature 9_B while the stars represent components from feature 3_B. In the left-hand figure the points represent the maser positions and the line is the best-fit positional axis to those points. The projected distance of the maser components relative to this line is plotted versus velocity in the figure on the right hand side. In the right hand figure it is clear that the velocity of the maser components changes monotonically with projected distance

Chapter 6

Conclusion

6.1 Synopsis of results

This thesis reports the production of VLBI synthesis maps of 1612 MHz OH maser emission from the PPNe candidate OH 0.9+1.3. PPNe are relatively short-lived objects that bridge the evolutionary gap between the largely spherical post-AGB stars and fully fledged PN that exhibit a wide variety of axisymmetric structure. The synthesis maps produced in this thesis are the first full-polarisation VLBI maps of this source. These maps were used to investigate the morphology and kinematics of this unusual transitional object at VLBI resolution. The total intensity maser maps were found to exhibit a considerable degree of asymmetry with the blue- and red-shifted maser emission located in spatially distinct regions of the envelope. This is in sharp contrast with the circularly symmetric ring-like structures which are typically observed in their evolutionary predecessors, OH/IR stars. OH/IR stars exhibit double-peaked OH maser emission consistent with a thin-shell morphology in a large fraction of cases, $> 85\%$ (Sevenster et al., 1997; Deacon et al., 2004). Thus the highly asymmetric spatial structure of this source argues strongly in favour of its status as a proto-planetary nebula.

An attempt was made to fit the standard OH/IR kinematic model of a simple expanding shell to the maser components. This model was a poor fit to the strong blue-shifted emission from this source but was a reasonable

approximation of the more ring-like red-shifted emission. The fit was performed using four different estimates of the stellar position which all yielded broadly similar estimates for the stellar velocity, the envelope expansion velocity and size of the envelope. The average of these four estimates was -107 km.s^{-1} for the stellar velocity, 16.47 km.s^{-1} for the expansion velocity, and 218 milliarcseconds for the envelope radius.

Bipolar outflows and jets are believed to be instrumental in creating axisymmetric structure in circumstellar envelopes. Thus the data was compared with a model of a bipolar outflow generated by a wind-wind interaction in a post-AGB star (Zijlstra et al., 2001). Analysis of the kinematics of this source did not reproduce the diagnostic features predicted by the bipolar outflow model and no other evidence of a bipolar outflow was detected in the source structure.

The source was imaged in all four Stokes parameters and the fractional linear and circular polarisation of the maser components was derived from the Stokes Q, U and V images. Polarised emission was detected from the eight strongest maser components in the blue-shifted emission and in only one component in the red-shifted emission. The maximum fractional linear polarisation, 20.0%, was detected at the same component with the maximum fractional circular polarisation, 23.4%. In all other components the detected level of polarised emission was small with an average linear polarisation of 5.54% and an average circular polarisation of 7.11%.

In a survey of 47 PPN candidates Szymczak and Gérard (2004) detected circularly polarised emission at 1612 MHz from about 80% of the targets. In the past circularly polarised emission has not typically been detected in OH/IR stars (Zijlstra et al., 1989), in this case the detection of several circularly polarised maser components towards OH 0.9+1.3 would provide further confirmation of its PPN status. However, in a paper by Zell and Fix (1991) circularly polarised emission was measured towards several OH/IR stars using the Arecibo telescope. This leads Szymczak and Gérard (2004) to conclude that insufficient sensitivity was the primary factor contributing to the previous non-detection of circular polarisation in these objects. If this is the case then circular polarisation may not provide a conclusive indicator

of evolutionary status.

The polarisation structure of the source appears to have changed over the period of 10 years between the observations reported in this thesis and those presented by Szymczak and Gérard (2004), although it retains the feature of a large variation in polarisation angle across the spectral profile of the emission. Unfortunately the absence of a readily identifiable Zeeman pair in the circularly polarised emission prohibited an estimation of the magnetic field strength in this source.

6.2 Future work

Observations of PPNe offer a unique opportunity to gain insight into the mechanisms which are responsible for producing asymmetries in planetary nebulae. As with any astronomical object maximum insight into the morphology and dynamics of a source can be obtained by combining information obtained from several observational techniques. The localised nature of maser emission means that maps of single maser transitions are not necessarily representative of the global morphology of the source and kinematic models are limited in their ability to reconstruct the source dynamics from the angular distribution of maser components. It is therefore advisable to supplement the current single epoch 1612 MHz maser emission map with proper motion studies obtained from observations of the source at several epochs. This will provide far more definitive information about the source dynamics, and combined with information regarding the variability of the polarisation morphology may indicate whether the magnetic field has any direct impact on these dynamics.

In several late-type stars the 1665 MHz maser emission has been observed to be located closer to the central star than the 1612 and 1667 MHz emission; e.g., IRAS 18491-0207 and Roberts 22 (Zijlstra et al., 2001). It has also been noted that a significant fraction of post-AGB objects have 1667 MHz emission whose velocity range is larger than the velocity range of the 1612 MHz emission (Deacon et al., 2004). In K3-35 and IRAS 16342-3814 OH maser maps have shown that the different OH lines trace distinct regions of the

envelope (Miranda et al., 2001; Sahai et al., 1999). Thus there is some evidence that the OH main-line emission does not necessarily occur in the same region or probe the same kinematics as the OH satellite-line emission. In light of this evidence it may be useful to image the 1665 and 1667 MHz OH maser emission associated with OH 0.9+1.3 and attempt to establish the relative location of this maser emission with respect to the location of the satellite-line emission and the radio continuum emission.

As mentioned previously maser emission can only provide insight into the morphology of the very localised region in which they occur. Thus in order to obtain more information about the global properties of this object it might be useful to attempt to map the radio continuum emission associated with this maser source and also to attempt infra-red (IR) imaging of the circumstellar envelope.

Finally it is important to note that this work should be viewed within the larger context of trying to characterise the properties and kinematics of PPNe in general. Thus future work should include further observations of this class of object, and particularly further attempts to characterise the magnetic field structure and strengths in these objects. This is particularly important in light of the ongoing controversy surrounding the role of such fields in shaping the overall nebula.

Bibliography

Alcolea, J., Bujarrabal, V., Sánchez Contreras, C., Neri, R., Zweigle, J., 2001, Astronomy and Astrophysics, 373, 932

Bains, I., Gledhill, T. M., Yates, J. A., Richards, A. M. S., 2003, Monthly Notices of the Royal Astronomical Society, 338, 287

Bains, I., Richards, A. M. S., Gledhill, T. M., Yates, J. A., 2004, Monthly Notices of the Royal Astronomical Society, 354, 529

Balick, B., Alexander, J., Hajian, A. R., Terzian, Y., Perinotto, M., Patriarchi, P., 1998, Astronomical Journal, 116, 360

Balick, B., Frank, A., 2002, Annual Review of Astronomy and Astrophysics, 40, 439

Balick, B., Wilson, J., Hajian, A. R., 2001, Astronomical Journal, 121, 354

Bedijn, P., 1987, Astronomy and Astrophysics, 186, 136

Blackman, E. G., 2004, in M. Meixner, J. H. Kastner, B. Balick, and N. Soker (eds.), *ASP Conf. Ser. 313: Asymmetrical Planetary Nebulae III: Winds, Structure and the Thunderbird*, p. 401

Blackman, E. G., Frank, A., Markiel, J. A., Thomas, J. H., Van Horn, H. M., 2001a, Nature, 409, 485

Blackman, E. G., Frank, A., Welch, C., 2001b, The Astrophysical Journal, 546, 288

Blandford, R. D., Payne, D. G., 1982, Monthly Notices of the Royal Astronomical Society, 199, 883

Boboltz, D., 1997, *Ph.D. thesis*, Virginia Polytechnic Institute

Booth, R. S., Norris, R. P., Porter, N. D., Kus, A. J., 1981, Nature, 290, 382

Born, M., Wolf, E., 1980, *Principles of Optics: Electromagnetic Principles of Propagation,Inteference and Diffraction of Light*, Pergamon Press, 6 edition

Bowers, P. F., Johnston, K. J., Spencer, J. H., 1983, The Astrophysical Journal, 274, 733

Breitschwerdt, D., Kahn, F. D., 1990, Monthly Notices of the Royal Astronomical Society, 244, 521

Bronfman, L., Nyman, L.-A., May, J., 1996, Astronomy and Astrophysics Supplement Series, 115, 81

Brown, L., Roberts, B., Wardle, J., 1989, Astronomical Journal, 97, 1522

Bujarrabal, V., 1999, in T. Le Bertre, A. Lebre, and C. Waelkens (eds.), *IAU Symp. 191: Asymptotic Giant Branch Stars*, p. 363

Bujarrabal, V., Castro-Carrizo, A., Alcolea, J., Sánchez Contreras, C., 2001, Astronomy and Astrophysics, 377, 868

Castor, J. I., Abbott, D. C., Klein, R. I., 1975, The Astrophysical Journal, 195, 157

Chapman, J., 1988, Monthly Notices of the Royal Astronomical Society, 230, 415

Chapman, J., Cohen, R. J., Norris, R. P., Diamond, P. J., Booth, R. S., 1984, Monthly Notices of the Royal Astronomical Society, 207, 149

Chevalier, R. A., Luo, D., 1994, The Astrophysical Journal, 421, 225

Chiu, Y., 1975, Journal of Atmospheric and Terrestrial Physics, 37, 1563

Chu, Y.-H., Guerrero, M. A., Gruendl, R. A., Williams, R. M., Kaler, J. B., 2001, Astrophysical Journal Letters, 553, L69

Clark, B., 1989, in R. A. Perley, F. R. Schwab, and A. H. Bridle (eds.), *ASP Conf. Ser. 6: Synthesis Imaging in Radio Astronomy*, p. 1

Condon, J. J., 1997, Publications of the Astronomical Society of the Pacific, 109, 166

Contopoulos, J., 1995, The Astrophysical Journal, 450, 616

Conway, R., Kronberg, P., 1968, Monthly Notices of the Royal Astromical Society, 142, 11

Cook, A., 1977, *Celestial Masers*, Cambridge University Press

Cornwell, T., Braun, R., 1989, in R. A. Perley, F. R. Schwab, and A. H. Bridle (eds.), *ASP Conf. Ser. 6: Synthesis Imaging in Radio Astronomy*, p. 167

Cornwell, T., Fomalont, E., 1989, in R. A. Perley, F. R. Schwab, and A. H. Bridle (eds.), *ASP Conf. Ser. 6: Synthesis Imaging in Radio Astronomy*, p. 185

Cornwell, T. J., Wilkinson, P. N., 1981, Monthly Notices of the Royal Astronomical Society, 196, 1067

Cotton, W., 1993, Astronomical Journal, 106, 1241

Cotton, W., 1995, in J.A.Zensus, P. Diamond, and P. Napier (eds.), *ASP Conf. Ser. 82: Very Long Baseline Interferometry and the VLBA*, p. 289

Cotton, W. D., Geldzahler, B. J., Marcaide, J. M., Shapiro, I. I., Sanroma, M., Rius, A., 1984, The Astrophysical Journal, 286, 503

D'Addario, L., 1989, in R. A. Perley, F. R. Schwab, and A. H. Bridle (eds.), *ASP Conf. Ser. 6: Synthesis Imaging in Radio Astronomy*, p. 59

Deacon, R. M., Chapman, J. M., Green, A. J., 2004, The Astrophysical Journal Supplement Series, 155, 595

Deguchi, S., 1982, The Astrophysical Journal, 259, 634

Deguchi, S., Watson, W. D., 1986, The Astrophysical Journall, 300, L15

Diamond, P., 1989, in R. A. Perley, F. R. Schwab, and A. H. Bridle (eds.), *ASP Conf. Ser. 6: Synthesis Imaging in Radio Astronomy*, p. 379

Diamond, P. J., 1995, in J. A. Zensus, P. J. Diamond, and P. J. Napier (eds.), *ASP Conf. Ser. 82: Very Long Baseline Interferometry and the VLBA*, p. 227

Diamond, P. J., Norris, R. P., Rowland, P. R., Booth, R. S., Nyman, L.-A., 1985, Monthly Notices of the Royal Astronomical Society, 212, 1

Dijkstra, C., Speck, A. K., 2006, The Astrophysical Journal, 651, 288

Dorch, S. B. F., 2004, Astronomy and Astrophysics, 423, 1101

Elitzur, M., 1978, Astronomy and Astrophysics, 62, 305

Elitzur, M., 1992, *Astronomical Masers*, Kluwer Academic Publishers

Elitzur, M., Goldreich, P., Scoville, N., 1976, The Astrophysical Journal, 205, 384

Field, D., 1985, Monthly Notices of the Royal Astronomical Society, 217, 1

Fomalont, E., Wright, M., 1974, in G. Verschuur and K. Kellermann (eds.), *Galactic and Extragalactic Radio Astronomy*, p. 256, Springer, Berlin

Formalont, E., Perley, R., 1989, in R. A. Perley, F. R. Schwab, and A. H. Bridle (eds.), *ASP Conf. Ser. 6: Synthesis Imaging in Radio Astronomy*, p. 83

Frank, A., 1999, in J. Kastner, N. Soker, and S. Rappaport (eds.), *ASP Conf. Ser. 199: Assymetrical Planetary Nebulae II: From Origins to Microstructures*, Vol. 199, p. 225

Frank, A., 2004, in M. Meixner, J. H. Kastner, B. Balick, and N. Soker (eds.), *ASP Conf. Ser. 313: Asymmetrical Planetary Nebulae III: Winds, Structure and the Thunderbird*, p. 456

Frank, A., Blackman, E. G., 2004, The Astrophysical Journal, 614, 737

Garcia-Segura, G., 1997, Astrophysical Journal Letters, 489, L189

García-Segura, G., Langer, N., Różyczka, M., Franco, J., 1999, The Astrophysical Journal, 517, 767

García-Segura, G., López, J. A., 2000, The Astrophysical Journal, 544, 336

García-Segura, G., López, J. A., Franco, J., 2005, The Astrophysical Journal, 618, 919

García-Segura, G., López, J. A., Steffen, W., Meaburn, J., Manchado, A., 2006, Astrophysical Journal Letters, 646, L61

Gauger, A., Balega, Y. Y., Irrgang, P., Osterbart, R., Weigelt, G., 1999, Astronomy and Astrophysics, 346, 505

Goldreich, P., Keeley, D. A., Kwan, J. Y., 1973, The Astrophysical Journal, 179, 111

Goldreich, P., Scoville, N., 1976, The Astrophysical Journal, 205, 144

Gomez, Y., Moran, J., Rodriguez, L., 1990, Revista Mexicana de Astronomía y Astrofísica, 20, 55

Gómez, Y., Rodríguez, L. F., 2000, in J. H. Kastner, N. Soker, and S. Rappaport (eds.), *ASP Conf. Ser. 199: Asymmetrical Planetary Nebulae II: From Origins to Microstructures*, p. 75

Gómez, Y., Tafoya, D., Anglada, G., Franco-Hernandez, R., Torrelles, J. M., Miranda, L. F., 2006, in *Revista Mexicana de Astronomia y Astrofisica Conf. Ser. 26*, p. 22

Guerrero, M. A., Chu, Y.-H., Gruendl, R. A., Williams, R. M., Kaler, J. B., 2001, Astrophysical Journal Letters, 553, L55

Habing, H., 1996, The Astronomy and Astrophysics Review, 7, 97

Harvey, P., Bechis, K., Wilson, W., Ball, J., 1974, Astrophysical Journal Supplement, 27, 331

Hofmann, K.-H., Balega, Y., Blöcker, T., Weigelt, G., 2001, Astronomy and Astrophysics, 379, 529

Högbom, J. A., 1974, Astronomy and Astrophysics Supplement, 15, 417

Hrivnak, B. J., Kwok, S., Su, K. Y. L., 2001, Astronomical Journal, 121, 2775

Hu, J. Y., Slijkhuis, S., Nguyen-Q-Rieu, de Jong, T., 1993, Astronomy and Astrophysics, 273, 185

Iben, I. J., Livio, M., 1993, Publications of the Astronomical Society of the Pacific, 105, 1373

Icke, V., Balick, B., Frank, A., 1992, Astronomy and Astrophysics, 253, 224

Imai, H., Morris, M., Sahai, R., Hachisuka, K., Azzollini F., J. R., 2004, Astronomy and Astrophysics, 420, 265

Imai, H., Obara, K., Diamond, P. J., Omodaka, T., Sasao, T., 2002, Nature, 417, 829

Jordan, S., Werner, K., O'Toole, S. J., 2005, Astronomy and Astrophysics, 432, 273

Kastner, J., Soker, N., Vrtilek, S., Dgani, R., 2000, The Astrophysical Journal, 545, 57

Kastner, J., Vrtilek, S.D.and Soker, N., 2001, The Astrophysical Journal, 550, 189

Kemball, A., 1992, *Ph.D. thesis*, Rhodes University

Kemball, A., 2002, in V. Migenes and M. J. Reid (eds.), *IAU Symp. 206: Cosmic masers: From protostars to black holes*, p. 359

Kemball, A., Diamond, P., Cotton, W., 1995, Astronomy and Astrophysics Supplement Series, 110, 383

Kemball, A. J., 1999, in G. B. Taylor, C. L. Carilli, and R. A. Perley (eds.), *ASP Conf. Ser. 180: Synthesis Imaging in Radio Astronomy II*, p. 499

Kemball, A. J., Diamond, P. J., 1997, Astrophysical Journal Letters, 481, L111

Kerr, F. J., Bowers, P. F., 1974, Astronomy and Astrophysics, 36, 225

Knapp, G. R., 1986, The Astrophysical Journal, 311, 731

Kogan, L., 1995, Technical report, VLBA Scientific Memo No.9, NRAO

Kogan, L., 1996, Technical report, AIPS Memo 92, NRAO

Kwok, S., 1993, Annual Review of Astronomy and Astrophysics, 31, 63

Kwok, S., 1999, in *ASP Conf. Ser. 199: Asymmetrical Planetary Nebulae II: From Origins to MicroStructures*, Vol. 199, p. 3

Kwok, S., Purton, C., Fitzgerald, P., 1978, The Astrophysical Journal, 219, 125

Kwok, S., SU, K., Stoesz, J., 2000, in R. Szczerba and S. Gorny (eds.), *Post-AGB Objects as a phase of Stellar Evolution*, Vol. 265, Astrophyscis and Space Science Library, Kluwer Academic Publishers

Kwok, S., Su, K. Y. L., Hrivnak, B. J., 1998, Astrophysical Journal Letters, 501, L117

Leppanen, K. J., Zensus, J. A., Diamond, P. J., 1995, Astronomical Journal, 110, 2479

Lewis, B. M., 1989, The Astrophysical Journal, 338, 234

Likkel, L., Morris, M., 1988, The Astrophysical Journal, 329, 914

Livio, M., Soker, N., 1988, The Astrophysical Journal, 329, 764

Lopez, J. A., Vazquez, R., Rodriguez, L. F., 1995, Astrophysical Journal Letters, 455, L63

Manchado, A., Villaver, E., Stanghellini, L., Guerrero, M. A., 2000, in J. H. Kastner, N. Soker, and S. Rappaport (eds.), *ASP Conf. Ser. 199: Asymmetrical Planetary Nebulae II: From Origins to Microstructures*, Vol. 199, p. 17

Mastrodemos, N., Morris, M., 1998, The Astrophysical Journal, 497, 303

Matt, S., Frank, A., Blackman, E. G., 2004, in M. Meixner, J. H. Kastner, B. Balick, and N. Soker (eds.), *ASP Conf. Ser. 313: Asymmetrical Planetary Nebulae III: Winds, Structure and the Thunderbird*, p. 449

Mauersberger, R., Henkel, C., Wilson, T., Olano, C., 1988, Astronomy and Astrophysics, 206, 34

Mauron, N., Huggins, P. J., 2000, Astronomy and Astrophysics, 359, 707

Mauron, N., Huggins, P. J., 2006, Astronomy and Astrophysics, 452, 257

Mellema, G., 1997, Astronomy and Astrophysics, 321, L29

Mellema, G., Frank, A., 1997, Monthly Notices of the Royal Astronomical Society, 292, 795

Migenes, V., Ludke, E., Cohen, R. J., Shepherd, M., Bowers, P. F., 1995, Astrophysics and Space Science, 224, 515

Miranda, L. F., Gómez, Y., Anglada, G., Torrelles, J. M., 2001, Nature, 414, 284

Moran, J., Dhawan, V., 1995, in J.A.Zensus, P. Diamond, and P. Napier (eds.), *ASP Conf. Ser. 82: Very Long Baseline Interferometery and the VLBA*, p. 161

Morris, M., 1987, Publications of the Astronomical Society of the Pacific, 99, 1115

Morris, M., Bowers, P. F., Turner, B. E., 1982, The Astrophysical Journal, 259, 625

Nedoluha, G., Bowers, P., 1992, The Astrophysical Journal, 392, 249

Nedoluha, G., Watson, W., 1988, The Astrophysical Journal, 335, 19

Nedoluha, G. E., Watson, W. D., 1990, The Astrophysical Journal, 361, 653

Neri, R., Kahane, C., Lucas, R., Bujarrabal, V., Loup, C., 1998, Astronomy and Astrophysics Supplement, 130, 1

Nordhaus, J., Blackman, E. G., 2006, Monthly Notices of the Royal Astronomical Society, 370, 2004

Norris, R. P., Diamond, P. J., Booth, R. S., 1982, Nature, 299, 131

Nyman, L., Hall, P., Bertre, T., 1993, Astronomy and Astrophysics, 280, 551

Nyman, L., Hall, P., Olofsson, H., 1998, Astronomy and Astrophysics, 127, 185

Olofsson, H., 1999, in T. Le Bertre, A. Lebre, and C. Waelkens (eds.), *IAU Symp. 191: Asymptotic Giant Branch Stars*, p. 3

Olofsson, H., 2001, in A. Wooten (ed.), *ASP Conf. Ser. 235: Science with the Atacama Large Millimeter Array*, Vol. 235, p. 355

Pascoli, G., 1997, The Astrophysical Journal, 489, 946

Pearson, T., Readhead, A., 1984, Annual Review of Astronomy and Astrophysics, 22, 97

Pottasch, S. R., Bignelli, C., Zijlstra, A., 1987, Astronomy and Astrophysics, 177, L49

Readhead, A., Wilkinson, P., 1978, The Astrophysical Journal, 223, 25

Reid, M., 1995, in J.A.Zensus, P. Diamond, and P. Napier (eds.), *ASP Conf. Ser. 82: Very Long Baseline Interferometry and the VLBA*, Vol. 82, p. 209, ASP Conference Series

Reid, M. J., 1990, in R. Beck, R. Wielebinski, and P. P. Kronberg (eds.), *IAU Symp. 140: Galactic and Intergalactic Magnetic Fields*, p. 21

Reid, M. J., 2002, in V. Migenes and M. J. Reid (eds.), *IAU Symp. 206: Cosmic masers: From protostars to black holes*, p. 506

Reid, M. J., Haschick, A. D., Burke, B. F., Moran, J. M., Johnston, K. J., Swenson, Jr., G. W., 1980, The Astrophysical Journal, 239, 89

Reid, M. J., Moran, J. M., Leach, R. W., Ball, J. A., Johnston, K. J., Spencer, J. H., Swenson, G. W., 1979, Astrophysical Journal Letters, 227, L89

Reid, M. J., Muhleman, D. O., Moran, J. M., Johnston, K. J., Schwartz, P. R., 1977, The Astrophysical Journal, 214, 60

Reyes-Ruiz, M., López, J. A., 1999, The Astrophysical Journal, 524, 952

Roberts, D. H., Brown, L. F., Wardle, J. F. C., 1991, in T. J. Cornwell and R. A. Perley (eds.), *ASP Conf. Ser. 19: IAU Colloq. 131: Radio Interferometry. Theory, Techniques, and Applications*, p. 281

Roberts, D. H., Gabuzda, D. C., Wardle, J. F. C., 1987, The Astrophysical Journal, 323, 536

Roberts, D. H., Wardle, J. F. C., 1986, in V. K. Kapahi and G. Swarup (eds.), *IAU Symp. 119: Quasars*, p. 141

Rozyczka, M., Franco, J., 1996, Astrophysical Journal Letters, 469, L127

Russell, C., 1999, Australian Journal of Physics, 52, 733

Ryle, M., Vonberg, D., 1946, Nature, 158, 339

Sahai, R., 2002, in W. J. Henney, W. Steffen, L. Binette, and A. Raga (eds.), *Revista Mexicana de Astronomia y Astrofisica Conf. Ser. 13: Emission Lines from Jet Flows*, p. 133

Sahai, R., 2004, in M. Meixner, J. H. Kastner, B. Balick, and N. Soker (eds.), *ASP Conf. Ser. 313: Asymmetrical Planetary Nebulae III: Winds, Structure and the Thunderbird*, p. 141

Sahai, R., Le Mignant, D., Sánchez Contreras, C., Campbell, R. D., Chaffee, F. H., 2005, Astrophysical Journal Letters, 622, L53

Sahai, R., Te Lintel Hekkert, P., Morris, M., Zijlstra, A., Likkel, L., 1999, The Astrophysical Journal, 514, L115

Sahai, R., Trauger, J. T., 1998, Astronomical Journal, 116, 1357

Sahai, S., 1999, in *ASP Conf. Ser. 199: Asymmetrical Planetary Nebulae II: From Origins to MicroStructures*, p. 209

Sandquist, E. L., Taam, R. E., Chen, X., Bodenheimer, P., Burkert, A., 1998, The Astrophysical Journal, 500, 909

Sault, R. J., Killeen, N. E. B., Zmuidzinas, J., Loushin, R., 1990, The Astrophysical Journals, 74, 437

Schwab, F., Cotton, W., 1983, Astronomical Journal, 88, 688

Seaquist, E. R., Plume, R., Davis, L. E., 1991, The Astrophysical Journal, 367, 200

Sevenster, M., 2002, Astronomical Journal, 123, 2788

Sevenster, M. N., Chapman, J. M., Habing, H. J., Killeen, N. E. B., Lindqvist, M., 1997, Astronomy and Astrophysics Supplement Series, 122, 79

Shepherd, M. C., Cohen, R. J., Gaylard, M. J., West, M. E., 1990, Nature, 344, 522

Shurcliff, W., Ballard, S., 1964, *Polarized Light*, D.van Nostrand Company, Princeton, New Jersey

Soker, N., 1998, Monthly Notices of the Royal Astronomical Society, 299, 1242

Soker, N., 2000, The Astrophysical Journal, 540, 436

Soker, N., 2004, in M. Meixner, J. H. Kastner, B. Balick, and N. Soker (eds.), *ASP Conf. Ser. 313: Asymmetrical Planetary Nebulae III: Winds, Structure and the Thunderbird*, p. 562

Soker, N., 2006, Publications of the Astronomical Society of the Pacific, 118, 260

Soker, N., Kastner, J. H., 2003, The Astrophysical Journal, 592, 498

Soker, N., Livio, M., 1989, The Astrophysical Journal, 339, 268

Soker, N., Livio, M., 1994, The Astrophysical Journal, 421, 219

Soker, N., Rappaport, S., 2000, The Astrophysical Journal, 538, 241

Soker, N., Zoabi, E., 2002, Monthly Notices of the Royal Astronomical Society, 329, 204

Szymczak, M., Gérard, E., 2004, Astronomy and Astrophysics, 423, 209

Szymczak, M., Gérard, E., 2005, Astronomy and Astrophysics, 433, L29

Thompson, A., 1989, in *ASP Conf. Ser. 6: Synthesis Imaging in Radio Astronomy*, p. 11

Thompson, A., Moran, J., Swenson, G., 2001, *Interferometry and Synthesis in Radio Astronomy*, John Wiley Sons, New York, second edition

Troland, T. H., Heiles, C., 1982, The Astrophysical Journal, 252, 179

Turner, B. E., 1970, Publications of the Astronomical Society of the Pacific, 82, 996

Ueta, T., Meixner, M., Bobrowsky, M., 2000, The Astrophysical Journal, 528, 861

Ulvestad, J., Woebel, J., 2006, Technical report, VLBA Observational Status Summary, NRAO

van der Veen, W., Habing, H., 1988, Astronomy and Astrophysics, 194, 125

van der Walt, D., Retief, S., Gaylard, M., MacLeod, G., 1996, Monthly Notices of the Royal Astronomical Society, 282, 1085

Vlemmings, W. H. T., Diamond, P. J., Imai, H., 2006, Nature, 440, 58

Vlemmings, W. H. T., Diamond, P. J., van Langevelde, H. J., 2002, Astronomy and Astrophysics, 394, 589

Vlemmings, W. H. T., van Langevelde, H. J., Diamond, P. J., 2005, Astronomy and Astrophysics, 434, 1029

Vlemmings, W. H. T., van Langevelde, H. J., Diamond, P. J., Habing, H. J., Schilizzi, R. T., 2003, Astronomy and Astrophysics, 407, 213

Walker, R., 1977, *Ph.D. thesis*, Massachusetts In

Walker, R., 1989, in R. A. Perley, F. R. Schwab, and A. H. Bridle (eds.), *ASP Conf. Ser. 6: Synthesis Imaging in Radio Astronomy*, p. 355

Walker, R. C., 1999, in G. B. Taylor, C. L. Carilli, and R. A. Perley (eds.), *ASP Conf. Ser. 180: Synthesis Imaging in Radio Astronomy II*, p. 433

Walsh, A., Hyland, A., Robinson, G., Burton, M., 1997, Monthly Notices of the Royal Astronomical Society, 291, 261

Wardle, J. F. C., Roberts, D. H., 1988, in M. J. Reid and J. M. Moran (eds.), *IAU Symp. 129: The Impact of VLBI on Astrophysics and Geophysics*, p. 143

Wardle, J. F. C., Roberts, D. H., Potash, R. I., Rogers, A. E. E., 1986, The Astrophysical Journal, 304, L1

Weigelt, G., Balega, Y. Y., Blöcker, T., Hofmann, K.-H., Men'shchikov, A. B., Winters, J. M., 2002, Astronomy and Astrophysics, 392, 131

Werner, M., Beckwith, S., Gately, I., Sellgreen, K., Berriman, G., Whiting, D., 1980, The Astrophysical Journal, 239, 540

Wiebe, D. S., Watson, W. D., 1998, Astrophysical Journal Letters, 503, L71

Yusef-Zadeh, F., Wardle, M., Roberts, D., 1996, The Astrophysical Journal, 458, 21

Zell, P., Fix, J. D., 1991, The Astrophysical Journal, 369, 506

Zijlstra, A. A., Chapman, J. M., te Lintel Hekkert, P., Likkel, L., Comeron, F., Norris, R. P., Molster, F. J., Cohen, R. J., 2001, Monthly Notices of the Royal Astronomical Society, 322, 280

Zijlstra, A. A., Te Lintel Hekkert, P., Pottasch, S. R., Caswell, J. L., Ratag, M., Habing, H. J., 1989, Astronomy and Astrophysics, 217, 157